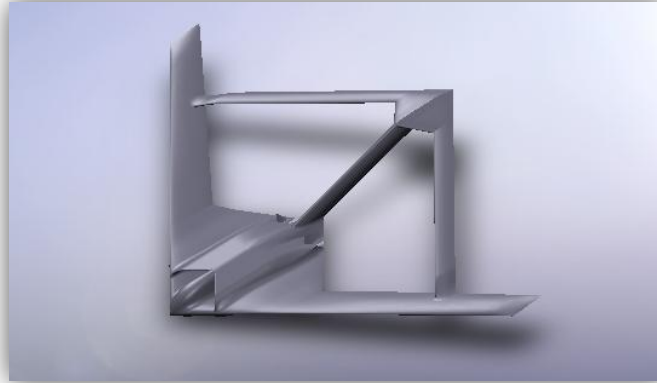




INSTITUTO SUPERIOR TÉCNICO  
Universidade Técnica de Lisboa



## **Development of Control Strategies for the Joined-Wing Aircraft**

**Bernardo Medina dos Santos Cunha**

Dissertação para obtenção do Grau de Mestre em  
**Engenharia Aeroespacial**

### **Júri:**

Presidente:	Prof. João Miranda Lemos
Orientador:	Prof. Fernando Lau
Co-Orientador:	Prof. Afzal Suleman
Vogal:	Prof. Pedro Gamboa
Vogal:	Prof. Agostinho Fonseca

**June 2011**



# Acknowledgments

To my parents, Mário and Maria, for all the unconditional love and care which they raised me, I will always be eternally grateful. They always were and will be my great inspirations and what I am today I owe everything to them. A truly thanks from the deep inside my heart.

My sincere thanks to my family for all the support and encouragement, specially my sister, Raquel, who always put me first than everything and everyone.

I am thankful to my mentors, professor Lau and professor Suleman, for the opportunity to work on this project of so much interest and which allowed me to expand my knowledge. To them I am very grateful for all the help and support, capable of pulling me up in the hard times.

I would like to express also my gratitude to all the professors who accompanied through all my studies; to them I owe the best education.

Last but not least, a special thanks to all my friends for their presence in the different moments of my life and for their real and so needed friendship.

# Abstract

In this thesis, different control strategies for an Unmanned Aerial Vehicle with a joined-wing configuration - Joined-Wing SensorCraft - are developed and analyzed. Both longitudinal and lateral motions are considered, but more attention will be given to the lateral motion due to the aircraft particularity of not having a rudder.

The control strategies explored several combinations of the control surfaces to investigate mixed-control and speed-brake control techniques.

The aircraft geometry was modeled into lifting surfaces and analyzed through the Lattice Vortex Method using the Athena Vortex Lattice (*AVL*) program, allowing the calculation of the stability coefficients.

In order to generate more accurate results, the profile drag was calculated using the *XFOIL* program, and later merged with the *AVL* results.

The static stability was confirmed through the evaluation of the stability derivatives, while the dynamic stability resulted in an aircraft longitudinally unstable and with a lateral of *level 2*.

From the analysis of the stability derivatives and the aircraft stability results were developed several configurations to investigate the control strategies. The efficiency of each configuration was calculated through the development of conventional and modern Automatic Flight Control Systems, used as methods of comparison method.

Finally, analyzing and comparing the results, a solution was achieved for the two most efficient configurations controlling the lateral motion, which belong to the speed-brake control technique. Meanwhile, the flight tests results from an already built SensorCraft model were qualitatively compared with the theoretical results.

**Keywords:** Joined-Wing, SensorCraft, Unmanned Aerial Vehicle, Mixed-control, Speed-brake control, Automatic Flight Control System

# Resumo

Na presente tese foram desenvolvidas e analisadas diferentes estratégias de controlo para um Veículo Aéreo Não Tripulado com uma configuração asa-junta – Joined-Wing SensorCraft. Tanto o movimento longitudinal como o lateral foram considerados, mas irá ser dada maior relevância ao movimento lateral devido à particularidade da aeronave não possuir um leme de direcção.

As estratégias de controlo exploraram as diversas combinações entre superfícies de controlo de modo a investigar as técnicas de controlo misto e de travagem.

A geometria da aeronave foi modelada em painéis sustentadores e analisada através do método da Malha de Vórtices usando programa Athena Vortex Lattice (*AVL*), permitindo o cálculo dos coeficientes de estabilidade.

De modo a gerar resultados mais precisos, o arrasto de forma foi calculado usando o programa *XFOIL*, e mais tarde os resultados foram combinados com os do *AVL*.

A estabilidade estática foi confirmada através da avaliação das derivadas de estabilidade, enquanto a estabilidade dinâmica resultou em uma aeronave longitudinalmente instável e com um lateral de *nível 2*.

Da análise das derivadas de estabilidade e dos resultados da estabilidade da aeronave foram desenvolvidas várias configurações para investigar as estratégias de controlo. A eficiência de cada configuração foi calculada através do desenvolvimento de Sistemas de Controlo de Voo Automático convencionais e modernos, usados como métodos de comparação.

Finalmente, analisando e comparando os resultados, chegou-se a uma solução para as duas configurações mais eficientes a controlar o movimento lateral, referentes à técnica controlo de travagem.

Entretanto, os resultados dos testes de voo de um modelo do SensorCraft previamente construído foram comparados qualitativamente com os resultados teóricos.

**Palavras-chave:** Asa-Junta, SensorCraft, Veículo Aéreo Não Tripulado, Controlo misto, Controlo de travagem, Sistema de Controlo de Voo Automático

# Contents

List of Figures	vii
List of Tables	ix
Nomenclature	x
1 Introduction	1
1.1 Development of the Joined-Wing concept.....	2
1.2 Thesis motivation .....	2
1.3 Thesis objectives.....	3
1.4 Properties definitions .....	3
1.6 Thesis layout.....	4
2 Joined-Wing SensorCraft	5
2.1 Configuration and aircraft properties .....	5
2.2 Control strategies in rudderless aircraft configurations .....	7
2.3 Dynamics of flight.....	9
2.4 State space representation of the equations of motion .....	15
3 Stability Coefficients of SensorCraft	17
3.1 Determination of stability coefficients using <i>AVL</i> .....	17
3.2 Stability coefficient estimation.....	20
3.3 Drag contributions.....	21
3.4 Determination of the Parasitic Drag using XFOIL .....	22
3.5 Determination of the Induced Drag using AVL.....	26
3.6 <i>XFOIL</i> and <i>AVL</i> result implications.....	30
3.7 Yaw coefficient results.....	31
4 Aircraft Stability Analysis	33
4.1 Static stability analysis.....	33
4.2 Dynamic stability analysis.....	35
4.3 Flying qualities evaluation .....	39
4.4 Configuration analysis of different control surface deflections.....	40
5 Control System Methods	49
5.1 Equivalent control surface transformation .....	49

5.2 Aircraft open loop system .....	59
5.3 Control system design .....	61
6 Results Analysis .....	77
6.1 Configurations results analysis .....	77
6.2 Qualitative validation with the SensorCraft heuristic model .....	79
7 Conclusions and Future Work .....	83

# List of Figures

FIGURE 1.1 – JOINED-WING SENSORCRAFT SCHEMATIC, WITH AXIS SYSTEM FOR CG AND AVL DATA DEFINITION .....	4
FIGURE 2.1 - SCHEMATIC VIEWS OF THE SENSORCRAFT .....	5
FIGURE 2.2 - CONTROL SURFACES DISTRIBUTION .....	6
FIGURE 2.4 - FRONT AND TOP VIEWS OF MIXED-CONTROL FORCES EXEMPLIFICATION [9] .....	7
FIGURE 2.3 - LONGITUDINAL SECTION OF THE SENSORCRAFT SHOWING THE ENGINE POSITION AND THE AIR INLET (YELLOW) OUTLET (RED) CONFIGURATION [9] .....	7
FIGURE 2.5 - AIRCRAFT B-2 SPIRIT USING SPEED-BRAKE CONTROL [10] .....	8
FIGURE 2.6 – EXEMPLIFICATION OF DIFFERENTIAL THRUST CONTROL METHOD [11] .....	8
FIGURE 2.7 - AIRCRAFT EARTH AXIS SYSTEM [12] .....	9
FIGURE 2.8 - AIRCRAFT BODY-FIXED AXIS SYSTEM [12] .....	9
FIGURE 2.9 - STATE SPACE BLOCK DIAGRAM [13] .....	15
FIGURE 3.1 - AVL SECTIONS LOCALIZATION .....	18
FIGURE 3.2 - AVL SENSORCRAFT MODEL .....	18
FIGURE 3.3 - XFOIL WINDOW RESULTS ENVIRONMENT .....	23
FIGURE 3.4 - $CDp$ vs $\delta f$ CURVE.....	24
FIGURE 3.5 - $CDp$ vs $\delta f$ CURVE SLOPES GIVEN BY LINEAR EQUATIONS .....	24
FIGURE 3.6 - $CDp$ vs $\delta ai$ CURVE .....	24
FIGURE 3.7 - $CDp$ vs $\delta ai$ CURVE SLOPES GIVEN BY LINEAR EQUATIONS .....	24
FIGURE 3.8 - $CDp$ vs $\delta ao$ CURVE.....	25
FIGURE 3.9 - $CDp$ vs $\delta ao$ CURVE SLOPES GIVEN BY LINEAR EQUATIONS .....	25
FIGURE 3.10 - $CDp$ vs $\delta ei$ CURVE.....	25
FIGURE 3.11 - $CDp$ vs $\delta ei$ CURVE SLOPES GIVEN BY LINEAR EQUATIONS .....	25
FIGURE 3.12 - $CDp$ vs $\delta eo$ CURVE.....	26
FIGURE 3.13 - $CDp$ vs $\delta eo$ CURVE SLOPES GIVEN BY LINEAR EQUATIONS .....	26
FIGURE 3.14 - $CDi$ vs $\delta f$ CURVE.....	27
FIGURE 3.15 - $CDi$ vs $\delta f$ CURVE SLOPES GIVEN BY LINEAR EQUATIONS .....	27
FIGURE 3.16 - $CDi$ vs $\delta ai$ CURVE .....	27
FIGURE 3.17 - $CDi$ vs $\delta ai$ CURVE SLOPES GIVEN BY LINEAR EQUATIONS.....	27
FIGURE 3.18 - $CDi$ vs $\delta ao$ CURVE .....	28
FIGURE 3.19 - $CDi$ vs $\delta ao$ CURVE SLOPES GIVEN BY LINEAR EQUATIONS .....	28
FIGURE 3.20 - $CDi$ vs $\delta ei$ CURVE .....	28
FIGURE 3.21 - $CDi$ vs $\delta ei$ CURVE SLOPES GIVEN BY LINEAR EQUATIONS .....	28
FIGURE 3.22 - $CDi$ vs $\delta eo$ CURVE.....	29
FIGURE 3.23 - $CDi$ vs $\delta eo$ CURVE SLOPES GIVEN BY LINEAR EQUATIONS .....	29
FIGURE 3.24 - RESOLVED FORCE COMPONENTS FOR A $CS$ DEFLECTION .....	30
FIGURE 4.1 - (A) STATICALLY STABLE (B) STATICALLY UNSTABLE (C) NEUTRALLY STABLE [18] .....	33
FIGURE 4.2 - LONGITUDINAL EIGENVALUES IN ARGAND PLAN.....	38
FIGURE 4.3 - LATERAL EIGENVALUES IN ARGAND PLAN.....	38
FIGURE 4.4 - FRONT AND TOP VIEWS OF FORCES PRODUCED BY ELEVATORS DEFLECTED IN (A) OPPOSITE AND (B) SAME DIRECTIONS .....	42
FIGURE 4.5 - FRONT AND TOP VIEWS OF FORCES AND MOMENTS PRODUCED BY THE OUTBOARDS ELEVATOR AND AILERON ...	43
FIGURE 4.6 - MIXED-CONTROL CONFIGURATION 1 AND 2 (LEFT AND RIGHT RESPECTIVELY) .....	45
FIGURE 4.7 - MIXED-CONTROL CONFIGURATION 3.....	45
FIGURE 4.8 - MIXED-CONTROL CONFIGURATION 4 AND 5 (LEFT AND RIGHT RESPECTIVELY) .....	45
FIGURE 4.9 - MIXED-CONTROL CONFIGURATION 6 AND 7 (LEFT AND RIGHT RESPECTIVELY) .....	45
FIGURE 4.10 - ANALOGY BETWEEN CONVENTIONAL SPLIT FLAPS AND SENSORCRAFT SPLIT FLAPS.....	46

FIGURE 4.11 - $FX$ AND $FY$ COMPONENTS FOR (A) FRONT WING DOWN DEFLECTION AND AFT WING UP DEFLECTION AND (B) FRONT WING UP DEFLECTION AND AFT WING DOWN DEFLECTION.....	47
FIGURE 4.12 - SPEED-BRAKE CONTROL CONFIGURATION 1 AND 2 (LEFT AND RIGHT RESPECTIVELY).....	47
FIGURE 4.13 - SPEED-BRAKE CONTROL CONFIGURATION 3 .....	47
FIGURE 4.14 - SPEED-BRAKE CONTROL CONFIGURATION 4 AND 5 (LEFT AND RIGHT RESPECTIVELY).....	48
FIGURE 4.15 - SPEED-BRAKE CONTROL CONFIGURATION 6 AND 7 (LEFT AND RIGHT RESPECTIVELY).....	48
FIGURE 5.1 - COMPARISON OF THE STABILITY COEFFICIENT $Cn\delta r$ FOR EACH CONFIGURATION.....	59
FIGURE 5.2 - OPEN LOOP REPRESENTATIVE SYSTEMS FOR (A) LONGITUDINAL AND (B) LATERAL MOTIONS.....	60
FIGURE 5.3 - RECTANGULAR SIGNAL INPUT OF CONTROL SURFACES .....	60
FIGURE 5.4 - LONGITUDINAL RESPONSE TO A 3 DEGREE RECTANGULAR SIGNAL IN ELEVATORS.....	60
FIGURE 5.5 - LATERAL RESPONSE TO A 3 DEGREE RECTANGULAR SIGNAL IN AILERONS.....	61
FIGURE 5.6 - LATERAL RESPONSE TO A 3 DEGREE RECTANGULAR SIGNAL IN RUDDER.....	61
FIGURE 5.7 - TYPICAL FEEDBACK CONTROL SYSTEM .....	62
FIGURE 5.8 - ROOT LOCUS OF LONGITUDINAL SYSTEM AND RESPECTIVE LEGEND.....	64
FIGURE 5.9 - ROOT LOCUS OF LATERAL SYSTEM .....	65
FIGURE 5.10 - CLOSE LOOP SYSTEMS FOR (A) LONGITUDINAL AND (B) LATERAL MOTIONS .....	66
FIGURE 5.11 - LONGITUDINAL RESPONSE OF FEEDBACK SYSTEM TO A 3 DEGREE RECTANGULAR SIGNAL IN ELEVATORS .....	66
FIGURE 5.12 - LATERAL RESPONSE OF THE FEEDBACK SYSTEM TO A 3 DEGREE RECTANGULAR SIGNAL IN AILERONS .....	66
FIGURE 5.13 - LATERAL RESPONSE OF THE FEEDBACK SYSTEM TO A 3 DEGREE RECTANGULAR SIGNAL IN RUDDER .....	66
FIGURE 5.14 - FLIGHT PATH CONTROL SYSTEM OF $\psi$ AND $\phi$ USING THE LQR FEEDBACK GAIN MATRIX .....	71
FIGURE 5.15 - RESPONSE OF LQR FEEDBACK SYSTEM – SATURATION CASE 1.....	72
FIGURE 5.16 - RESPONSE OF LQR FEEDBACK SYSTEM – SATURATION CASE 2.....	72
FIGURE 5.17 - $\psi$ RESPONSE FOR MIXED-CONTROL CONFIGURATIONS (LEFT) AND RESPECTIVE ZOOM (RIGHT).....	73
FIGURE 5.18 - $\psi$ RESPONSE FOR SPEED-BRAKE CONTROL CONFIGURATIONS (LEFT) AND RESPECTIVE ZOOM (RIGHT) .....	73
FIGURE 5.19 - $\psi$ RESPONSE COMPARISON BETWEEN MIXED-CONTROL AND SPEED-BRAKE CONTROL .....	73
FIGURE 5.20 - $\psi$ RESPONSE FOR MIXED-CONTROL CONFIGURATIONS.....	74
FIGURE 5.21 - $\psi$ RESPONSE FOR SPEED-BRAKE CONTROL CONFIGURATIONS .....	74
FIGURE 5.22 - $\psi$ RESPONSE COMPARISON BETWEEN MIXED-CONTROL AND SPEED-BRAKE CONTROL .....	74
FIGURE 5.23 - EQUIVALENT RUDDER USE DURING THE REQUESTED HEADING ANGLE CHANGE .....	75
FIGURE 6.1 - COMPARISON OF THE CLOSE LOOP GAINS FOR EACH CONFIGURATION .....	78
FIGURE 6.2 - HEURISTIC MODEL AIRFRAME CONTOUR [20] .....	80
FIGURE 6.3 - JOINED WING SENSORCRAFT 3 [20].....	80
FIGURE A.1 - SWEEP ANGLE DEFINITION .....	89
FIGURE A.2 - DIHEDRAL ANGLE DEFINITION [21] .....	89
FIGURE A.3 - TWIST ANGLE DEFINITION [22] .....	90
FIGURE E.1 - DRAG-POLAR POINTS SELECTION FROM <i>JavaFoil</i> PROGRAM .....	93
FIGURE F.1 - <i>AVL</i> STABILITY COEFFICIENTS RESULTS .....	94
FIGURE G.1 - LONGITUDINAL NATURAL FREQUENCY, DAMPING RATIO AND EIGENVALUES.....	95
FIGURE G.2 - LATERAL NATURAL FREQUENCY, DAMPING RATIO AND EIGENVALUES .....	95
FIGURE I.1 - STABLE SHORT PERIOD MODE [19] .....	96
FIGURE I.2 - STABLE PHUGOID MODE [19] .....	96
FIGURE I.3 - SPIRAL MODE [19] .....	97
FIGURE I.4 - DUTCH ROLL MODE EXPLANATION [19] .....	98
FIGURE I.5 - ROLL MODE [19] .....	99

# List of Tables

TABLE 2.1 - SENSORCRAFT FLIGHT CONDITION PARAMETERS.....	6
TABLE 2.2 – LEGEND OF FIGURE 2.2 .....	6
TABLE 3.1 - LONGITUDINAL STABILITY DERIVATIVES .....	19
TABLE 3.2 - LATERAL STABILITY DERIVATIVES.....	20
TABLE 3.3 – AVL AND XFOIL DRAG COEFFICIENTS.....	22
TABLE 3.4 - INPUT AIRFOIL PROPERTIES FOR <i>XFOIL</i> .....	23
TABLE 3.5 - DRAG COEFFICIENTS OF THE CONTROL SURFACES.....	31
TABLE 3.6 - YAW MOMENT COEFFICIENTS OF THE CONTROL SURFACES.....	32
TABLE 4.1 - STATIC STABILITY OF THE SENSORCRAFT .....	35
TABLE 4.2 - LONGITUDINAL EIGENVALUES .....	38
TABLE 4.3 - LATERAL EIGENVALUES.....	38
TABLE 4.4 - SHORT PERIOD AND PHUGOID FLIGHT QUALITY RESULTS.....	39
TABLE 4.5 - LATERAL MODES FLIGHT QUALITY RESULTS .....	40
TABLE 4.6 - STABILITY COEFFICIENTS OF RIGHT OUTBOARD AILERON AND ELEVATOR.....	43
TABLE 4.7 - DRAG-LESS YAWING COEFFICIENT $C_{n\delta s}$ OF CONTROL SURFACES.....	44
TABLE 5.1 - MIXED-CONTROL EQUIVALENT RUDDER STABILITY COEFFICIENTS.....	58
TABLE 5.2 - SPEED-BRAKE CONTROL EQUIVALENT RUDDER STABILITY COEFFICIENTS .....	58
TABLE 5.3 - LONGITUDINAL FEEDBACK SYSTEM PROPERTIES .....	64
TABLE 5.4 - LATERAL FEEDBACK SYSTEM PROPERTIES .....	65
TABLE 5.5 - GAINS AND EIGENVALUES OF THE LONGITUDINAL CONFIGURATIONS .....	68
TABLE 5.6 - GAINS AND EIGENVALUES OF THE LATERAL CONFIGURATIONS.....	68
TABLE 5.7 - LATERAL LQR FEEDBACK SYSTEM PROPERTIES.....	70
TABLE 6.1 - EQUIVALENT RUDDER CLASSIFICATIONS .....	81
TABLE B.1 - SENSORCRAFT CHARACTERISTICS AND GEOMETRY PARAMETERS .....	90
TABLE B.2 - CG POSITION .....	91
TABLE H.1 - ESTIMATED VALUES .....	96
TABLE J.1 - AIRCRAFT CLASSIFICATION .....	100
TABLE J.2 - AIRCRAFT FLIGHT PHASES .....	100
TABLE J.3 - AIRCRAFT QUALITY FLIGHT LEVELS .....	100
TABLE J.4 - SHORT PERIOD MODE DAMPING RATIO SPECIFICATION .....	101
TABLE J.5 - PHUGOID MODE FLYING QUALITIES.....	101
TABLE J.6 - SPIRAL MODE LEVELS SPECIFICATION.....	102
TABLE J.7 - DUTCH ROLL MODE LEVELS SPECIFICATION .....	102
TABLE J.8 - ROLL MODE TIME CONSTANT SPECIFICATION .....	102

# Nomenclature

## Latin Letters

$A$	State coefficient matrix
$a_y$	Side slip acceleration
$a_z$	Acceleration in $Z$ -axis
$b$	Wing Span
$B$	Driving matrix
$C$	Output matrix
$\bar{c}$	Mean aerodynamic chord line
$cg_x$	Distance of the center of gravity from the $X$ -axis
$cg_y$	Distance of the center of gravity from the $Y$ -axis
$cg_{xy}$	Distance of the center of gravity from the $XY$ -plane
$C_D$	Drag coefficient
$C_{D\alpha}$	Drag curve slope
$C_{D_i}$	Induced drag coefficient
$C_{D_p}$	Parasitic drag coefficient
$C_{D_u}$	Change in the drag coefficient due to the $u$ -direction velocity
$C_{D_\delta}$	Change in the drag coefficient due to the deflection of control surfaces
$C_L$	Lift Coefficient
$C_{L\alpha}$	Lift curve slope
$C_{L_u}$	Change in the lift coefficient due to the $u$ -direction velocity
$C_{L_\delta}$	Change in the lift coefficient due to the deflection of control surfaces
$C_l$	Rolling moment coefficient
$C_{l_\beta}$	Change in $C_l$ due to a change in the side slip angle
$C_{l_p}$	Change in $C_l$ due to a change in the rolling rate
$C_{l_r}$	Change in $C_l$ due to a change in the yawing rate
$C_{l_v}$	Change in $C_l$ due to a change in the $v$ -direction velocity
$C_{l_\delta}$	Change in $C_l$ due to the deflection of control surfaces
$C_m$	Pitching moment coefficient
$C_{m_0}$	Pitching moment coefficient of the wing
$C_{m\alpha}$	Slope of $C_m$ versus $\alpha$
$C_{m_u}$	Change in $C_m$ caused by the change in the $u$ -direction velocity
$C_{m_\delta}$	Change in $C_m$ due to the deflection of the control surfaces
$C_n$	Yawing moment coefficient

$C_{n\beta}$	Change in $C_n$ due to a change in the side slip angle
$C_{np}$	Change in $C_n$ due to a change in the rolling rate
$C_{nr}$	Change in $C_n$ due to a change in the yawing rate
$C_{nv}$	Change in $C_n$ due to a change in the $v$ -direction velocity
$C_{n\delta}$	Change in $C_n$ due deflection of the control surfaces
$C_X$	$X$ -axis force coefficient
$C_{X\alpha}$	Slope of $C_X$ versus $\alpha$
$C_{Xq}$	Change in $C_X$ due to the change in pitching rate
$C_{Xu}$	Change in $C_X$ caused by the change in the $u$ -direction velocity
$C_{Xw}$	Change in $C_X$ caused by the change in the $w$ -direction velocity
$C_{X\delta}$	Change in $C_X$ due to the deflection of the control surfaces
$C_Y$	$Y$ -axis force coefficient
$C_{Y\beta}$	Change in $C_Y$ due to a change in the side slip angle
$C_{Yp}$	Change in $C_Y$ due to a change in the rolling rate
$C_{Yr}$	Change in $C_Y$ due to a change in the yawing rate
$C_{Yv}$	Change in $C_Y$ due to a change in the $v$ -direction velocity
$C_{Y\delta}$	Change in $C_Y$ due to the deflection of the control surfaces
$C_Z$	$Z$ -axis force coefficient
$C_{Z\alpha}$	Slope of $C_Z$ versus $\alpha$
$C_{Zq}$	Change in $C_Z$ due to the change in pitching rate
$C_{Zu}$	Change in $C_Z$ caused by the change in the $u$ -direction velocity
$C_{Zw}$	Change in $C_Z$ caused by the change in the $w$ -direction velocity
$C_{Z\delta}$	Change in $C_Z$ due deflection of the control surfaces
$D$	Feed forward matrix
$D_i$	Parasitic drag force
$D_p$	Induced drag force
$e$	Oswald efficiency number
$g$	Acceleration due to gravity
$h_0$	Reference altitude
$i$	Complex number
$I$	Identity matrix
$I_x$	Moment of inertia in roll direction
$I_y$	Moment of inertia in pitch direction
$I_z$	Moment of inertia in yaw direction
$J$	Cost function
$l, m, n$	Roll, pitch and yaw moments
$\mathcal{L}$	Lagrangian

$L_{\beta}, L_v$	Dihedral effect
$L_p$	Roll damping
$L_r$	Rolling moment due to the yaw rate
$L_{\delta}$	Rolling moment due to the deflection of the control surfaces
$m$	Mass
$M$	Mach number
$M_{\alpha}$	Change in the pitching moment due to the angle of attack
$M_u$	Change in the pitching moment due to the $u$ -direction velocity
$M_w$	Change in the pitching moment due to the $w$ -direction velocity
$M_q$	Change in the pitching moment due to the pitch rate
$M_{\delta}$	Pitching moment due to the deflection of the control surfaces
$M_{\dot{w}}$	Damping stability derivative
$N_{\beta}, N_v$	Static directional stability or weathercock stability
$N_p$	Yawing moment due to the roll rate
$N_r$	Yaw rate damping
$N_{\delta}$	Yawing moment due to the deflection of the control surfaces
$P$	Period of an oscillatory function
$p, q, r$	Roll, pitch and yaw rates
$Q$	Dynamic pressure
$Re$	Reynolds number
$s$	Variable of control transfer functions
$S$	Wing reference area
$T$	Time constant
$T_s$	Time to double
$u, v, w$	Velocity components
$U$	Forward velocity
$U_0$	Upstream air speed
$U_{0n}$	Normal component of the air speed on wing due to the sweep angle
$\vec{u}$	Control input variables
$V$	Side velocity
$V_T$	Velocity vector
$W$	Vertical velocity
$x_{ac}$	Position of the aerodynamic center
$x_{cg}$	Position of the center of gravity
$X$	Axial force
$X_u$	Stability derivative of $X$ in $u$ -direction velocity
$X_w$	Stability derivative of $X$ in $w$ -direction velocity
$X_q$	Stability derivative of $X$ due to the pitch rate
$X_{\delta}$	Stability derivative of $X$ due to the deflection of the control surfaces

$x$	State vector
$\dot{x}$	State vector derivatives
$Y$	Side force
$Y_\beta$	Stability derivative of $Y$ due to a change in side slip angle
$Y_p$	Stability derivative of $Y$ due to a change in the roll rate
$Y_r$	Stability derivative of $Y$ due to a change in the yaw rate
$Y_\delta$	Stability derivative of $Y$ due to the deflection of the control surfaces
$y$	Output vector
$Z$	Normal force
$Z_u$	Stability derivative of $Z$ in $u$ -direction velocity
$Z_w$	Stability derivative of $Z$ in $w$ -direction velocity
$Z_q$	Stability derivative of $Z$ due to pitch rate
$Z_\delta$	Stability derivative of $Z$ due to the deflection of the control surfaces

## Greek Letters

$\alpha$	Angle of attack
$\beta$	Sideslip angle
$\gamma$	Flight path angle
$\theta$	Pitch attitude angle
$\phi$	Bank angle
$\psi$	Heading angle
$\lambda$	Eigenvalue
$\xi$	Damping ratio
$\omega_n$	Natural frequency
$\sigma$	Real part of a pole
$\omega$	Imaginary part of a pole
$\Lambda$	Wing sweep angle at $\bar{c}/4$ line
$\Lambda_f$	Forward wing sweep angle at $\bar{c}/4$ line
$\Lambda_a$	Aft wing sweep angle at $\bar{c}/4$ line
$\Gamma_f$	Dihedral forward wing
$\Gamma_a$	Dihedral aft wing
$\theta_f$	Twist forward wing
$\theta_a$	Twist aft wing
$\lambda_f$	Taper ratio forward wing
$\lambda_a$	Taper ratio aft wing
$\rho$	Density
$\nu$	Kinematic viscosity
$\mu$	Dynamic viscosity
$\delta_s$	Control surface deflection
$\delta_f$	Flaps deflection
$\delta_{a_i}$	Inboard aileron deflection
$\delta_{a_o}$	Outboard aileron deflection
$\delta_{e_i}$	Inboard elevator deflection
$\delta_{e_o}$	Outboard elevator deflection

## Abbreviations

<i>2-D</i>	Two-dimensional
<i>3-D</i>	Three-dimensional
<i>AFCS</i>	Automatic Flight Control System
<i>AFRL</i>	Air Force Research Laboratory
<i>AR</i>	Aspect Ratio
<i>AVL</i>	Athena Vortex Lattice
<i>AFA</i>	Academia Força Aérea Portuguesa
<i>CAD</i>	Computer-Aided Design
<i>CNC</i>	Computer Numerically Controlled
<i>CS</i>	Control Surface
<i>CFD</i>	Computational Fluid Dynamics
<i>cg</i>	Center of Gravity
<i>EDF</i>	Electric Ducted Fan
<i>HALE</i>	High-Altitude Long-Endurance
<i>ISR</i>	Intelligence, Surveillance and Reconnaissance
<i>JWS</i>	Joined-Wing Sensorcraft
<i>LQR</i>	Linear Quadratic Regulator
<i>ph</i>	Phugoid mode
<i>SI</i>	International System of Units
<i>sp</i>	Short period mode
<i>UAV</i>	Unmanned Aerial Vehicle
<i>US</i>	United States
<i>USAF</i>	United States Air Force
<i>VLM</i>	Vortex Lattice Method

# Chapter 1

## Introduction

The Joined-Wing SensorCraft inserts itself in a United States Air Force (USAF) project of a new generation of High-Altitude Long-Endurance (HALE) aircrafts. At this very moment, only small and scaled models have been constructed and experimented in flight tests. This Unmanned Aerial Vehicle (UAV) is a merging between stealth, endurance and a low-band array, able to provide 360° coverage. HALE UAVs have become an important part of the aeronautic field with great future perspectives. These vehicles have civilian as well as military applications, distinguished for remote sensing, telecommunications, atmospheric studies, along surveillance and reconnaissance, accomplished at relatively low operating costs [1].

The Joined-Wing aircraft is an unusual configuration that incorporates two wings in which the forward wing is swept back positive dihedral to join the aft wing, which is swept forward anhedral, usually from the top and front view forming a diamond arrangement [2].

The limitation to UAVs data collection was a lack in continuous area coverage and so low ability to penetrate dense foliage. A conformal radar antenna array embedded in such a diamond shape could afford 360° radar coverage thus improving the ability to see through thick forest canopies. This configuration is commonly referred to as a Sensorcraft.

The problem with the actual radars is that they have to be installed after the aircraft design, introducing a weight penalty and sometimes creating drag. Nowadays the aircrafts use in ever-more precise missions, increase the need of higher resolution from the sensor. Increasing the radar resolution means increasing the size of the sensor, which leads to even more weight and possibly more drag.

The Joined-Wing SensorCraft design was created for a new type of radar array that could work as part of the airframe. The main goal was having an aircraft with continuous area coverage, so it was designed around the antennas, and all the performance requirements obey firstly to the antenna requirements [1].

It can be said, that the genesis of the SensorCraft was the desire to integrate the sensing functionality into the airframe of an UAV, solving the problem of the actual radars.

The conformal antennas integrated in the aircraft improve the aerodynamic performance, thus maximize the endurance performance of the aircraft.

## 1.1 Development of the Joined-Wing concept

The Joined-Wing design is not a new concept at all. Although with some different names, like Close-Wing or Box-Wing, the concept emerged a century ago. It started with the Blériot III aircraft, built in 1906 by Louis Blériot and Gabriel Voisin [3]. Nevertheless, the huge advance in the Joined-Wing concept only took place in 1980's by Dr. Julian Wolkovitch, who suggested that this new design would lead to possible weight savings and aeroelastic benefits [4] [5].

The general aims of this design are to provide a Joined-Wing aircraft with:

- An improved strength to weight ratio
- A greater stiffness
- Less aerodynamic drag
- An improvement in wing structure for resistant out-of-plane lifting loads
- An improvement in terms of the buckling resistance

After Dr. J. Wolkovitch proposed this concept, several studies have been conducted to investigate structural and aerodynamic characteristics of the Joined-Wing. The benefits provided by the Joined-Wing depend on its application and design goals. For the same applications, weight saving may be of prime importance [6].

Some of the advantages stated for the Joined-Wing are:

- Light weight
- High stiffness
- Low induced drag
- Good transonic area distribution
- High trimmed maximum lift coefficient
- Reduced Wetted area and parasitic drag
- Direct lift control capability
- Direct side force control capability

Between these advantages, the weight saving, less drag and high trimmed, along with the improvement in surveillance and reconnaissance capability, make the Joined-Wing SensorCraft a promising advance in HALE UAVs.

Because of the great attention given to the surveillance and endurance abilities, the stability and control of the aircraft was not a primary concern. Thus this thesis will focus and treat this later subject, exploring the high number of control surfaces in the wings.

## 1.2 Thesis motivation

The Joined-Wing SensorCraft gave its first steps in the Air Force Research Laboratory. The development of this project aimed for a completely innovative design that could carry all the sensing capability that USAF currently have. The SensorCraft configurations are motivated by the capability they can provide in terms of altitude, range, endurance, payload capacity, surveillance, reconnaissance, and antenna systems with 360° coverage [7].

In order to explore different configurations for the Sensorcraft, many contracts were conducted between USAF and the United States' largest airframers, Northrop Grumman, Lockheed Martin and Boeing. An ambitious plan was proposed to the airframers that demanded them new challenges: high endurance capability, outstanding aerodynamic performance, great payload capacity, power and cooling to support a next-generation intelligence, surveillance and reconnaissance (ISR) sensor. From the airframers competition came three different designs, a conventional high aspect ratio wing, a Flying-Wing and the Joined-Wing [8].

The Joined-Wing Sensorcraft configuration belongs to the airframer Boeing and some work has been done by USAF partners, building and flight testing smaller SensorCraft models [9]. SensorCraft is a 5 meters wingspan UAV, with an overall mass of 93 Kg and 2 engines mounted inside the fuselage like shown in figure 1.1. It represents a challenge for stability and control not only because of the unusual configuration, but also because of a particular nonexistence of a vertical stabilizer and thus of the yaw control surface (rudder). Usual joined-wing configurations always preserve the vertical stabilizer; however the strict requisites of long endurance, and high aerodynamic performance led to this configuration.

The numerous control surfaces that was possible to install in both front and aft wings, contributed to the feasibility of mixed-control techniques on the SensorCraft.

### 1.3 Thesis objectives

The objectives of this thesis are the development of the static and dynamic stability analysis of the Joined-Wing SensorCraft, following the control of its unstable modes in order to achieve good handling flight properties, and finally exploring which best non rudder techniques can make the SensorCraft control feasible.

In order to accomplish such objectives, and due to the lack of wind tunnel tests, the aircraft performance will be analyzed with a Computational Fluid Dynamics (*CFD*) code program. After the calculation of the aircraft's stability derivatives, the static and dynamic stability analysis of the aircraft motion will take place. Conventional and modern control techniques will be applied as an effort to stabilize both longitudinal and lateral motions, but it will be placed more emphasis in the lateral motion control due to the nonexistence of a rudder.

### 1.4 Properties definitions

#### Axis System

The definition of the axis system is important since it is from it that the center of gravity (*cg*) will be represented, as well as the aerodynamic parameters used in the *AVL* program.

The axis system was built with the *X*-axis starting at aircraft nose and pointing to the tail aligned along the vehicle body. The *Z*-axis is perpendicular to *X*-axis and pointing up, with aircraft wings

leveled. Finally the  $Y$ -axis points out through the right wing, and creates a right-handed trihedron along with the two other axis.

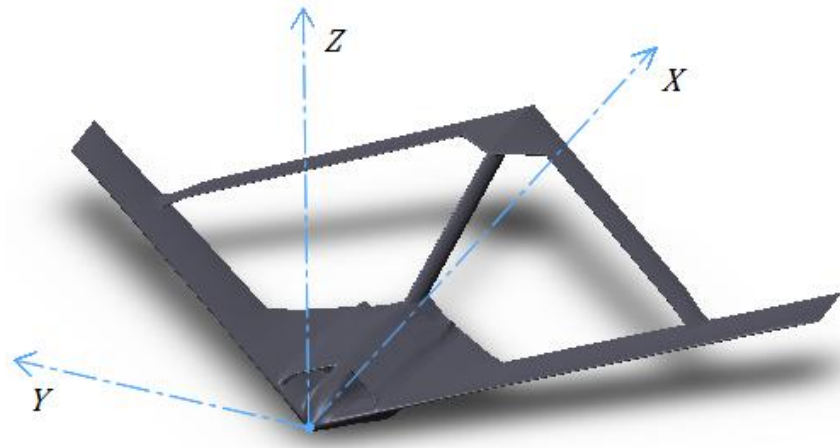


Figure 1.1 - Joined-Wing SensorCraft schematic, with axis system for cg and AVL data definition

### Direction of control surfaces

As notation for positive and negative direction of the deflection of control surfaces, it is defined a downwards deflection as a positive deflection (+), and an upwards deflection as a negative deflection (-).

Other definitions, like swept, dihedral, twist and taper ratio follow the conventional definitions. Further insight on these definitions can be seen in Appendix A.

## 1.6 Thesis layout

In Chapter 1, the theme of this thesis is approached through a history briefing about the joined-wing configuration aircrafts and the objectives of the thesis are lined out.

In Chapter 2 is presented the configuration of the Joined-Wing aircraft, as well as strategies to control rudderless aircrafts. The equations of motion for the aircraft are deduced.

In Chapter 3, the aerodynamic characteristics are calculated and estimated using various techniques.

In Chapter 4, the aircraft stability is investigated, a study about the stability derivatives impact on the control strategies is performed and ways to approach an equivalent rudder using the existent control surfaces are explored.

In Chapter 5 control systems are designed to stabilize and control the dynamic of aircraft, and the control systems are used to evaluate the different control strategies.

In Chapter 6, the results achieved in the previous chapter are analyzed and discussed in order to come up with the best solutions. It is presented an already built Joined-Wing SensorCraft heuristic model and the qualitative flight test results are compared with the theoretical results.

Finally, in Chapter 7 the conclusion about the several control systems studied are presented and recommendations are made for the aircraft control.

## Chapter 2

# Joined-Wing SensorCraft

As stated before, the Joined-Wing SensorCraft has a configuration that incorporates two wings in which the forward wing is swept back positive dihedral to join the aft wing, which is swept forward anhedral, creating a diamond shape that can be seen from top and front views (figure 2.1). The fuselage is linked to the end of the aft wing by a tail boom, granting better structural and aeroelasticity responses from the wings during the SensorCraft flight.

### 2.1 Configuration and aircraft properties

A peculiar characteristic of Joined-Wing SensorCraft, when compared with other Joined-Wing configurations is the nonexistence of vertical stabilizer, and therefore of a rudder to control the yaw. The schematic views of the Joined-Wing SensorCraft are presented below in figure 2.1.

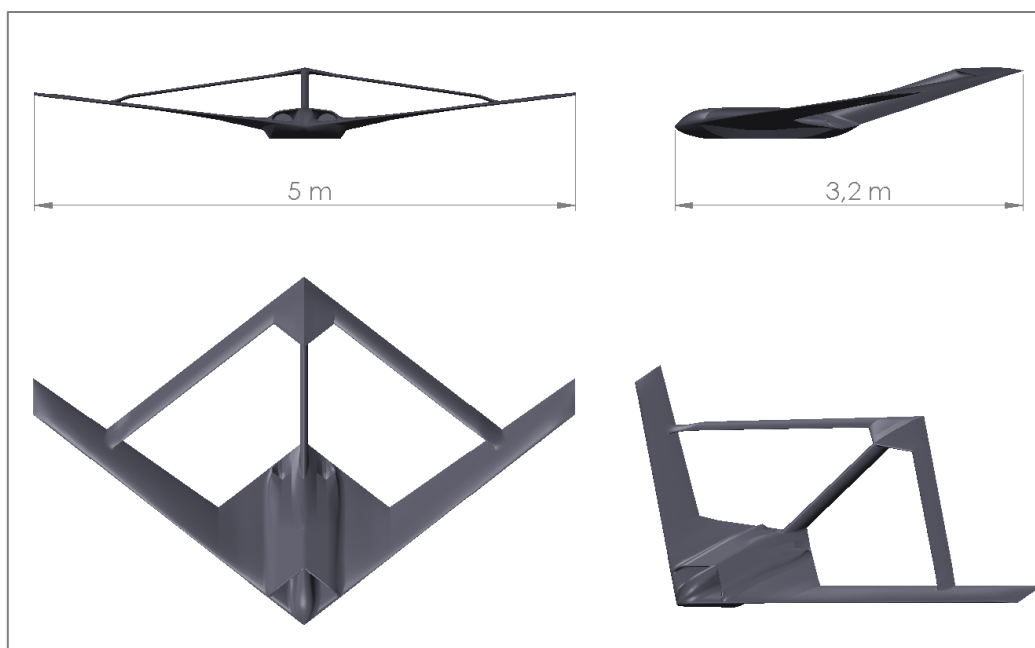


Figure 2.1 - Schematic views of the SensorCraft

The main characteristics and geometry parameters of SensorCraft can be seen in Appendix B as well as their definitions.

All the analysis will be ran for a trimmed, straight and symmetric flight, with wings leveled. As a consequence, lift equals weight. The flight condition parameters are given in table 2.1, where,  $U_0$  is the aircraft forward velocity,  $\rho$  is the air density for the given reference altitude  $h_0$ . The parameter  $\theta_0$  represents the aircraft pitch angle for the stated conditions and was calculated using the *AVL* program. The last parameter  $C_L$  represents the lift coefficient and is given in equation 2.1.

<b>Flight Conditions</b>	<b>Value</b>	<b>Unit</b>
$U_0$	25,9	<i>m/s</i>
$\rho$	1,225	<i>Kg/m<sup>3</sup></i>
$\theta_0$	4,5	<i>degrees</i>
$h_0$	0	<i>m</i>
$C_L$	1,13	–

**Table 2.1 - SensorCraft flight condition parameters**

The lift coefficient was calculated for the lift equal to weight condition as represented in following equations:  $L = W \Leftrightarrow \frac{1}{2}\rho U_0^2 S C_L = mg$ , resulting in the expression:

$$C_L = \frac{2mg}{\rho U_0^2 S}, \quad (2.1)$$

where,  $L$  is the lift force,  $W$  is the weight force and the other parameters were defined before or in Appendix B.

The SensorCraft has ten control surfaces along the forward and aft wings. Six control surfaces are located in the forward wing and the other four in the aft wing. The distribution of the control surfaces is shown in figure 2.2, and the table 2.3 makes the matching between the designation used for each control surface and the code assigned to it, which will be followed through this thesis. Symmetrical right and left control surfaces are defined by the same code.

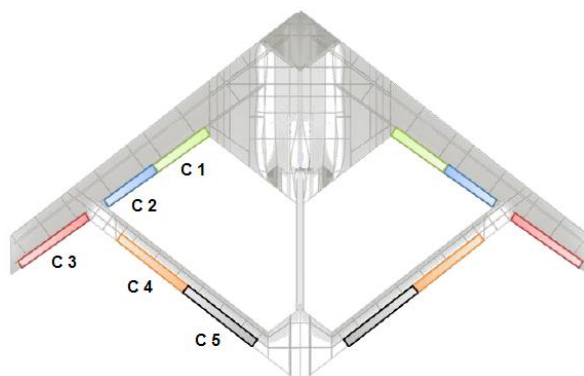


**Figure 2.2 - Control surfaces distribution**

<b>Control surface</b>	<b>Code</b>
Flaps	C1
Inboard Ailerons	C2
Outboard Ailerons	C3
Outboard Elevators	C4
Inboard Elevators	C5

**Table 2.2 - Legend of figure 2.2**

The SensorCraft will use two turbine engines mounted inside the fuselage, having an inlet and outlet configuration shown in figure 2.3.

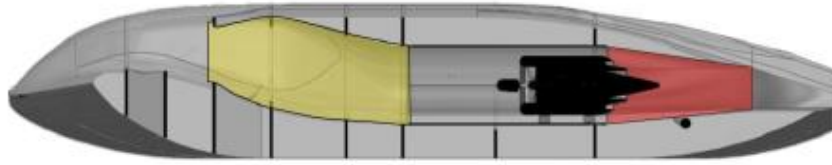


Figure 2.3 - Longitudinal section of the SensorCraft showing the engine position and the air inlet (yellow) outlet (red) configuration [9]

## 2.2 Control strategies in rudderless aircraft configurations

Due to the lack of vertical stabilizer and consequently of the yaw control surface (rudder), there was a need to explore modern techniques of controlling yaw motion. Three methods of yaw stability control were found and are described below.

### 2.2.1 Mixed-control method

The mixed-control purpose is to combine different control surfaces in order to produce a certain motion that would be impossible to achieve by the deflection of one single control surface. Mixed-control is also a method to make one control surface actuate over different motions, for example the elevon working as elevator (longitudinal motion) and aileron (roll motion) depending on the pilot's request.

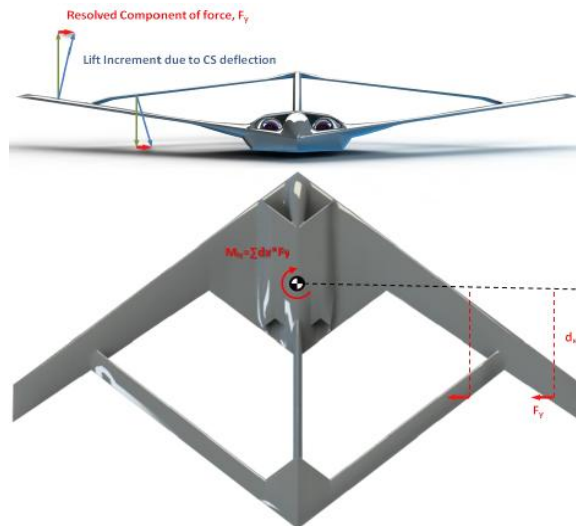


Figure 2.4 - Front and top views of mixed-control forces exemplification [9]

In figure 2.4, it is easily seen that a positive deflection on the right outboard aileron causes the appearance of an increment lift force (normal to the control surface) which has a lateral force contribution to the inboard of the aircraft. On the other hand, the negative deflection of the right outboard elevator has the same contribution of a force into the inboard of the aircraft. Given these contributions of lateral force and its distance to the *cg*, it is possible to create a yawing moment on the aircraft.

### 2.2.2 Speed-brake control method

Speed-brake control works on deflecting a control surface of one wing in order to produce a differential drag force between the wings. This differential force will create a yaw moment and will be used to lateral control. It is commonly used through split control surfaces, where it deflects up and downwards to create drag.



Figure 2.5 - Aircraft B-2 Spirit using speed-brake control [10]

### 2.2.3 Differential thrust control method

Differential thrust is acquired by creating a differential thrust force between the engines, giving more power to one and less to the other, for example. The yaw control results from these differential forces which create a yaw moment.

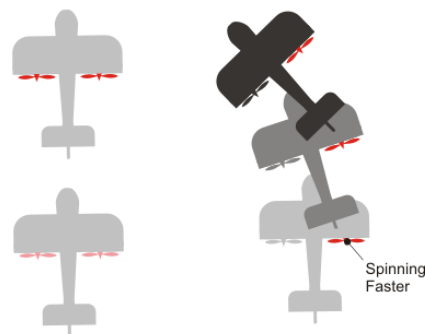


Figure 2.6 - Exemplification of differential thrust control method [11]

### 2.2.4 Resume

Two control strategies will be explored in the control of the SensorCraft, since the engines are mounted very close to the aircraft  $X$ -axis, the yawing moment produced would be very small. Therefore, this third method will not be considered and only the first two methods will be analyzed.

## 2.3 Dynamics of flight

### 2.3.1 Axis referring

First of all it is essential to analyze the physical characteristics of the system and to mathematically describe it, allowing the development of the required control algorithms. For this particular flight control application the physical characteristics of the system are based around the flight dynamics of the aircraft.

The first step in the analysis of the flight dynamics of any aircraft is to develop an initial reference axis system to describe the position and attitude of the aircraft in relation to the Earth. The most convenient inertial reference frame to use is known as the tropocentric coordinate system or Earth axis system; where the origin of this axis is regarded as being fixed at the centre of the Earth. Figure 2.7 represents this system [12].

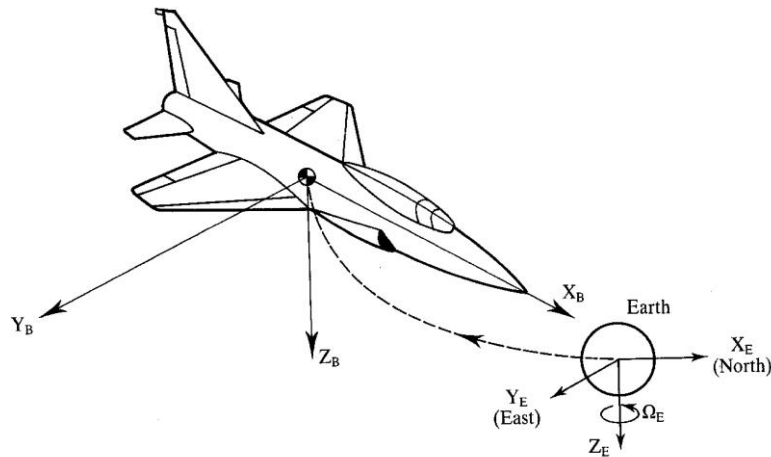


Figure 2.7 - Aircraft Earth axis system [12]

To complement the Earth axis system and to characterize the aircraft in relation to this initial Earth reference frame, the aircraft itself must also be referenced by a suitable axis system. The system chosen for this project is the body-fixed axis system. This system and its components are presented in figure 2.8 [12].

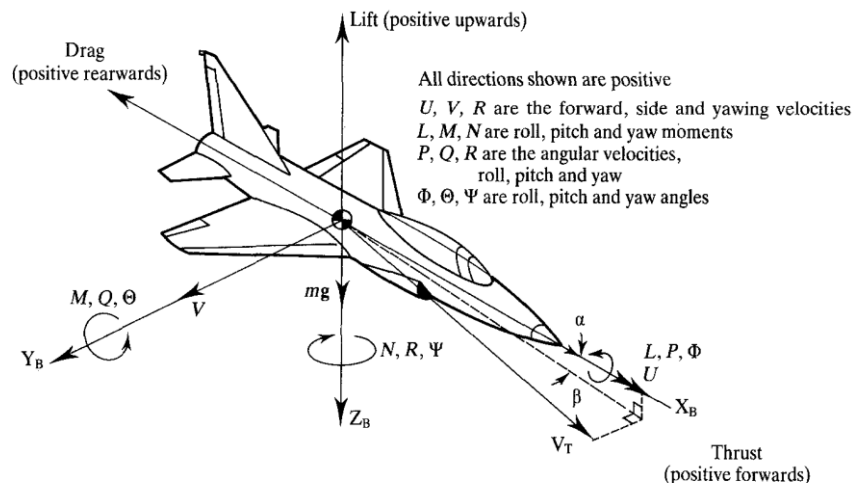


Figure 2.8 - Aircraft body-fixed axis system [12]

From the body-fixed axis system, it can be deduced a commonly used axis named Stability axis system. In the Stability axis system, the axis  $X_s$  is chosen to coincide with the velocity vector at the start of the motion, thus steady symmetric flight. Therefore, between the  $X$ -axis of stability axis system and the  $X$ -axis of the body axis system, there is a difference of a trimmed angle of attack,  $\alpha_0$  and the sideslip angle ( $\beta$ ) is considered to be zero at start of motion.

The definition of both axis systems is essential to determine the equations of motion that will describe the attitude of the aircraft at any point in time. As shown in figure 2.8, there are six degrees of freedom in any aircraft system, consisting of longitudinal ( $X$ ), lateral ( $Y$ ) and vertical ( $Z$ ) translational motions, roll ( $L$ ), pitch ( $M$ ) and yaw ( $N$ ) rotational motions about the aircraft's center of gravity.

### 2.3.2 Euler's Equations of Motion

To describe the six degrees of freedom the following equations, known as Euler's Equations of Motion, have been derived from Newton's Second Law and are essential for the development of any flight control system. These equations are described in the body-fixed axis system, which is in motion with respect to the Earth axis system, considered to be an inertial system.

$$\Delta X = m(\dot{U} + QW - VR), \quad (2.2)$$

$$\Delta Y = m(\dot{V} + UR - PW), \quad (2.3)$$

$$\Delta Z = m(\dot{W} + VP - UQ), \quad (2.4)$$

$$L = I_{xx}\dot{P} - I_{xz}(\dot{R} + PQ) + (I_{zz} - I_{yy})QR, \quad (2.5)$$

$$M = I_{yy}\dot{Q} + I_{xz}(P^2 - R^2) + (I_{xx} - I_{zz})PR, \quad (2.6)$$

$$N = I_{zz}\dot{R} - I_{xz}\dot{P} + PQ(I_{yy} - I_{xx}) + I_{xz}QR, \quad (2.7)$$

where, these variables are defined in figure 2.8,  $W$  is the vertical velocity and other parameters are defined in Appendix B.

The equations (2.2 – 2.7) represent the inertial forces and moments acting on the aircraft. For completeness it becomes necessary to characterize the contribution of the forces due to gravity. Gravity forces will affect only the translational dynamics of the aircraft and are described in below:

$$\delta X = -mg \sin \Theta, \quad (2.8)$$

$$\delta Y = mg \cos \Theta \sin \Phi, \quad (2.9)$$

$$\delta Z = mg \cos \Theta \cos \Phi, \quad (2.10)$$

where,  $\delta X$ ,  $\delta Y$  and  $\delta Z$  are the incremental forces due to the gravity, and the angles are defined in figure 2.8.

Now that both the inertial forces of the aircraft and the contributions made by gravity have been quantified, the equations can be combined to produce the complete equations of motion of the aircraft for its six degrees of freedom.

$$\Delta X = m(\dot{U} + QW - VR + g \sin \Theta), \quad (2.11)$$

$$\Delta Y = m(\dot{V} + UR - PW - g \cos \Theta \sin \Phi), \quad (2.12)$$

$$\Delta Z = m(\dot{W} + VP - UQ - g \cos \Theta \cos \Phi), \quad (2.13)$$

$$L = I_{xx}\dot{P} - I_{xz}(\dot{R} + PQ) + (I_{zz} - I_{yy})QR, \quad (2.14)$$

$$M = I_{yy}\dot{Q} + I_{xz}(P^2 - R^2) + (I_{xx} - I_{zz})PR, \quad (2.15)$$

$$N = I_{zz}\dot{R} - I_{xz}\dot{P} + PQ(I_{yy} - I_{xx}) + I_{xz}QR. \quad (2.16)$$

To complement the equations (2.11 – 2.16), it is also important to account with the equations which relate the Euler angles ( $\Phi$ ,  $\Theta$  and  $\Psi$ ) to the angular velocities ( $P$ ,  $Q$  and  $R$ ). These equations are defined as follows.

$$P = \dot{\Phi} - \dot{\Psi} \sin \Theta, \quad (2.17)$$

$$Q = \dot{\Theta} \cos \Phi + \dot{\Psi} \cos \Theta \sin \Phi, \quad (2.18)$$

$$R = -\dot{\Theta} \sin \Phi + \dot{\Psi} \cos \Theta \cos \Phi. \quad (2.19)$$

### 2.3.3 Small disturbance theory - linearization

From the previous nine equations (2.11 – 2.19), the aircraft motion can be described using the small disturbance theory. This theory essentially describes all of the motion variables in the equations of motion as having two components, a reference (or equilibrium) component and a dynamic (or perturbation) component as shown in the follow expressions.

$$\begin{aligned} U &= U_0 + u, & P &= P_0 + p, & X &= X_0 + x, & L &= L_0 + l, \\ V &= V_0 + v, & Q &= Q_0 + q, & Y &= Y_0 + y, & M &= M_0 + m, \\ W &= W_0 + w, & R &= R_0 + r, & Z &= Z_0 + z, & N &= N_0 + n. \end{aligned} \quad (2.20)$$

In equations (2.20), the reference values are denoted by the subscript 0, while the perturbation values about the equilibrium condition are denoted by the lower case letter.

In order to apply the small disturbance theory it is required to define both equilibrium and perturbation equations. In equilibrium conditions there can be no translational or rotational acceleration, thus the equilibrium equations are expressed as shown below [12]:

$$X_0 = m(Q_0W_0 - V_0R_0 + g \sin \Theta_0), \quad (2.21)$$

$$Y_0 = m(U_0R_0 - P_0W_0 - g \cos \Theta_0 \sin \Phi_0), \quad (2.22)$$

$$Z_0 = m(V_0P_0 - U_0Q_0 - g \cos \Theta_0 \cos \Phi_0), \quad (2.23)$$

$$L_0 = -I_{xz}P_0Q_0 + (I_{zz} - I_{yy})Q_0R_0, \quad (2.24)$$

$$M_0 = I_{xz}(P_0^2 - R_0^2) + (I_{xx} - I_{zz})P_0R_0, \quad (2.25)$$

$$N_0 = P_0Q_0(I_{yy} - I_{xx}) + I_{xz}Q_0R_0, \quad (2.26)$$

$$P_0 = \dot{\Phi}_0 - \dot{\Psi}_0 \sin \Theta_0, \quad (2.27)$$

$$Q_0 = \dot{\Theta}_0 \cos \Phi_0 + \dot{\Psi}_0 \cos \Theta_0 \sin \Phi_0, \quad (2.28)$$

$$R_0 = -\dot{\Theta}_0 \sin \Phi_0 + \dot{\Psi}_0 \cos \Theta_0 \cos \Phi_0. \quad (2.29)$$

To find the expressions of the perturbed motion, it was applied the small perturbation theory following the equation:

$$dX = (X_0 + x) - X_0. \quad (2.30)$$

The term  $(X_0 + x)$  is obtained by replacing equations (2.20) into the equations (2.11 – 2.19). The perturbation equations describing the small disturbances from the equilibrium condition are represented below:

$$dX = m[\dot{u} + W_0q + Q_0w - V_0r - R_0v + (g \cos \Theta_0) \theta], \quad (2.31)$$

$$dY = m[\dot{v} + U_0r + R_0u - W_0p - P_0w - (g \cos \Theta_0 \cos \Phi_0) \phi + (g \sin \Theta_0 \sin \Phi_0) \theta], \quad (2.32)$$

$$dZ = m[\dot{w} + V_0p + P_0v - U_0q - Q_0u + (g \cos \Theta_0 \sin \Phi_0) \phi + (g \sin \Theta_0 \cos \Phi_0) \theta], \quad (2.33)$$

$$dL = I_{xx}\dot{p} - I_{xz}\dot{r} + (I_{zz} - I_{yy})(Q_0r + R_0q) - I_{xz}(P_0q + Q_0p), \quad (2.34)$$

$$dM = I_{yy}\dot{q} + (I_{xx} - I_{zz})(P_0r + R_0p) - I_{xz}(2R_0r - 2P_0p), \quad (2.35)$$

$$dN = I_{zz}\dot{r} - I_{xz}\dot{p} + (I_{yy} - I_{xx})(P_0q + Q_0p) + I_{xz}(Q_0r + R_0q), \quad (2.36)$$

$$p = \dot{\phi} - (\dot{\Psi}_0 \cos \Theta_0) \theta - \dot{\psi} \sin \Theta_0, \quad (2.37)$$

$$q = \dot{\theta} \cos \Phi_0 - \theta(\dot{\Psi}_0 \sin \Theta_0 \sin \Phi_0) + \dot{\psi} \cos \Theta_0 \sin \Phi_0 + \phi(\dot{\Psi}_0 \cos \Theta_0 \cos \Phi_0 - \dot{\Theta}_0 \sin \Phi_0), \quad (2.38)$$

$$r = \dot{\psi} \cos \Theta_0 \cos \Phi_0 - \phi(\dot{\Psi}_0 \cos \Theta_0 \sin \Phi_0 + \dot{\Theta}_0 \cos \Phi_0) - \dot{\theta} \sin \Phi_0 - \theta(\dot{\Psi}_0 \sin \Theta_0 \cos \Phi_0). \quad (2.39)$$

After applying the small disturbance theory, simplification is needed to adapt the equations into a form that will be easier to analyze and implement an automated control system. It becomes necessary to analyze the motion variables for a given flight condition. What is commonly done in Automatic Flight Control System (AFCS) studies is to consider flight cases with simpler trim conditions, like stated before in subsection 2.1. These conditions and respective simplifications are:

- Straight flight implies:  $\dot{\Psi}_0 = \dot{\Theta}_0 = 0$ ; (2.40)

- Symmetric flight implies:  $\Psi_0 = V_0 = 0$ ; (2.41)

- Flying with wings leveled implies:  $\Phi_0 = 0$ ; (2.42)

- Trimmed flight implies:  $P_0 = Q_0 = R_0 = 0$ . (2.43)

Another simplification that can be made is that the product of inertia  $I_{xy} = 0$ , that comes from the table (2.1).

It becomes possible to rewrite the equations in this new form with reference to the above flight conditions. Note that in equations (2.31 – 2.39), the notation  $dX$  was replaced by  $x$  only.

$$x = m[ \dot{u} + W_0 q + (g \cos \Theta_0) \theta ], \quad (2.44)$$

$$y = m[ \dot{v} + U_0 r - W_0 p - (g \cos \Theta_0) \phi ], \quad (2.45)$$

$$z = m[ \dot{w} - U_0 q + (g \sin \Theta_0) \theta ], \quad (2.46)$$

$$l = I_{xx} \dot{p}, \quad (2.47)$$

$$m = I_{yy} \dot{q}, \quad (2.48)$$

$$n = I_{zz} \dot{r}, \quad (2.49)$$

$$\dot{\phi} = p + r \tan \Theta_0, \quad (2.50)$$

$$\dot{\theta} = q, \quad (2.51)$$

$$\dot{\psi} = r \sec \Theta_0. \quad (2.52)$$

The equations (2.50) and (2.52) were combined to rewrite the equations in order of  $\dot{\phi}$  and  $\dot{\psi}$ . The equations for  $x$ ,  $z$  and  $m$  are referred to as equations of longitudinal motion as they deal with all motion in the  $XZ$ -plane. Equations for  $y$ ,  $l$  and  $n$  are referred to as equations of lateral/directional motion as they deal with all motion in the  $XY$ -plane. It is notable the separation of lateral and longitudinal equations, which result from the trim conditions applied.

### 2.3.4 Equations of longitudinal motion

The final step to complete the linearized equations of motion is to expand the left-hand side of these equations. To do this, an expansion in Taylor series of the aerodynamic forces and moment terms is used about the trimmed flight condition.

$$\begin{aligned} \frac{\partial X}{\partial u} u + \frac{\partial X}{\partial \dot{u}} \dot{u} + \frac{\partial X}{\partial w} w + \frac{\partial X}{\partial \dot{w}} \dot{w} + \frac{\partial X}{\partial q} q + \frac{\partial X}{\partial \dot{q}} \dot{q} + \frac{\partial X}{\partial \delta_s} \delta_s + \frac{\partial X}{\partial \dot{\delta}_s} \dot{\delta}_s = \\ = m[\dot{u} + W_0 q + (g \cos \Theta_0) \theta], \end{aligned} \quad (2.53)$$

$$\begin{aligned} \frac{\partial Z}{\partial u} u + \frac{\partial Z}{\partial \dot{u}} \dot{u} + \frac{\partial Z}{\partial w} w + \frac{\partial Z}{\partial \dot{w}} \dot{w} + \frac{\partial Z}{\partial q} q + \frac{\partial Z}{\partial \dot{q}} \dot{q} + \frac{\partial Z}{\partial \delta_s} \delta_s + \frac{\partial Z}{\partial \dot{\delta}_s} \dot{\delta}_s = \\ = m[\dot{w} - U_0 q + (g \sin \Theta_0) \theta], \end{aligned} \quad (2.54)$$

$$\frac{\partial M}{\partial u} u + \frac{\partial M}{\partial \dot{u}} \dot{u} + \frac{\partial M}{\partial w} w + \frac{\partial M}{\partial \dot{w}} \dot{w} + \frac{\partial M}{\partial q} q + \frac{\partial M}{\partial \dot{q}} \dot{q} + \frac{\partial M}{\partial \delta_s} \delta_s + \frac{\partial M}{\partial \dot{\delta}_s} \dot{\delta}_s = I_{yy} \dot{q}. \quad (2.55)$$

Note,  $\delta_s$  is the change in deflection of a control surface defined by  $S$ .

To simplify the notation, it was made the following usual substitutions:

$$X_i = \frac{1}{m} \frac{\partial X}{\partial i}, \quad Z_i = \frac{1}{m} \frac{\partial Z}{\partial i}, \quad M_i = \frac{1}{I_{yy}} \frac{\partial M}{\partial i},$$

where, the coefficients  $X_i$ ,  $Z_i$  and  $M_i$  are referred as stability derivatives.

Without loss of generality it can be assumed that the following stability derivatives are often negligible, and so they may be ignored [12]:

$$X_{\dot{u}}, X_{\dot{w}}, X_q, X_{\dot{q}}, X_{\dot{\delta}_s}, Z_{\dot{u}}, Z_{\dot{w}}, Z_q, Z_{\dot{q}}, Z_{\dot{\delta}_s}, M_{\dot{u}}, M_{\dot{q}} \text{ and } M_{\dot{\delta}_s}.$$

It was decided to pass to the stability axis system to make equations even simpler, in which  $W_0 = 0$  and  $\Theta_0 = \gamma_0$ .

Therefore, considering for completeness the equation 2.51, ignoring the above negligible stability derivatives, applying the change to the stability axis system and rearranging the expression of longitudinal motion it takes the following form.

$$\dot{u} = X_u u + X_w w - (g \cos \gamma_0) \theta + X_{\delta_s} \delta_s, \quad (2.56)$$

$$\dot{w} = Z_u u + Z_w w + (Z_q + U_0) q - (g \sin \gamma_0) \theta + Z_{\delta_s} \delta_s, \quad (2.57)$$

$$\dot{q} = M_u u + M_w w + M_{\dot{w}} \dot{w} + M_q q + M_{\delta_s} \delta_s, \quad (2.58)$$

$$\dot{\theta} = q. \quad (2.59)$$

To simplify the equation (2.58), the  $\dot{w}$  equation was replaced in the  $\dot{q}$  equation, resulting in the following system:

$$\dot{u} = X_u u + X_w w - (g \cos \gamma_0) \theta + X_{\delta_s} \delta_s, \quad (2.60)$$

$$\dot{w} = Z_u u + Z_w w + (Z_q + U_0) q - (g \sin \gamma_0) \theta + Z_{\delta_s} \delta_s, \quad (2.61)$$

$$\dot{q} = \tilde{M}_u u + \tilde{M}_w w + \tilde{M}_q q + \tilde{M}_\theta \theta + M_{\delta_s} \delta_s, \quad (2.62)$$

$$\dot{\theta} = q. \quad (2.63)$$

Note, for more details on the definitions of the tilde stability derivatives and the substitution see Appendix C.

### 2.3.5 Equations of lateral motion

For the lateral motion equations we will proceed in the same way as the longitudinal equations. So expanding in Taylor series the left-hand of the lateral equations, it takes the following form:

$$\begin{aligned} \frac{\partial Y}{\partial v} v + \frac{\partial Y}{\partial \dot{v}} \dot{v} + \frac{\partial Y}{\partial r} r + \frac{\partial Y}{\partial \dot{r}} \dot{r} + \frac{\partial Y}{\partial p} p + \frac{\partial Y}{\partial \dot{p}} \dot{p} + \frac{\partial Y}{\partial \delta_s} \delta_s + \frac{\partial Y}{\partial \dot{\delta}_s} \dot{\delta}_s \\ = m [ \dot{v} + U_0 r - W_0 p - (g \cos \Theta_0) \phi ], \end{aligned} \quad (2.64)$$

$$\frac{\partial L}{\partial v} v + \frac{\partial L}{\partial \dot{v}} \dot{v} + \frac{\partial L}{\partial r} r + \frac{\partial L}{\partial \dot{r}} \dot{r} + \frac{\partial L}{\partial p} p + \frac{\partial L}{\partial \dot{p}} \dot{p} + \frac{\partial L}{\partial \delta_s} \delta_s + \frac{\partial L}{\partial \dot{\delta}_s} \dot{\delta}_s = I_{xx} \dot{p}, \quad (2.65)$$

$$\frac{\partial N}{\partial v} v + \frac{\partial N}{\partial \dot{v}} \dot{v} + \frac{\partial N}{\partial r} r + \frac{\partial N}{\partial \dot{r}} \dot{r} + \frac{\partial N}{\partial p} p + \frac{\partial N}{\partial \dot{p}} \dot{p} + \frac{\partial N}{\partial \delta_s} \delta_s + \frac{\partial N}{\partial \dot{\delta}_s} \dot{\delta}_s = I_{zz} \dot{r}. \quad (2.66)$$

Adopting the above convenient notation for stability derivatives:

$$Y_j = \frac{1}{m} \frac{\partial Y}{\partial j}, \quad L_j = \frac{1}{I_{xx}} \frac{\partial L}{\partial j}, \quad N_j = \frac{1}{I_{zz}} \frac{\partial N}{\partial j},$$

the following lateral stability derivatives may be neglected:

$$Y_{\dot{v}}, Y_{\dot{p}}, Y_{\dot{r}}, Y_{\dot{\delta}_s}, L_{\dot{v}}, L_{\dot{p}}, L_{\dot{r}}, L_{\dot{\delta}_s}, N_{\dot{v}}, N_{\dot{p}}, N_{\dot{r}} \text{ and } N_{\dot{\delta}_s}.$$

As in the longitudinal motion case, the stability axis system will also be used for the lateral motion, in which  $W_0 = 0$  and  $\Theta_0 = \gamma_0$ .

Considering the above assumptions and the equations  $\dot{\phi}$  and  $\dot{\psi}$  to complete the equations (2.64 – 2.66), the equations of lateral motion are finally given by:

$$\dot{v} = Y_v v + Y_p p + (Y_r - U_0) r + (g \cos \gamma_0) \phi + Y_{\delta_s} \delta_s, \quad (2.67)$$

$$\dot{p} = L_v v + L_p p + L_r r + L_{\delta_s} \delta_s, \quad (2.68)$$

$$\dot{r} = N_v v + N_p p + N_r r + N_{\delta_s} \delta_s, \quad (2.69)$$

$$\dot{\phi} = p + r \tan \gamma_0, \quad (2.70)$$

$$\dot{\psi} = r \sec \gamma_0. \quad (2.71)$$

The sideslip angle  $\beta$  is preferred as a state variable, instead of the sideslip velocity  $v$ , due to the easily comprehension of the aircraft attitude. The relation between these variables, for small angles, is:  $v = U_0 \beta \Rightarrow \dot{v} = U_0 \dot{\beta}$ .

Finally the equations (2.67 – 2.71) can be rewritten into the following expressions:

$$\dot{\beta} = Y_\beta \beta + \frac{Y_p}{U_0} p + \left( \frac{Y_r}{U_0} - 1 \right) r + \left( \frac{g}{U_0} \cos \gamma_0 \right) \phi + \frac{Y_{\delta_s}}{U_0} \delta_s, \quad (2.72)$$

$$\dot{p} = L_\beta \beta + L_p p + L_r r + L_{\delta_s} \delta_s, \quad (2.73)$$

$$\dot{r} = N_\beta \beta + N_p p + N_r r + N_{\delta_s} \delta_s, \quad (2.74)$$

$$\dot{\phi} = p + r \tan \gamma_0, \quad (2.75)$$

$$\dot{\psi} = r \sec \gamma_0. \quad (2.76)$$

See Appendix D for more details about the transformation of sideslip velocity into sideslip angle.

## 2.4 State space representation of the equations of motion

The longitudinal and lateral systems described in equations (2.60 – 2.63) and (2.72 – 2.76), can be represented in a state space form for control system design and simulation purposes. This system is represented by the following scheme.

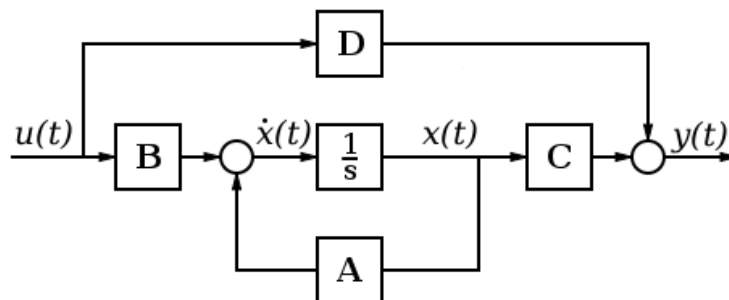


Figure 2.9 - State space block diagram [13]

Mathematically the block diagram in figure 2.9 can be represented as the following state space equations shown in equations (2.77) and (2.78).

$$\dot{x} = Ax + Bu, \quad (2.77)$$

$$y = Cx + Du, \quad (2.78)$$

where:

- $x$  is the state vector which represents the state variables;
- $u$  is the control vector which represents the control input variables;
- $y$  is the output vector;
- $A$  represents the state coefficient matrix;
- $B$  represents the driving matrix;
- $C$  represents the output matrix;
- $D$  represents the direct matrix.

### 2.4.1 Longitudinal system

The longitudinal equations shown in equations (2.60 – 2.63) can be represented in state space matrix form as shown in equations (2.77) and (2.78) in the following manner.

$$\begin{bmatrix} \dot{u} \\ \dot{w} \\ \dot{q} \\ \dot{\theta} \end{bmatrix} = \begin{bmatrix} X_u & X_w & 0 & -g \cos \gamma_0 \\ Z_u & Z_w & Z_q + U_0 & -g \sin \gamma_0 \\ \tilde{M}_u & \tilde{M}_w & \tilde{M}_q & \tilde{M}_\theta \\ 0 & 0 & 1 & 0 \end{bmatrix} \begin{bmatrix} u \\ w \\ q \\ \theta \end{bmatrix} + \begin{bmatrix} X_{\delta_{s1}} & X_{\delta_{s2}} \\ Z_{\delta_{s1}} & Z_{\delta_{s2}} \\ M_{\delta_{s1}} & M_{\delta_{s2}} \\ 0 & 0 \end{bmatrix} \dots \begin{bmatrix} \delta_{s1} \\ \delta_{s2} \\ \vdots \end{bmatrix}, \quad (2.79)$$

$$y = \begin{bmatrix} 1 & 0 & 0 & 0 \\ 0 & 1 & 0 & 0 \\ 0 & 0 & 1 & 0 \\ 0 & 0 & 0 & 1 \end{bmatrix} \begin{bmatrix} u \\ w \\ q \\ \theta \end{bmatrix} + \begin{bmatrix} 0 & 0 \\ 0 & 0 \\ 0 & 0 \\ 0 & 0 \end{bmatrix} \dots \begin{bmatrix} \delta_{s1} \\ \delta_{s2} \\ \vdots \end{bmatrix},$$

Note,  $\delta_{s_n}$  represents the  $n$  control surfaces possible to incorporate into the system.

### 2.4.2 Lateral system

The lateral equations (2.72 – 2.76) are represented in state space matrix in the same way as the longitudinal equations. The state space matrix of lateral motion is in equation (2.80).

$$\begin{bmatrix} \dot{\beta} \\ \dot{p} \\ \dot{r} \\ \dot{\phi} \\ \dot{\psi} \end{bmatrix} = \begin{bmatrix} Y_\beta & \frac{Y_p}{U_0} & \left(\frac{Y_r}{U_0} - 1\right) & \left(\frac{g}{U_0} \cos \gamma_0\right) & 0 \\ L_\beta & L_p & L_r & 0 & 0 \\ N_\beta & N_p & N_r & 0 & 0 \\ 0 & 1 & \tan \gamma_0 & 0 & 0 \\ 0 & 0 & \sec \gamma_0 & 0 & 0 \end{bmatrix} \begin{bmatrix} \beta \\ p \\ r \\ \phi \\ \psi \end{bmatrix} + \begin{bmatrix} \frac{Y_{\delta_{s1}}}{U_0} & \frac{Y_{\delta_{s2}}}{U_0} \\ L_{\delta_{s1}} & L_{\delta_{s2}} \\ N_{\delta_{s1}} & N_{\delta_{s2}} \\ 0 & 0 \\ 0 & 0 \end{bmatrix} \dots \begin{bmatrix} \delta_{s1} \\ \delta_{s2} \\ \vdots \end{bmatrix}, \quad (2.80)$$

$$y = \begin{bmatrix} 1 & 0 & 0 & 0 & 0 \\ 0 & 1 & 0 & 0 & 0 \\ 0 & 0 & 1 & 0 & 0 \\ 0 & 0 & 0 & 1 & 0 \\ 0 & 0 & 0 & 0 & 1 \end{bmatrix} \begin{bmatrix} \beta \\ p \\ r \\ \phi \\ \psi \end{bmatrix} + \begin{bmatrix} 0 & 0 \\ 0 & 0 \\ 0 & 0 \\ 0 & 0 \\ 0 & 0 \end{bmatrix} \dots \begin{bmatrix} \delta_{s1} \\ \delta_{s2} \\ \vdots \end{bmatrix}.$$

Note,  $\delta_{s_n}$  represents the  $n$  control surfaces possible to incorporate into the system.

To analyze the stability of the SensorCraft it is then necessary to find the stability derivatives in the longitudinal and lateral systems, which is presented in Chapter 3.

## Chapter 3

# Stability Coefficients of SensorCraft

To determine the stability coefficients of the aircraft, it is necessary to run either wind tunnel tests with the aircraft model or a *CFD* code program to simulate the air flow over the computed surface of the aircraft.

Since wind tunnel aerodynamic data was not available and there was no model to perform the tests, an *CFD* analysis was conducted.

### 3.1 Determination of stability coefficients using *AVL*

#### 3.1.1 Introduction to *AVL* – Vortex Lattice Method

The program chosen to proceed with the *CFD* analysis was the Athena Vortex Lattice (*AVL*). *AVL* is a numerical *CFD* code that uses the vortex lattice method (*VLM*). *VLM* models the lifting surfaces of an aircraft as an infinitely thin sheet of discrete vortices to compute lift and induced drag in an inviscid flow. Therefore there are some parameters neglected such as the influence of the thickness and the viscosity [14] [15].

This program was chosen because of the simple and fast analysis that can be performed, assuring convergence for few iterations. However, the results would be more reliable with a more complex *CFD* code or with wind tunnel tests.

#### 3.1.2 Modeling and *AVL* analysis

The creation of the *AVL* SensorCraft surfaces started assuming the *AVL* axes, which are the same as described in figure 1.1.

To create the surfaces it is required to define the various longitudinal sections of the aircraft (wing and fuselage airfoils). The lifting surfaces, which represent the mean surfaces between the various sections, as well as their geometry and aerodynamic parameters defined next, are computed by a linear interpolation between the points of the different sections.

For each section it is defined the respective geometry and aerodynamic parameters, given by:

- Leading edge position relative to *AVL* axis
- Airfoil chord
- Airfoil angle of attack
- Airfoil shape
- Lift curve slope of the airfoil  $dC_L/d\alpha$
- 3 points of the Drag-Polar curve:  $C_l$  vs  $C_d$
- Hinge position

where,  $C_l$  and  $C_d$  represent the lift and drag coefficients of the airfoil sections, respectively.

In order to improve the results, and since *AVL* does not consider viscosity and thickness effects, it was calculated and introduced in the *AVL* file the profile-drag from the Drag-Polar curve, the airfoil shape and its lift curve slope  $dC_l/d\alpha$  of each section (airfoil). However, the drag-polar will not affect the control surfaces derivatives, since it is just related to the airfoil. For further insight on *AVL* data see Appendix E.

The division into sections of the SensorCraft was performed attending the control surfaces distribution and the shape of the aircraft, as can be seen in figure 3.1. Each number represents a different airfoil, which respective airfoil coordinate data can be seen in Appendix L.

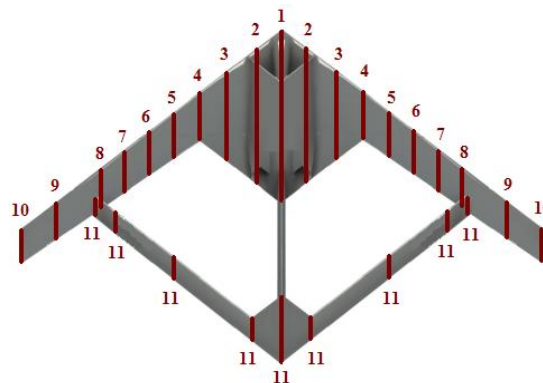


Figure 3.1 - *AVL* sections localization

For the numerical calculation proceed, the number of chordwise and spanwise horseshoe vortices and its spacing distribution must be defined as well. These values were chosen carefully to assure convergence of the results. The *AVL* SensorCraft model for analysis is represented in figure 3.2 in two different views.

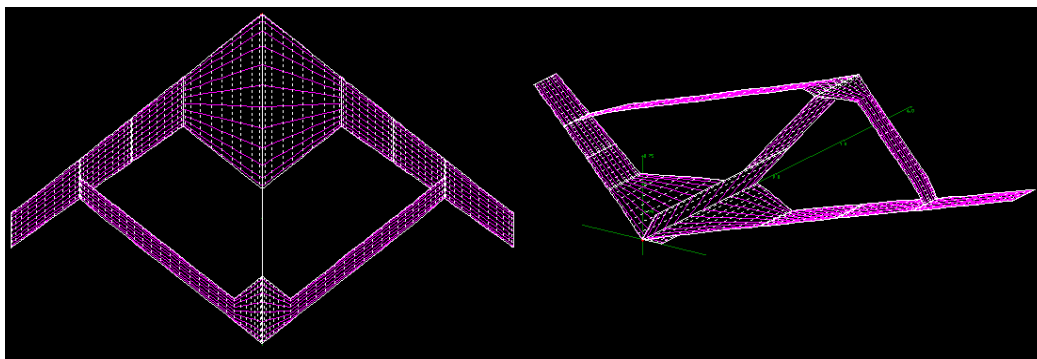


Figure 3.2 - *AVL* SensorCraft model

### 3.1.3 AVL results

After the aircraft surface modeling and the surface meshing the AVL analysis was performed, assuming the trimmed conditions given by the equations (2.40) - (2.43) and by Table 2.2.

After a few iterations the convergence was achieved and the aerodynamic data was determined. The results of the stability derivatives for the SensorCraft are presented in Appendix F.

### 3.1.4 Results interpretation

All the stability coefficients computed are dimensionless, except the stability coefficients in order to  $\alpha$  and  $\beta$  that are usually given in  $rad^{-1}$ . However, the control related stability coefficients in AVL are given in  $degree^{-1}$ . Therefore, all control related stability coefficients must be transformed into  $rad^{-1}$ . The transformation applied is in equation (3.1).

$$\frac{1}{degree} = \frac{1}{\frac{\pi}{180}rad} = \frac{180}{\pi} \frac{1}{rad} \quad (3.1)$$

The stability coefficients are dimensionless quantities of the stability derivatives, corresponding to the variation of forces and moments with the linear velocities, angular velocities or angles. In order to make these quantities dimensionless they are divided by the aircraft properties, e.g. aircraft forward velocity, density, reference chord and area, aircraft mass, wingspan and moments of inertia.

The equations used to relate the stability coefficients and stability derivatives are shown in tables 3.1 and 3.2.

<b>Longitudinal</b>			
<i>Derivative</i>	<i>Unit (SI)</i>	<i>Derivative</i>	<i>Unit (SI)</i>
$X_u = C_{X_u} \frac{Q S}{m U_0}$	$s^{-1}$	$Z_{\delta_s} = C_{Z_{\delta_s}} \frac{Q S}{m}$	$m/s^2$
$X_w = C_{X_w} \frac{Q S}{m U_0}$	$s^{-1}$	$M_u = C_{m_u} \frac{Q S \bar{c}}{U_0 I_{yy}}$	$(m.s)^{-1}$
$X_{\delta_s} = C_{X_{\delta_s}} \frac{Q S}{m}$	$m/s^2$	$M_w = C_{m_\alpha} \frac{Q S \bar{c}}{U_0 I_{yy}}$	$(m.s)^{-1}$
$Z_u = C_{Z_u} \frac{Q S}{m U_0}$	$s^{-1}$	$M_q = C_{m_q} \frac{\bar{c}}{2U_0} \frac{Q S \bar{c}}{I_{yy}}$	$s^{-1}$
$Z_w = C_{Z_w} \frac{Q S}{m U_0}$	$s^{-1}$	$M_{\dot{w}} = C_{m_\alpha} \frac{\bar{c}}{2(U_0)^2} \frac{Q S \bar{c}}{I_{yy}}$	$m^{-1}$
$Z_q = C_{Z_q} \frac{\bar{c}}{2U_0} \frac{Q S}{m}$	$m/s$	$M_{\delta_s} = C_{m_{\delta_s}} \frac{Q S \bar{c}}{I_{yy}}$	$s^{-2}$

Table 3.1 - Longitudinal stability derivatives

<b>Lateral</b>			
Derivative	Unit (SI)	Derivative	Unit (SI)
$Y_\beta = C_{Y_\beta} \frac{Q S}{m U_0}$	$s^{-1}$	$L_r = C_{l_r} \frac{b^2 Q S}{2U_0 I_{xx}}$	$s^{-1}$
$Y_p = C_{Y_p} \frac{b Q S}{2U_0 m}$	$m/s$	$L_{\delta_s} = C_{l_{\delta_s}} \frac{Q S b}{I_{xx}}$	$s^{-2}$
$Y_r = C_{Y_r} \frac{b Q S}{2U_0 m}$	$m/s$	$N_\beta = C_{n_\beta} \frac{Q S b}{I_{zz}}$	$s^{-2}$
$Y_{\delta_s} = C_{Y_{\delta_s}} \frac{Q S}{m}$	$m/s^2$	$N_p = C_{n_p} \frac{b^2 Q S}{2U_0 I_{zz}}$	$s^{-1}$
$L_\beta = C_{l_\beta} \frac{Q S b}{I_{xx}}$	$s^{-2}$	$N_r = C_{n_r} \frac{b^2 Q S}{2U_0 I_{zz}}$	$s^{-1}$
$L_p = C_{l_p} \frac{b^2 Q S}{2U_0 I_{xx}}$	$s^{-1}$	$N_{\delta_s} = C_{n_{\delta_s}} \frac{Q S b}{I_{zz}}$	$s^{-2}$

**Table 3.2 - Lateral stability derivatives**

In all relations,  $Q$  is the dynamic pressure given by the equation:

$$Q = \frac{1}{2} \rho U_0^2. \quad (3.2)$$

### 3.2 Stability coefficient estimation

From *AVL* it was possible to attain almost all stability coefficients with the exception of the  $C_{m_{\dot{\alpha}}}$ . The dot stability coefficients are not computed by the program, and since the only one important to aircraft motion is  $C_{m_{\dot{\alpha}}}$ , this is the only one to be estimated. The expression used to estimate  $C_{m_{\dot{\alpha}}}$  is shown in equation (3.3).

$$C_{m_{\dot{\alpha}}} = -2C_{L_{\alpha_h}} \eta_h \bar{V}_h (\bar{x}_{ac_h} - \bar{x}_{cg}) \frac{d\epsilon}{d\alpha}, \quad (3.3)$$

The equation (3.3) was used accordingly to reference [16], and further details or definitions are specified in Appendix G.

The term “ $h$ ” in equation (3.3) is related to the horizontal tail of the aircraft. Therefore to proceed with the stability coefficient estimation, the aft wing of SensorCraft was approximated to a horizontal tail. Since stability coefficient estimation formulas are mostly available for conventional aircraft, different configurations have to be adjusted to be used in such formulas. In conclusion there will be always an intrinsic error. The result obtained for the stability coefficient  $C_{m_{\dot{\alpha}}}$  is:  $C_{m_{\dot{\alpha}}} = -2,4$ .

The value of  $C_{m_{\dot{\alpha}}}$  obtained for SensorCraft, was compared with  $C_{m_{\dot{\alpha}}}$  values of conventional aircrafts in reference [16], and confirmed to be inside their range of variation which was  $[-9,1 ; -0,95]$ . Although it does not prove that the value estimated is exact, it proves that the value obtained is not absurd.

## 3.3 Drag contributions

### 3.3.1 Theory

There are various drag force contributions of different nature in a three-dimensional (3-D) wing. Some of these contributions appear due to 3-D properties, while others are simply explained by two-dimensional (2-D) theory.

The entire analysis is conducted for subsonic flight, the wave drag and interference drag effects will be neglected, because their contributions are small and difficult to calculate. The wave drag is the result of shock-waves so can be neglected for subsonic speeds. The interference drag effects are too complex, but small comparing with other drag contributions at subsonic speeds.

In short, the drag force contributions are:

- Induced drag
- Parasitic Drag
  - Pressure drag
  - Skin friction drag

Induced drag or lift-induced drag is purely three-dimensional effect. It occurs mainly on the wings, caused by the difference of air pressure between the top surface (lower pressure) and the bottom surface (higher pressure) of the wing. The swirling movement of the air around the wing creates vortices that will induce a downwash angle in the airflow. For a given increase in the downwash angle, so the angle of attack will increase, creating an additional drag component (induced drag).

The parasitic drag has two components: the pressure drag and the skin friction drag. Pressure drag results from the pressure distribution over the wing, so it depends on the form of the object that is facing the airflow. Skin friction drag depends on the friction (wall shear stress) between the airflow and the wing, and it is caused by viscous drag in the boundary layer.

### 3.3.2 Application of the different drag effects

Since *AVL* only accounts for the induced drag in the calculation of the stability coefficients of the control surfaces, it is necessary to calculate the parasitic drag using another method. This is important to explore the many control strategies based on drag force, like the *speed-brake control*.

It was decided to calculate the parasitic drag with a 2-D viscous flow simulator program. Since, the induced drag is a 3-D effect, a 2-D analysis allows to detach it from parasitic drag. The program chosen was the *XFOIL*.

Using *AVL* to determine the influence of control surfaces deflection in induced drag, is quite different than using *XFOIL*. While the *AVL* can determine the change in the induced drag coefficient ( $C_{D_i}$ ) of the entire aircraft for a deflection in the control surfaces, the *XFOIL* only computes the change in the parasitic drag coefficient ( $C_{D_p}$ ) of an airfoil.

Since *XFOIL* makes the calculations for an airfoil and *AVL* for a wing surface, the drag coefficients are adimensionalized by the different parameters.

<i>AVL</i>	<i>XFOIL</i>
$C_{D_i} = \frac{D_i}{\frac{1}{2}\rho U^2 S}$	$C_{D_p} = \frac{D_p}{\frac{1}{2}\rho U^2 \bar{c}}$

Table 3.3 – AVL and XFOIL drag coefficients

To solve this problem, the general equation of the total drag of the aircraft was used, as described in equation (3.4).

$$D = D_i + D_p, \quad (3.4)$$

where,  $D$  represents the total drag force,  $D_i$  is the induced drag force and  $D_p$  is the parasitic drag force.

Deriving the equation (3.4) in order to a control surface deflection  $\delta_s$ , (3.4) takes the form:

$$D_{\delta_s} = D_{i\delta_s} + D_{p\delta_s}. \quad (3.5)$$

Expanding the drag equation:

$$\frac{1}{2}\rho U_0^2 S C_{D_{\delta_s}} = \frac{1}{2}\rho U_0^2 S C_{D_{i\delta_s}} + \frac{1}{2}\rho U_{0n}^2 S C_{D_{p\delta_s}}, \quad (3.6)$$

where  $U_{0n}$  represents the normal velocity to the airfoil due to the wing swept. Finally, the stability coefficients are given by:

$$C_{D_{\delta_s}} = C_{D_{i\delta_s}} + \left(\frac{U_{0n}}{U_0}\right)^2 C_{D_{p\delta_s}}. \quad (3.7)$$

### 3.4 Determination of the Parasitic Drag using XFOIL

*XFOIL* is an interactive program for the design and analysis of subsonic isolated airfoils. This program uses a viscous analysis of airfoils, allowing for the calculation of transition and separation cases as well. Through this analysis it will be possible to determine the parasitic drag over an airfoil [17].

#### 3.4.1 Method

The methodology used to calculate the parasitic drag stability coefficient of a control surface due to its deflection, was to represent graphically the curve  $C_{D_p}$  vs  $\delta_s$ . For several deflection angles of the control surface, in an interval of  $[-30^\circ, 30^\circ]$ , the corresponding value of parasitic drag coefficient was calculated.

After the curve has been obtained, the stability coefficient of the parasitic drag versus the angle of deflection of control surface ( $C_{Dp\delta_s}$ ) is simply determined by the curve slope.

For each sector of the wing containing a specific control surface, the middle airfoil was chosen as representative section for that control surface. In this way, it was analyzed one airfoil for each control surface; assuming symmetry in the  $XZ$ -plane only 5 total airfoils were tested: the flaps, the inboard aileron, the outboard aileron, the outboard elevator and the inboard elevator. Since each airfoil had its own properties, such as chord, pitch angle, position of the control surface hinge or the perpendicular velocity in the airfoil (due to the swept wing characteristic), the analysis will be different from airfoil to airfoil.

The properties studied and introduced in the *XFOIL* program are presented in table 3.4.

<b>Properties</b>	<b>Formula</b>
$U_{0n}$	$U_{0n} = U_0 \cos \Lambda$
$Re$	$Re = \frac{U_0 \bar{c}}{\nu}$
$\theta_{total}$	$\theta_{total} = \theta_{aircraft} + \theta_{airfoil}$
$x_{hinge}$	(1)

Table 3.4 - Input airfoil properties for *XFOIL*

(1)The position of the control surface hinge  $x_{hinge}$ , is the ratio of the chord where the control hinge is located. For the forward wing controls  $x_{hinge} = 0.8$  and for the after wing  $x_{hinge} = 0.6$ .  $Re$  is the Reynolds number,  $\theta_{total}$  represents the total pitch angle of the section given by the sum of the airfoil pitch and aircraft pitch angle.  $\nu$  is the kinematic viscosity and is defined as  $\nu [m^2/s] = \frac{\mu}{\rho}$ , where  $\mu$  is the dynamic viscosity of air for the given air density in table 2.2. Other parameters were defined before, or can be seen in Appendix A and B.

The figure 3.3 exemplifies a typical result for  $C_{Dp}$  in *XFOIL* environment due to the positive deflection of control surface by 10 degrees.

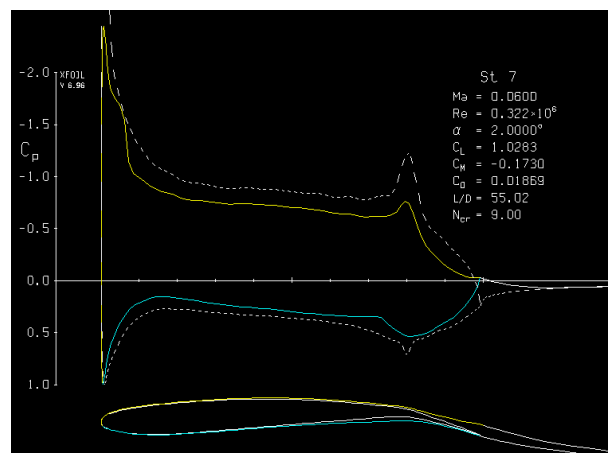


Figure 3.3 - *XFOIL* window results environment

### 3.4.2 XFOIL Results

The results from XFOIL will be presented next, to the different control surfaces.

#### ➤ Flaps

The variation of the flaps (C1 in figure 2.2) parasitic drag coefficient is given in figure 3.4. The stability coefficient  $C_{D\delta_f}$  is given by the curve slope, but since it has a parabolic shape, two different values of  $C_{D\delta_f}$  were calculated, the positive and negative values of deflection starting from the point of minimum drag coefficient (figure 3.5).

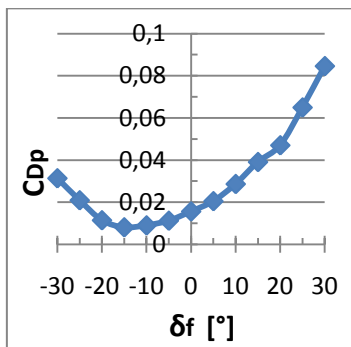


Figure 3.4 -  $C_{D_p}$  vs  $\delta_f$  curve

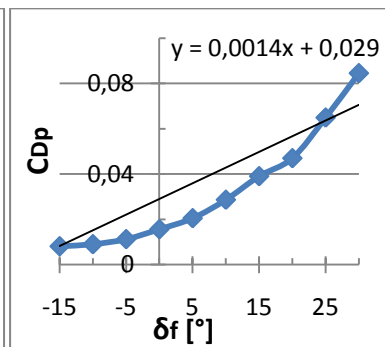
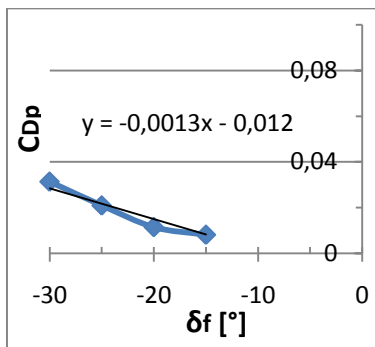


Figure 3.5 -  $C_{D_p}$  vs  $\delta_f$  curve slopes given by linear equations

#### ➤ Inboard Aileron

The variation of the inboard aileron (C2) parasitic drag coefficient is given in figure 3.6. To calculate  $C_{D\delta_{a_i}}$  the procedure was the same as for the flaps (figure 3.7).

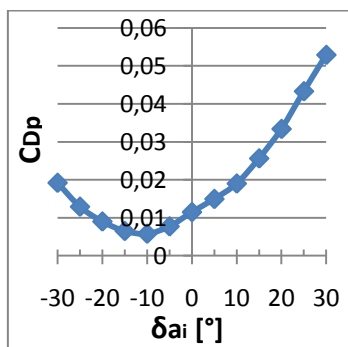


Figure 3.6 -  $C_{D_p}$  vs  $\delta_{a_i}$  curve

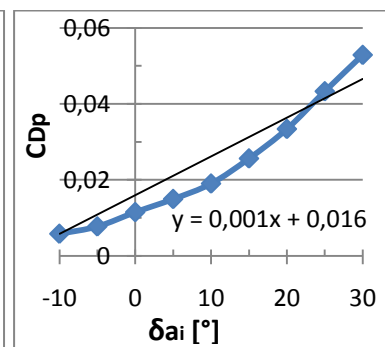
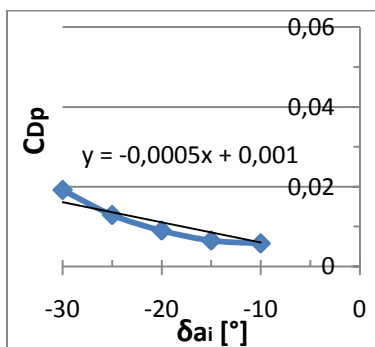


Figure 3.7 -  $C_{D_p}$  vs  $\delta_{a_i}$  curve slopes given by linear equations

➤ *Outboard Aileron*

The variation of the outboard aileron (C3) parasitic drag coefficient is given in figure 3.8. To calculate  $C_{D\delta_{a_o}}$  the procedure was the same as for the flaps (figure 3.9).

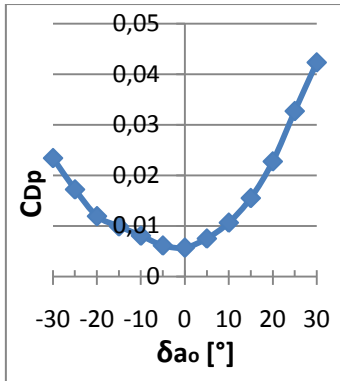


Figure 3.8 -  $C_{D_p}$  vs  $\delta_{a_o}$  curve

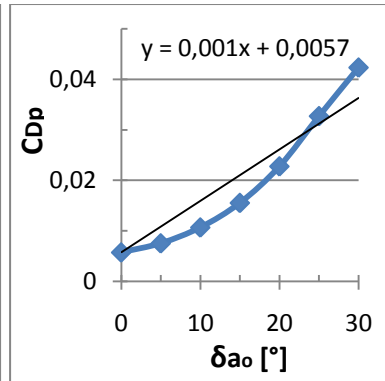
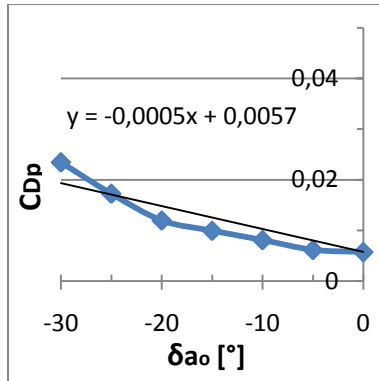


Figure 3.9 -  $C_{D_p}$  vs  $\delta_{a_o}$  curve slopes given by linear equations

➤ *Inboard Elevator*

The variation of the inboard elevator (C5) parasitic drag coefficient is given in figure 3.10. To calculate  $C_{D\delta_{e_i}}$ , the curve presents an interval of  $[-15^\circ, 10^\circ]$  where  $C_{D_p}$  practically has no variation, therefore only the curve slopes for deflections lower and higher than the given interval were taken into account. In conclusion, the coefficient is given by:

$$C_{D\delta_{e_i}} = 0 \quad \text{for} \quad \delta_{e_i} \in [-15^\circ, 10^\circ].$$

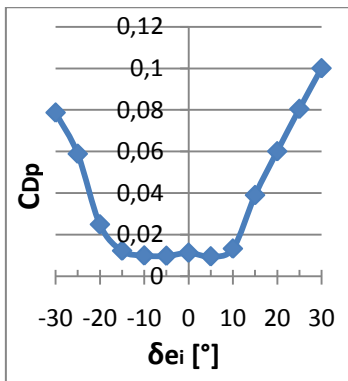


Figure 3.10 -  $C_{D_p}$  vs  $\delta_{e_i}$  curve

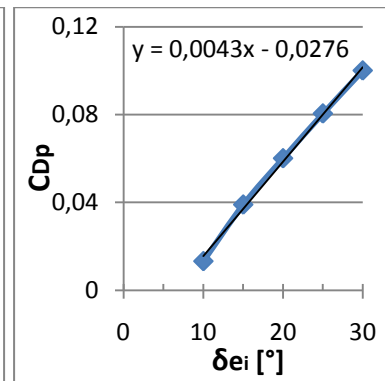
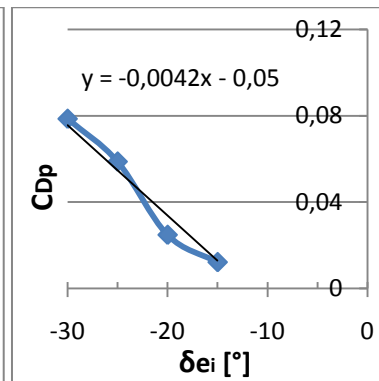


Figure 3.11 -  $C_{D_p}$  vs  $\delta_{e_i}$  curve slopes given by linear equations

➤ *Outboard Elevator*

The variation of the outboard elevator (C4) parasitic drag coefficient is given in figure 3.12. In the same manner than for the previous case, the coefficient was considered to be zero for the interval  $[-10^\circ, 5^\circ]$ . For the two remaining intervals two stability coefficients  $C_{D\delta_{e_o}}$  were obtained.

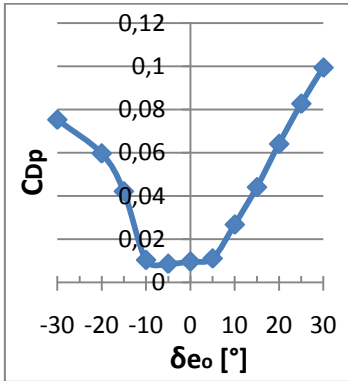


Figure 3.12 -  $C_{D_p}$  vs  $\delta_{e_o}$  curve

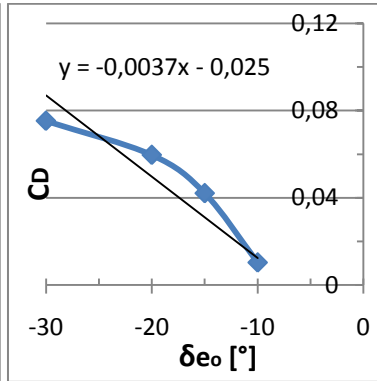
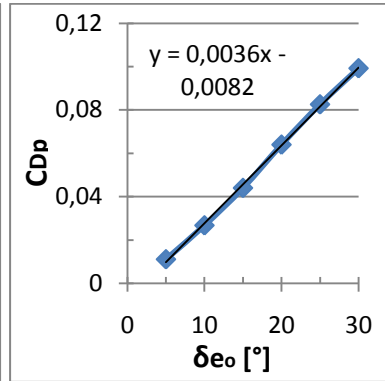


Figure 3.13 -  $C_{D_p}$  vs  $\delta_{e_o}$  curve slopes given by linear equations



## 3.5 Determination of the Induced Drag using AVL

### 3.5.1 AVL induced drag calculation

The changes in the induced drag coefficient ( $C_{D_i}$ ) due to the deflection of control surfaces were calculated by *AVL* in the same way as the parasitic drag coefficients ( $C_{D_p}$ ) were calculated with *XFOIL*. The values of  $C_{D_i}$  were obtained for each value of the control surface deflection in a range of  $[-30^\circ, 30^\circ]$ , thus obtaining the variation of  $C_{D_i}$  with the deflection of the control surface ( $\delta_s$ ), i.e.  $C_{D_i\delta_s}$ .

### 3.5.2 Results

The curve slopes will be taken for positive and negative deflections of the control surfaces, for the main reason of keeping further calculations simpler. This approximation can be justified by the much smaller range of variation of  $C_{D_i}$  [0,03; 0,04], when comparing to the range of  $C_{D_p}$  [0,01; 0,1], which is nine times higher. Furthermore, the parabola minimum was never at a higher distance than  $5^\circ$  from zero. Nevertheless, an error analysis will be taken at the end of this subsection.

➤ *Flaps*

The variation of the flaps (C1) induced drag coefficient is given in figure 3.14. Negative and positive values of  $C_{D_i\delta_f}$  are given by the curve slopes of linear equations in figure 3.15 (left and right, respectively).

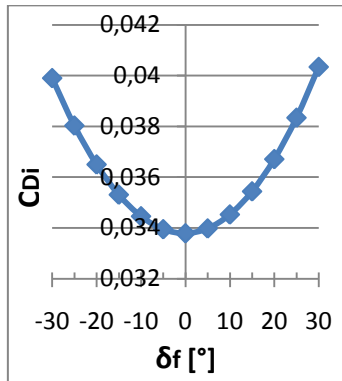


Figure 3.14 -  $C_{D_i}$  vs  $\delta_f$  curve

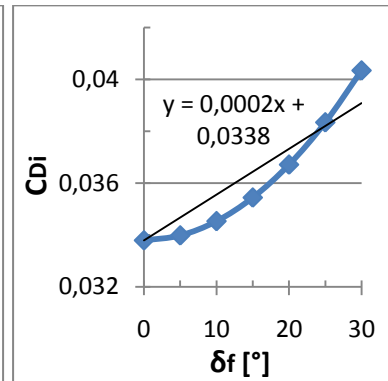
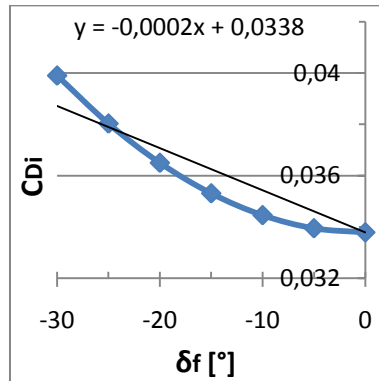


Figure 3.15 -  $C_{D_i}$  vs  $\delta_f$  curve slopes given by linear equations

➤ *Inboard Aileron*

The variation of the inboard aileron (C2) induced drag coefficient is given in figure 3.16. Negative and positive values of  $C_{D_i\delta_{a_i}}$  are given by the curve slopes of linear equations in figure 3.17 (left and right, respectively).

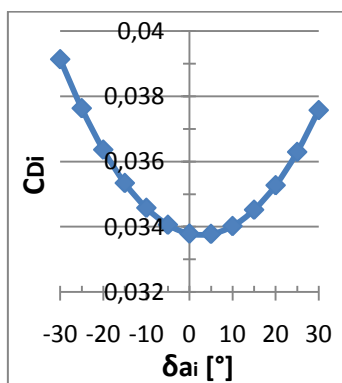


Figure 3.16 -  $C_{D_i}$  vs  $\delta_{a_i}$  curve

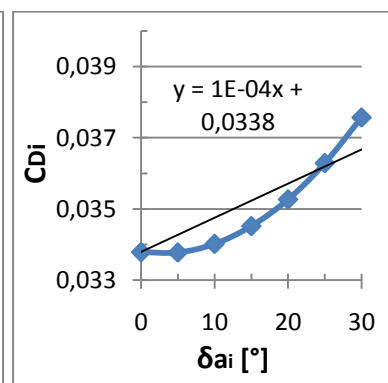
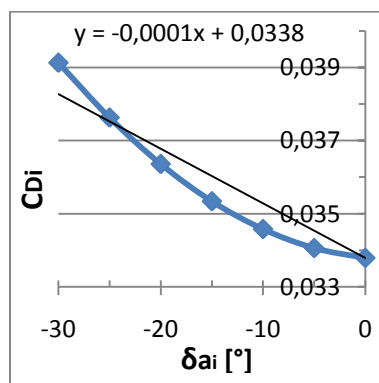


Figure 3.17 -  $C_{D_i}$  vs  $\delta_{a_i}$  curve slopes given by linear equations

➤ *Outboard Aileron*

The variation of the outboard aileron (C3) induced drag coefficient is given in figure 3.18. Negative and positive values of  $C_{D_i\delta_{a_0}}$  are given by the curve slopes of linear equations in figure 3.19 (left and right, respectively).

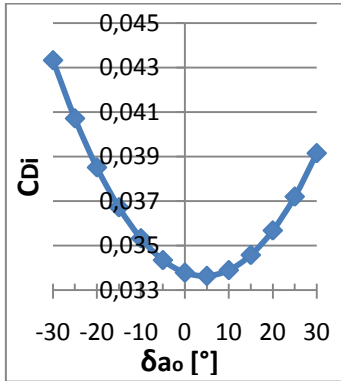


Figure 3.18 -  $C_{D_i}$  vs  $\delta_{a_0}$  curve

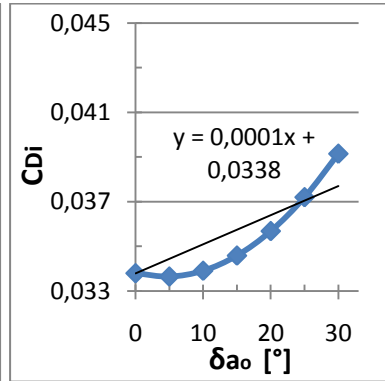
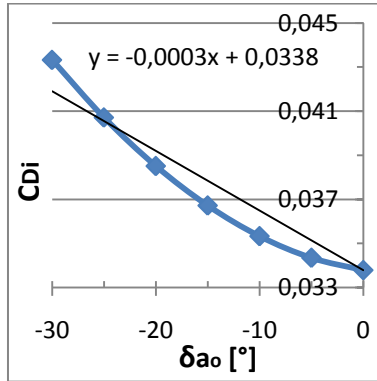


Figure 3.19 -  $C_{D_i}$  vs  $\delta_{a_0}$  curve slopes given by linear equations

➤ *Inboard Elevator*

The variation of the inboard elevator (C5) induced drag coefficient is given in figure 3.20. Negative and positive values of  $C_{D_i\delta_{e_i}}$  are given by the curve slopes of linear equations in figure 3.21 (left and right, respectively).

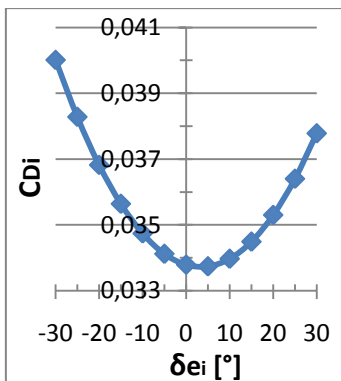


Figure 3.20 -  $C_{D_i}$  vs  $\delta_{e_i}$  curve

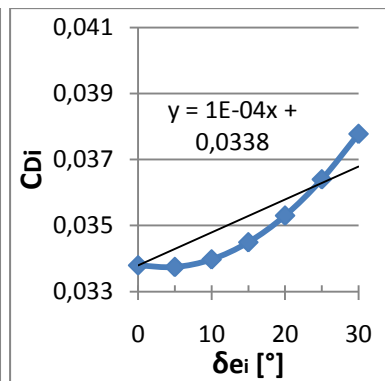
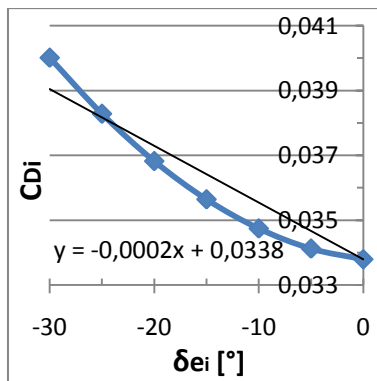


Figure 3.21 -  $C_{D_i}$  vs  $\delta_{e_i}$  curve slopes given by linear equations

➤ *Outboard Elevator*

The variation of the outboard elevator (C4) induced drag coefficient is given in figure 3.22. Negative and positive values of  $C_{D_i\delta_{e_o}}$  are given by the curve slopes of linear equations in figure 3.23 (left and right, respectively).

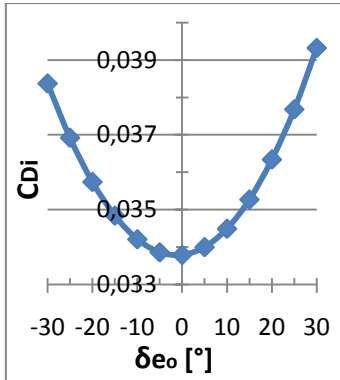


Figure 3.22 -  $C_{D_i}$  vs  $\delta_{e_o}$  curve

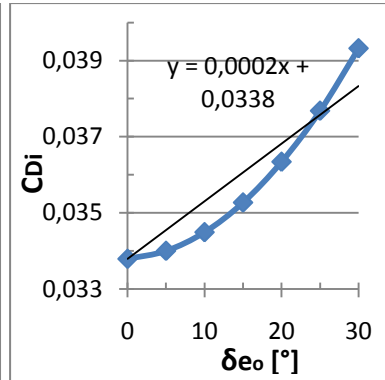
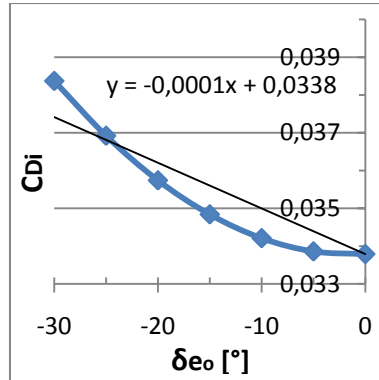


Figure 3.23 -  $C_{D_i}$  vs  $\delta_{e_o}$  curve slopes given by linear equations

The error of considering the curve slope starting from zero degrees, was conducted by comparing the divergence from the correct induced drag curve slope (taken at parabola minimum) with the parasitic drag curve slope presented before. The conclusion is the following:

- Inboard aileron has a maximum error of 2%
- Outboard aileron has a maximum error of 4,9%
- Inboard elevator has a maximum error of 1,2%
- All other control surfaces have maximum errors below 1%

For the sake of example, in the worst case (outboard aileron maximum deflection), the difference between the values of  $C_{D_i}$  for the correct curve slope (taken at parabola minimum) and for the used curve slope are  $1,5 \times 10^{-3}$ . Comparing with the value of  $C_{D_p}$  for the same deflection, which is  $30,6 \times 10^{-3}$ , the variation is very small.

Therefore, the errors admitted are small and the analysis can proceed with the approximation made for the curve slopes. Besides, the admitted curve slopes are upper bounded by the correct curve slope values, so the solutions will never exceed the real limits.

### 3.6 XFOIL and AVL result implications

The deflection of any control surface (CS) will result in a drag increase, i.e., in an increment of the  $X$ -axis force component. On the other hand, due to the wings dihedral and anhedral angles, the lift increment produced by the same control surface deflection will result in an additive contribution in the  $Y$  direction.

In figure 3.24 it is shown an example of the resolved components for a negative deflection of the right outboard elevator.

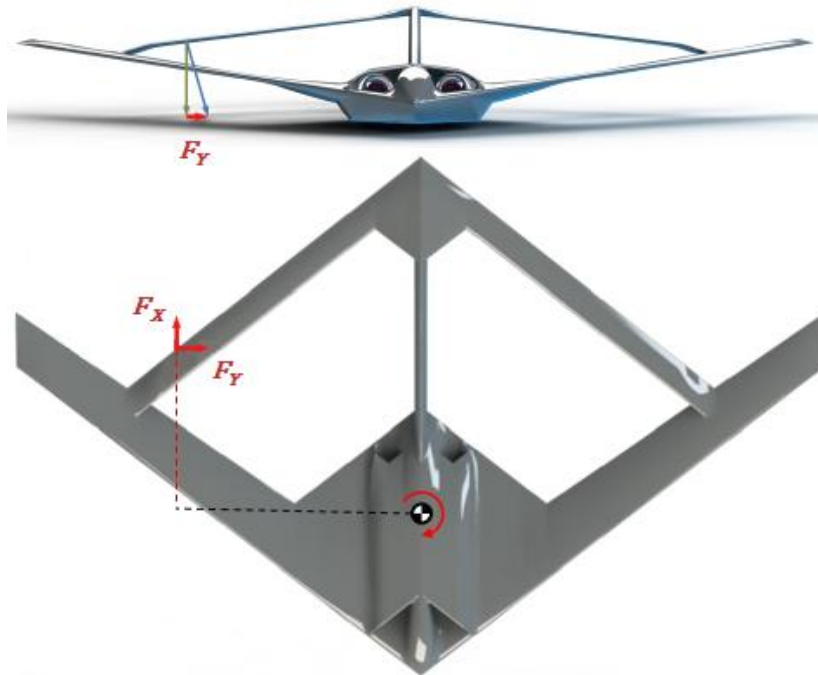


Figure 3.24 - Resolved force components for a CS deflection

For the yawing moment ( $N$ ) we have the following contribution of forces described in equation (3.8).

$$N = X \cdot l_y + Y \cdot l_x, \quad (3.8)$$

where,  $l_x$  and  $l_y$  represent the distance of the mean section of control surface to the  $Y$ -axis and  $X$ -axis of the stability system, respectively. Forces and moment in equation (3.8) are defined for:

$$N = \frac{1}{2} \rho U_0^2 S b C_n, \quad (3.9)$$

$$X = \frac{1}{2} \rho U_0^2 S b C_x, \quad (3.10)$$

$$Y = \frac{1}{2} \rho U_0^2 S b C_y. \quad (3.11)$$

Thus the equation (3.8) takes the form:

$$C_n = \frac{l_y}{b} C_X + \frac{l_x}{b} C_Y = -\frac{l_y}{b} C_D + \frac{l_x}{b} C_Y, \quad (3.12)$$

Lastly the variation of  $C_n$  with the control surface deflection ( $\delta_s$ ) is obtained by differentiating the equation (3.12) in order to  $\delta_s$ .

$$C_{n\delta_s} = -\frac{l_y}{b} C_{D\delta_s} + \frac{l_x}{b} C_{Y\delta_s}. \quad (3.13)$$

### 3.7 Yaw coefficient results

The parasitic and induced drag control coefficients obtained by the curve slopes of *XFOIL* and *AVL* graphics are summarized in the next table. The calculation of the total drag control coefficient was performed as in equation (3.7).

<b>Control Surface</b>	<b><math>C_{D_{p\delta_s}}</math> [1/°]</b>	<b><math>C_{D_{i\delta_s}}</math> [1/°]</b>	<b><math>C_{D_{\delta_s}}</math> [1/°]</b>
<i>Flap</i> < -15°	-0,0013	-0,0002	-0,0010
<i>Flap</i> > -15°	0,0014	0,0002	0,0011
<i>Inboard Aileron</i> < -10°	-0,0005	-0,0001	-0,0004
<i>Inboard Aileron</i> > -10°	0,001	0,0001	0,0007
<i>Outboard Aileron</i> < 0°	-0,0005	-0,0003	-0,0006
<i>Outboard Aileron</i> > 0°	0,001	0,0001	0,0007
<i>Inboard Elevator</i> < -15°	-0,0042	-0,0002	-0,0028
<i>Inboard Elevator</i> > 10°	0,0043	0,0001	0,0028
<i>Outboard Elevator</i> < -10°	-0,0036	-0,0001	-0,0023
<i>Outboard Elevator</i> > 5°	0,0036	0,0002	0,0024

**Table 3.5 - Drag coefficients of the control surfaces**

For all values not considered above, the given stability coefficients are assumed to be zero.

The yawing moment coefficient related to control surfaces will be given by the previous equation (3.13), and the results for each control surface are summarized in table 3.6.

<b><i>Control Surface</i></b>	<b><math>C_{n_{\delta_a}}</math> [1/°]</b>
<i>Flap</i> < -15°	-0,00021
<i>Flap</i> > -15°	0,00023
<i>Inboard Aileron</i> < -10°	-0,00008
<i>Inboard Aileron</i> > -10°	0,00028
<i>Outboard Aileron</i> < 0°	-0,00021
<i>Outboard Aileron</i> > 0°	0,00037
<i>Inboard Elevator</i> < -15°	-0,00051
<i>Inboard Elevator</i> > 10°	0,00017
<i>Outboard Elevator</i> < -10°	-0,00071
<i>Outboard Elevator</i> > 5°	0,00047

**Table 3.6 - Yaw moment coefficients of the control surfaces**

As expected, the yaw moment coefficients will strongly depend on the direction of the deflection, as can be verified in table 3.6.

The values of  $C_{n_{\delta_a}}$  in table 3.6 are for the right wing control surfaces; they will take symmetric values for the left wing.

## Chapter 4

# Aircraft Stability Analysis

Since all the stability coefficients of the SensorCraft are completely described, it is now possible to proceed with the stability study. Stability is a property of an equilibrium state, thus the meaning of the equilibrium has to be defined first. If an aircraft is to remain in steady uniform flight the resultant forces and the resultant moments in relation to the center of gravity must be zero. An aircraft satisfying this requirement is in a state of equilibrium. The state of equilibrium is called trimmed flight in flight dynamics. Stability is the property of an aircraft to preserve the trimmed flight condition and for a given perturbation of forces and moments it tends to restore the original condition. The stability of an aircraft is divided in the static and in the dynamic stability.

### 4.1 Static stability analysis

The static stability can be explained by a ball on a surface. Initially the ball is in equilibrium, and then experiences a disturbance from the equilibrium position caused by forces or moments (or both). The behavior of the ball after the disturbance can be evaluated into three different cases:

- statically stable
- statically unstable
- neutrally stable

where, statically stable means that the ball returned to the equilibrium position, statically unstable that the ball did not returned to equilibrium and neutrally stable that the ball will achieve an equilibrium state but different from the initial. In flight dynamics the statically stable and unstable cases are the most important and the neutrally stable case occurs rarely. The figure 4.1 represents the three cases of stability for the ball case.

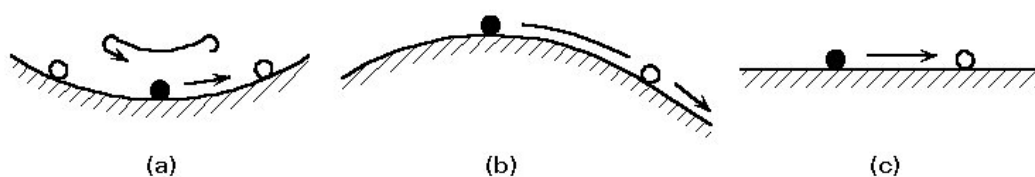


Figure 4.1 - (a) statically stable (b) statically unstable (c) neutrally stable [18]

### 4.1.1 Longitudinal motion

The static stability of the longitudinal motion is based on the analysis of the longitudinal properties of aircraft described below.

#### 4.1.1.1 Longitudinal static stability

The longitudinal static stability is referred to the aircraft's stability in the pitching plane,  $XZ$ -plane. If an aircraft is longitudinally stable a small increase in the angle of attack will cause a change of the pitching moment, which decreases the angle of attack. On the other hand, a small decrease in the angle of attack will cause in a change of the pitching moment, which increases the angle of attack.

As result, longitudinal static stability is evaluated by the sign of the stability derivative  $M_w$ ; an aircraft is statically stable when  $M_w$  is negative:  $M_w < 0$ .

#### 4.1.1.2 Forward speed stability

An aircraft is statically stable in its forward speed if the stability derivative  $X_u$  is negative:  $X_u < 0$ .

#### 4.1.1.3 Vertical speed stability

An aircraft is statically stable for any disturbance in the vertical speed if  $Z_w$  is negative:  $Z_w < 0$ .

### 4.1.2 Lateral motion

For the lateral motion the static stability is analyzed by the lateral properties of aircraft.

#### 4.1.2.1 Sideslip stability

The restoring force that usually opposes the sideslip motion, restoring the aircraft to the equilibrium condition, is measured by the sign of the stability derivative  $Y_\beta$ , and is statically stable when  $Y_\beta$  is negative:  $Y_\beta < 0$ .

#### 4.1.2.2 Static directional stability

If the aircraft has static directional stability, after a positive change in velocity  $v$  (or sideslip) the resulting perturbed yawing moment will tend to increase and the aircraft aligns itself with the relative airflow. This effect is quantified by the stability derivative  $N_\beta$ , and is statically directional stable if positive:  $N_\beta > 0$ .

The  $C_{N_\beta}$  is referred as 'static directional' or 'weathercock' stability coefficient.

#### 4.1.2.3 Lateral static stability

The lateral static stability is concerned with the aircraft ability to maintain wings level equilibrium in the roll sense. This effect is referred as 'dihedral effect' and for it to be stable the stability derivative  $L_\beta$  must be negative:  $L_\beta < 0$ .

### 4.1.3 Resume of the static stability of SensorCraft

Having described which aerodynamic properties contribute to the static stability of the aircraft, the analysis is presented in table 4.1. The stability derivatives were calculated as stated before in tables 3.1 and 3.2, using the stability coefficients of the SensorCraft given by *AVL* results in figure 3.3.

<i>Static Stability Requirement</i>	<i>Stability derivative</i>	<i>Static stability result</i>
$M_w < 0$	-0,48	<i>Stable</i>
$X_u < 0$	-0,02	<i>Stable</i>
$Z_w < 0$	-3,73	<i>Stable</i>
$Y_\beta < 0$	-0,17	<i>Stable</i>
$N_\beta > 0$	0,55	<i>Stable</i>
$L_\beta < 0$	-19,9	<i>Stable</i>

Table 4.1 - Static stability of the SensorCraft

From table 4.1 it was possible to conclude that the SensorCraft is statically stable for all the presented longitudinal and lateral requirements for static stability.

## 4.2 Dynamic stability analysis

The dynamic stability is concerned with the time history of the aircraft's motion after it is disturbed from the equilibrium point. An aircraft can be statically stable but dynamically unstable, therefore static stability does not guarantee dynamic stability.

The dynamic stability is the reduction of the disturbance in time, which indicates that there is a resistance to the motion, i.e., energy dissipation. In the flight dynamic the dissipation of energy is called positive damping. Otherwise if energy is added to the system, it is called negative damping and the equilibrium will never be achieved.

The positive damping is produced by forces and moments during the aircraft motion which work against the disturbances and tend to damp them in time.

When an aircraft has negative damping it is dynamically unstable: the aircraft cannot produce the forces and moments to damp the disturbances, and an artificial damping must be created using a control system. That will be treated further in Chapter 5.

### 4.2.1 Dynamic stability of longitudinal motion

The dynamic stability of longitudinal motion consists in two distinct oscillations: a short period oscillation called short period mode, and a long period oscillation called phugoid mode.

#### 4.2.1.1 Short period mode

The short period mode is referred as a very short period oscillation about the center of gravity. During the short period mode the velocity and the altitude of the aircraft do not change and the

oscillation is essentially in the angle of attack. The short period is a usually heavily damped oscillation so it is very fast.

A dynamic stable short period mode is presented in Appendix I, figure I.1.

#### 4.2.1.2 Phugoid mode

The phugoid mode is most commonly a lightly damped low frequency oscillation in speed  $u$  which couples into pitch attitude  $\theta$  and height  $h$ . Because of its low damping in this mode, it has a long period of oscillation. A significant feature of this mode is that the incidence angle of attack  $\alpha$  remains substantially constant during a disturbance.

The phugoid oscillation is a slow interchange of kinetic energy and potential energy about an equilibrium energy level as the aircraft attempts to re-establish the equilibrium level-flight condition from which it had been disturbed.

Since the aircraft tends to keep the angle of attack constant, the increase in velocity due to a disturbance results in a higher lift force which leads to an increase in the flight altitude. After the kinetic energy has been transformed into potential energy, the velocity decreases and so the lift leads the aircraft to the opposite situation where the aircraft flight altitude decreases. If the phugoid mode is stable it will slowly tend to the equilibrium condition as shown in figure I.2 of Appendix I.

#### 4.2.1.3 Longitudinal dynamic stability analysis

The dynamic stability of perturbed longitudinal motion is established from the knowledge of the eigenvalues of the state coefficient matrix  $A$  presented in equation (2.79). They can be found by solving the linear equation:

$$|\lambda I - A| = 0, \quad (4.1)$$

where,  $\lambda$  represents the eigenvalues, and  $I$  is a 4 x 4 identity matrix. By solving the determinant, the longitudinal stability is expressed as a fourth degree polynomial in  $\lambda$  shown in equation (4.2):

$$\lambda^4 + a_1\lambda^3 + a_2\lambda^2 + a_3\lambda + a_4 = 0. \quad (4.2)$$

The aircraft is called dynamically stable if all its eigenvalues  $\lambda_i$  of the coefficient matrix  $A$  for the lateral and longitudinal motions are real negative values or are complex numbers with a negative real part. In all other cases the aircraft will be dynamically unstable.

In flight dynamics it is usual that the quartic equation (4.2) factorizes into two quadratic factors corresponding to the short period and phugoid modes:

$$(\lambda^2 + 2\xi_{sp}\omega_{sp}\lambda + \omega_{sp}^2)(\lambda^2 + 2\xi_{ph}\omega_{ph}\lambda + \omega_{ph}^2) = 0. \quad (4.3)$$

The first factor contains the eigenvalues of the short period mode, where the  $\xi_{sp}$  represents the short period damping ratio and the  $\omega_{sp}$  represents the short period frequency. The second factor contains the eigenvalues of the phugoid mode, and  $\xi_{ph}$  and  $\omega_{ph}$  represent the phugoid damping ratio and frequency respectively.

## 4.2.2 Dynamic stability of lateral motion

The dynamic stability of lateral motion involves the coupling of rolling and yawing motions, which are discussed as lateral-directional modes.

The three lateral-directional modes are the spiral mode, the dutch roll mode and the roll mode.

### 4.2.2.1 Spiral mode

The spiral mode is a non-oscillatory, slowly convergent or divergent motion. When excited, the mode dynamics are usually slow to develop and involve complex coupled motion in roll, yaw and sideslip. It is described by changes in the bank angle  $\phi$  and the heading angle. The sideslip angle  $\beta$  is generally quite small, but cannot be neglected because the aerodynamic moments depend on it.

The spiral mode is usually excited by a disturbance in sideslip which typically follows a disturbance in roll causing a wing to drop. The figure I.3 in Appendix I represents the spiral mode development for a sideslip disturbance.

### 4.2.2.2 Dutch roll mode

The Dutch Roll is a lightly damped oscillatory motion having a low frequency. It is a classical oscillation in yaw, about the  $Z$ -axis of the aircraft, which couples into roll and sideslip. The motion described by the dutch roll mode is therefore a complex interaction between all three lateral-directional degrees of freedom.

In the figure I.4 of Appendix I is possible to see the evolution and coupling of dutch roll mode.

### 4.2.2.3 Roll mode

The roll mode is a non-oscillatory lateral characteristic. It follows immediately a lateral directional disturbance and it is a heavily damped mode, where the aircraft experiences a rolling motion predominantly about the  $X$  body axis.

Roll mode is usually substantially decoupled from the spiral and dutch roll modes. Other parameters like the sideslip angle  $\beta$ , heading angle  $\psi$ , and yawing rate  $r$  almost do not vary, and can be neglected in roll mode.

The roll mode is excited by a disturbing rolling moment in the aircraft which leads the wing to experience a component of velocity  $w'$  normal to it. This velocity will increase the incidence of the going-down wing (increasing lift) and decrease the incidence of the going-up wing (decreasing lift). This differential lift results in a restoring rolling moment as it can be seen in figure I.5 of Appendix I.

### 4.2.2.4 Lateral dynamic stability analysis

Similarly to the longitudinal motion, the dynamic stability of disturbed lateral motion can be determined by the characteristic polynomial that results from solving the equation (4.1).

The dynamic stability of perturbed lateral motion is established from the knowledge of the eigenvalues of the state coefficient matrix  $A$  presented in equation (2.80). They can be found by solving the linear equation (4.1), expressed as a fifth degree polynomial in  $\lambda$ , shown below:

$$\lambda^5 + d_1\lambda^4 + d_2\lambda^3 + d_3\lambda^2 + d_4\lambda + d_5 = 0. \quad (4.4)$$

Equation (4.4) is usually factorized into the following form:

$$\lambda(\lambda + e)(\lambda + f)(\lambda^2 + 2\xi_D\omega_D\lambda + \omega_D^2) = 0. \quad (4.5)$$

The simple term in  $\lambda$  corresponds to the heading state variable,  $\psi$ . The term  $(\lambda + e)$  corresponds to the spiral mode which is usually a slow motion or divergent. The term  $(\lambda + f)$  corresponds to the roll mode and the quadratic term corresponds to the dutch roll. Like in longitudinal modes,  $\xi_D$  represents the dutch roll damping ratio and  $\omega_D$  the dutch roll frequency.

### 4.2.3 Dynamic stability results

In order to achieve the results of the dynamic stability of lateral and longitudinal motions, the determinant in equation (4.1) was computed using *MATLAB*®.

The determinant was solved and the eigenvalues of all lateral and longitudinal modes were determined.

The results for longitudinal motion are detailed in figure 4.2 which is the representation of the eigenvalues in the Argand plane. In the table 4.2 the values of the eigenvalues are presented, as well as their association with the short period and phugoid modes.

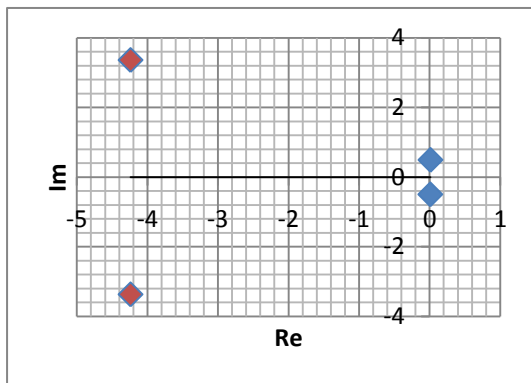


Figure 4.2 - Longitudinal eigenvalues in Argand plan

<b>Longitudinal</b>	
<i>Mode</i>	<i>Eigenvalues</i>
<i>Short Period</i>	$-4,24 \pm -3,37 i$
<i>Phugoid</i>	$0,011 \pm 0,5 i$

Table 4.2 - Longitudinal eigenvalues

The eigenvalues of the lateral motion are represented in Argand plan in figure 4.3. Their eigenvalues relation with the lateral modes, such as spiral, dutch roll and roll are described in table 4.3.

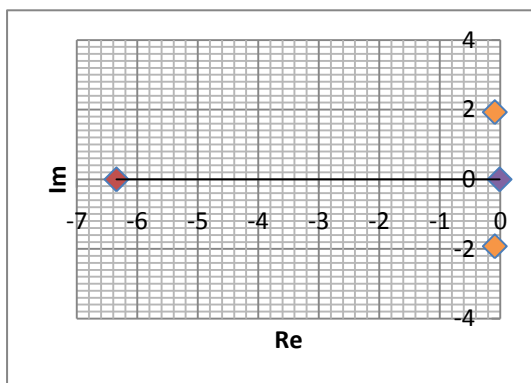


Figure 4.3 - Lateral eigenvalues in Argand plan

<b>Lateral</b>	
<i>Mode</i>	<i>Eigenvalues</i>
<i>Spiral</i>	$-0,01$
<i>Dutch Roll</i>	$-0,09 \pm 1,9 i$
<i>Roll</i>	$-6,3$

Table 4.3 - Lateral eigenvalues

### 4.3 Flying qualities evaluation

Aircraft flying qualities are usually characterized by several parameters which are related to the eigenvalues in complex plane of the different longitudinal and lateral modes. The most common parameters used are the damping ratio  $\xi$  and the natural frequency  $\omega_n$ .

For a given eigenvalue given by a real part  $\sigma$  and an imaginary part  $\omega$ , the natural frequency and the damping ratio are defined by equations (4.6) and (4.7) respectively:

$$\omega_n = \sqrt{\sigma^2 + \omega^2}, \quad (4.6)$$

$$\xi = -\frac{\sigma}{\omega_n}. \quad (4.7)$$

However the requirements of flight quality for these parameters differ on the class of aircraft and on the flight phase considered. Therefore it is essential to classify the aircraft and the flight phase. These classification parameters are presented in Appendix J (subsection J.1) according with reference [12].

#### 4.3.1 Aircraft flying qualities

The aircraft flying qualities are analyzed using several parameters, such as, natural frequency, damping ratio and time constants defined in Appendix J. For each mode, the flying qualities are determined comparing those parameters with the respective specification table,

The specification tables and parameters of longitudinal and lateral modes are given in Appendix J (subsections J.2 and J.3, for longitudinal and lateral modes respectively).

#### 4.3.2 Flying qualities analysis

According with the tables J.1 and J.2 (Appendix J) the SensorCraft is *class I* since it is a light aircraft, and the reconnaissance mission objectives for which precise control maneuverability is required, define the phase of flight as *phase A*.

The longitudinal parameters for the flight quality analysis are presented in table 4.4, and comparing with the specifications of each mode, the following results were obtained:

<b>Mode</b>	<b>Eigenvalue</b>	<b><math>\omega_n</math> [rad/s]</b>	<b><math>\xi</math></b>	<b>P [s]</b>	<b>Level</b>
<i>Short Period</i>	$-4,24 \pm 3,37i$	5,42	0,78	—	1
<i>Phugoid</i>	$0,011 \pm 0,5i$	0,5	-0,022	12,6	<i>Unstable</i>

Table 4.4 - Short period and phugoid flight quality results

Using the following relation of longitudinal modes frequencies and comparing with the equation (4.9):

$$\frac{\omega_{ph}}{\omega_{sp}} = 0,092.$$

In conclusion, the longitudinal modes have a good frequency separation. However, the overall flight quality of the longitudinal motion is the worst of the two modes quality. Therefore, since the phugoid mode is unstable, the whole longitudinal motion will be qualified as unstable. For the lateral motion, the analysis of the flight quality parameters of each mode is resumed in table 4.5 as well as the results for the quality levels.

<i>Mode</i>	<i>Eigenvalue</i>	$\omega_n$ [rad/s]	$\xi$	$\xi\omega_n$	<i>T</i> [s]	<i>Level</i>
<i>Spiral</i>	-0,01	0,01	1	-	-	1
<i>Dutch roll</i>	$-0,09 \pm 1,9i$	1,9	0,047	0,09	-	2
<i>Roll</i>	-6,3	6,3	1	-	0,16	1

Table 4.5 - Lateral modes flight quality results

Note that the spiral mode is *level 1* because its eigenvalue is negative.

As in the longitudinal motion, the overall quality of the lateral motion is defined by the worst level of all three lateral modes. Since the dutch roll mode has the worst flight quality level, the overall flight quality of the lateral motion is *level 2*.

In resume, the longitudinal motion is unstable because of the phugoid mode, since the separation of modes is respected and the short period mode is *level 1*. A controller to the phugoid mode will be explored in Chapter 5.

The lateral motion was determined as *level 2* by the flying quality of the dutch roll mode. This is unusual for common aircrafts where the spiral mode tends to be unstable and of worst quality than the dutch roll. However, this unusual but expected characteristic is related to the SensorCraft non-existence of a vertical stabilizer, which plays a huge role in dutch roll mode. Again, a controller should be designed to stabilize the lateral motion of the SensorCraft.

## 4.4 Configuration analysis of different control surface deflections

### 4.4.1 Longitudinal motion

The results of unstable flying qualities for the longitudinal motion are due to the unstable phugoid, since short-period is *level 1*. The speed of the aircraft has a major contribution for the position of phugoid eigenvalues, where slow velocities can make this mode unstable.

The augmentation of the longitudinal stability is usually made by means of a feedback system of the elevator. This will be explored in Chapter 5.

#### 4.4.2 Lateral motion

Based on the dynamic stability analysis of SensorCraft, the lateral motion stability is reduced due to the lack of a vertical stabilizer and consequent rudder to further control the motion. This became obvious when the dutch roll mode showed up to have the worst flying quality of all three lateral modes.

To proceed with the augmentation of the stability, we need to understand which control surfaces can provide the most effect on yawing moment coefficient,  $C_{n\delta_s}$ , but also on the aircraft side force,  $C_{Y\delta_s}$ . In order to build the stability augmentation system for the dutch roll, the rudder is usually the main control surface which is more effective upon this mode, thus on the dutch roll damping ratio and frequency, allowing for better lateral flying qualities. For the given aircraft control surfaces, the strategies to design a rudder equivalent control surface were presented before in Chapter 2: the mixed-control and the speed-brake control.

Before we present the configuration strategies of an equivalent rudder control surface, we need to understand why doing this and why not use all the control surfaces at once in the state space equations and compute the results.

The answer lies on the effectiveness desirable for the aircraft. On conventional aircrafts, ailerons and rudder are distinct control surfaces, so they have major effects either on roll or on yaw respectively. In our case, the many control surfaces of SensorCraft represent a great challenge because there is not a clear separate action in roll or in yaw motions. The control surfaces take action in both motions, having couple effects.

Therefore, there are many possible combinations of the control surfaces in order to achieve a required state. Most of the solutions will be undesirable, since they are the result of achieving a certain pilot request using all available control surfaces, not concerning with which ones are being used and how much they deflecting.

As an example of undesirable solutions, two different cases will be introduced.

The first undesirable case can occur when in order to attain a certain lateral state (e.g. sideslip velocity or yawing moment) two control surfaces could be deflected in a ratio of  $-2:1$ , where the control surface A has a deflection of 2 times the deflection angle of control surface B and in the opposite direction. It is then possible to have solutions between minimum deflection angles or exceeding angles that over use the control surfaces.

The second undesirable case happens due to the freely combination of control surfaces, when in order to achieve a requested motion any control surface can be used. If somehow the surface used for that motion is not much effective, the deflecting angle solutions can be absurd or lead to an exceeding use of a control surface, disabling it to act in the motions where it is more effective.

Consequently, it is necessary to determine which control surfaces most influence the yaw motion.

From table 3.6 the surfaces that most contribute to the changes of the aircraft yawing moment are the outboard and inboard elevators in aft wing (C4 and C5 in figure 2.2). However, deflecting only these surfaces will create an undesired rolling moment if deflected in opposite directions in both wings (for example right elevators going down and left elevators going up). If deflected in the same direction, the yawing moment becomes null and they work as elevators, acting only in pitching moment.

To explain the origin of the forces in the elevators and how the yawing moment is influenced by the direction of the deflections in right and left wings the figure 4.4 is presented. For convention, the signal (+) under a control surface mean that it is deflected downwards and the signal (-) that it is deflected upwards.

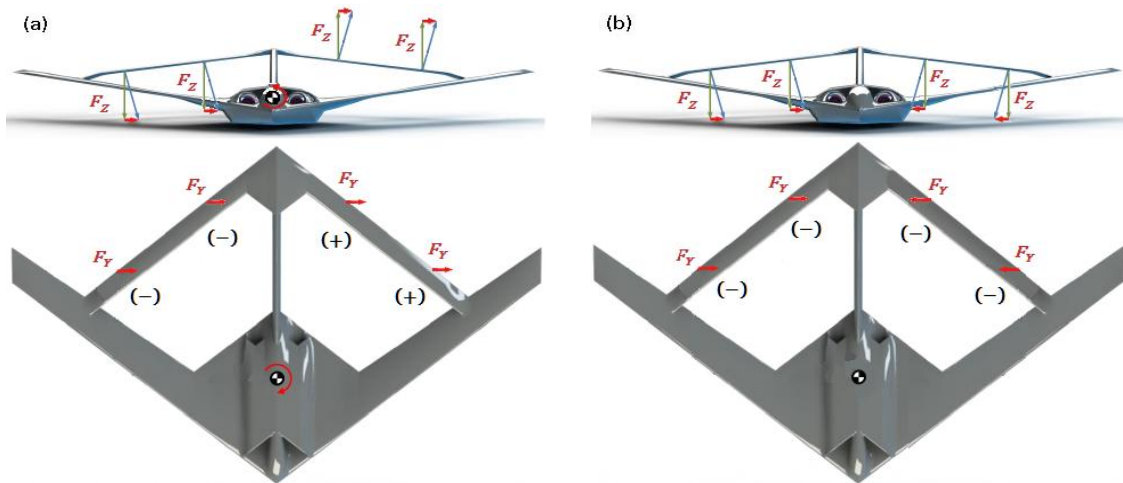


Figure 4.4 - Front and top views of forces produced by elevators deflected in (a) opposite and (b) same directions

From figure 4.4 the situation (a) arises when the right elevators are deflected up and the left elevators deflected down. In the right elevators, a deflection upwards, produce a downward force normal to the control surface, which due to the wing anhedral has a  $F_Y$  component pointing to the outer left wing. In the left wing the elevators deflected down produce an upward force normal to the control surface which due to anhedral will have also a  $F_Y$  component pointing to the outer left wing. As we can see in situation (a) the  $F_Y$  components of the force produce a yawing moment about the center of gravity and the  $F_Z$  components produce a rolling moment about the center of gravity.

From situation (b) both left and right elevators are deflected up. Therefore, the  $F_Y$  components from both wings cancel each other and no yawing moment is produced. As a result, the  $F_Z$  components will generate a pitching moment about the center of gravity.

It is clear from figure 4.4 (a), that the single use of elevators will produce undesirable rolling motion beside the wanted yaw moment. It is necessary to combine the use of elevators in

situation (a) with the control surfaces in front wing, in order to cancel the rolling moment and not the yawing moment. This situation is exemplified in figure 4.5.

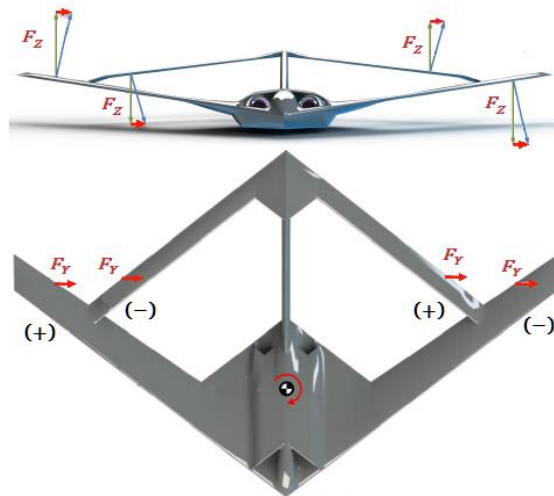


Figure 4.5 - Front and top views of forces and moments produced by the outboards elevator and aileron

In figure 4.5 the right and left outboard elevators (C4) are deflected up and down respectively, and the forces act as explained in figure 4.4 (a). The right and left outboard ailerons (C3) are deflected down and up respectively. The right aileron deflected down produce an upward force normal to the control surface producing (due to the dihedral of the front wing) a  $F_Y$  component as shown in figure 4.5. The left aileron deflected up produces a downward force which the component  $F_Y$  points also to the outside of the left wing.

Thus, the ailerons and elevators working in opposite directions cancel the rolling moment, and due to the opposite properties of the dihedral and anhedral of front and aft wings, all the  $F_Y$  components have the same direction and contribute for the same yawing moment.

These results of the dihedral and anhedral in yawing and rolling moments are also possible to be accomplished by analyzing the signs of the stability coefficients. For example, the right outboard aileron and the right outboard elevator have the following lateral and vertical forces stability coefficients (from the AVL results in figure 3.3).

<b>Control surface</b>	<b><math>C_{Y\delta_s}</math> [1/degree]</b>	<b><math>C_{Z\delta_s}</math> [1/degree]</b>
Right outboard aileron	-0,000346	-0,005307
Right outboard elevator	0,000656	-0,005592

Table 4.6 - Stability coefficients of right outboard aileron and elevator

As we can see in table 4.6, if the right outboard aileron and elevator (C3 and C4) deflect in opposite directions, the coefficients  $C_{Z\delta_s}$  having the same sign will tend to cancel each other and the coefficients  $C_{Y\delta_s}$  having different signs will sum their values of lateral force. As it was demonstrated in figure 4.5, the canceling of vertical forces will cancel the rolling moment and the lateral forces will act on the yawing moment of the SensorCraft.

#### 4.4.2.1 Mixed-control

Based on the achieved understanding of the control surfaces presented before, several configurations were designed to be tested and to determine which one is the most capable to control the yaw motion, and to act like a rudder.

For the mixed-control configurations presented next, and as shown in figure 4.5, the drag can be neglected since it has a very small contribution on the yawing moment. That is because both left and right control surfaces are being deflected and producing similar drag forces. This is easily confirmed by the drag stability coefficient of the control surface,  $C_{D\delta_s}$ , when it has a negative deflection one side of the wing and a positive deflection on the other side of the wing. From table 3.5 it is possible to verify that positive and negative deflections of the control surfaces have similar results for the  $C_{D\delta_s}$ , where the error admitted is less than 8.3% for all control surfaces, with the exception of the inboard aileron (C2), with an error of 29.7% but, where the drag force is small comparing with other control surfaces.

Therefore, according with equation (3.13) the  $C_{x\delta_s}$  becomes null and the new yawing stability coefficients of control surfaces are calculated. The drag-less coefficients  $C_{n\delta_s}$  are presented in table 4.7 only for the right wing control surfaces, since left wing ones have symmetric values.

<b>Control Surface</b>	<b><math>C_{n\delta_s}</math> [1/°]</b>
<i>Flap</i>	0,000003
<i>Inboard Aileron</i>	0,000053
<i>Outboard Aileron</i>	0,000056
<i>Inboard Elevator</i>	-0,000168
<i>Outboard Elevator</i>	-0,000134

**Table 4.7 - Drag-less yawing coefficient  $C_{n\delta_s}$  of control surfaces**

The configurations of mixed-control will follow the same analogy of figures 4.4 and 4.5 and therefore, there was no need to present the front view of the SensorCraft. To easily spot which surfaces are being deflected up and down, the figures follow the convention defined before and the incremental force component  $F_Y$  produced by the control surface deflection, is represented through a red vector.

The mixed-control configurations are the following:

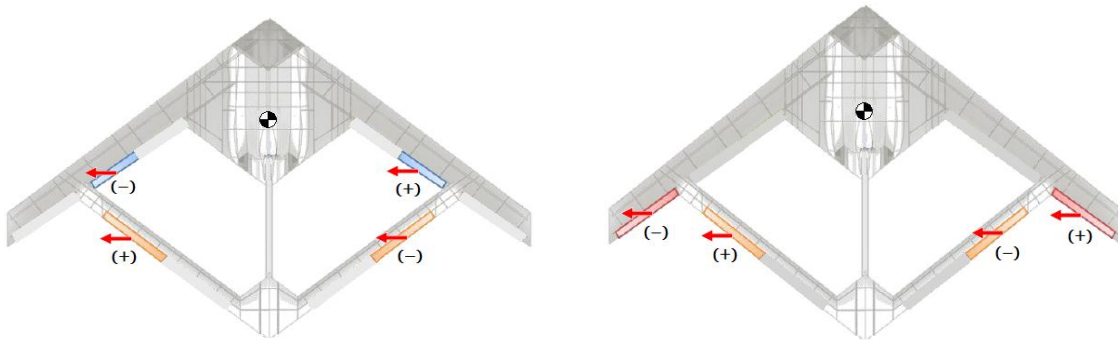


Figure 4.6 - Mixed-control configuration 1 and 2 (left and right respectively)

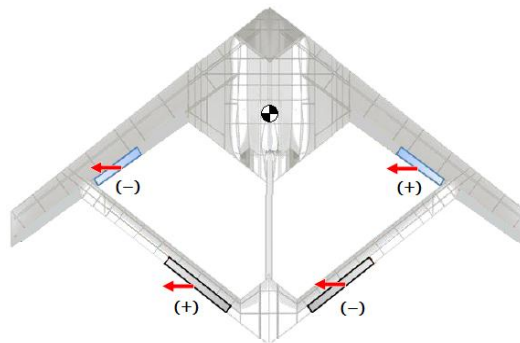


Figure 4.7 - Mixed-control configuration 3

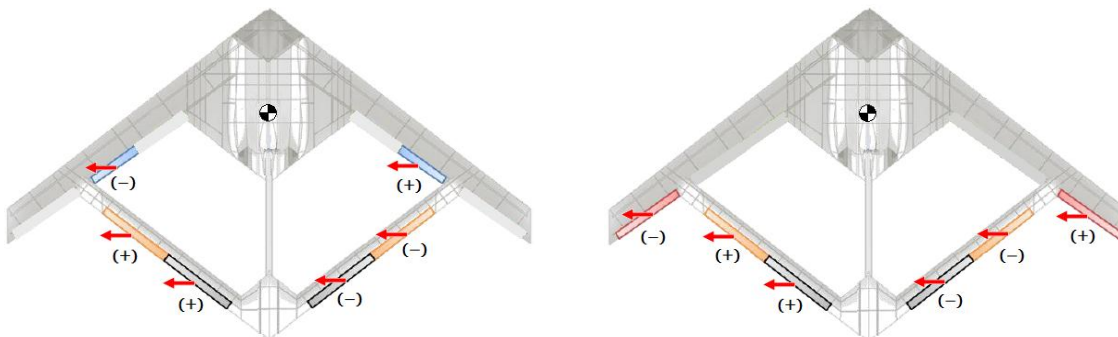


Figure 4.8 - Mixed-control configuration 4 and 5 (left and right respectively)

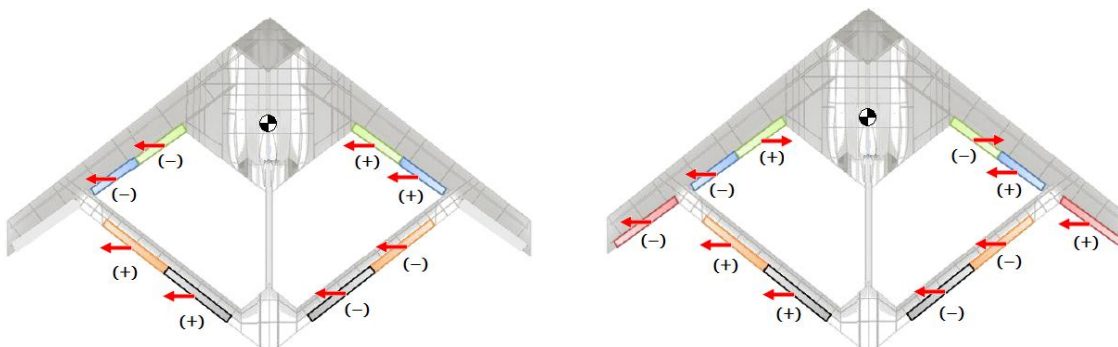


Figure 4.9 - Mixed-control configuration 6 and 7 (left and right respectively)

All the configurations above were not just based in what was explained in subsection 4.4.2. They are also the result of an iterative investigation; therefore the results obtained for a previous configuration were sometimes the key for the following configuration designed. For example, after analyzing the configuration 6 (figure 4.9), the rolling moment was cancelled for the entire use of control surfaces. It can be seen that the addition of the outboard ailerons in configuration 7 could not be used, since they would create a rolling moment. Therefore, it was chosen to deflect the flaps (C1) in the same direction of elevators (C4 and C5) so that both contribute for the same rolling moment, allowing the outboard aileron to be used and cancel it.

Note that the presented configurations are designed for a positive yawing moment about the Z-axis, while for a negative yawing moment the control surfaces must simply assume symmetric deflections of each case.

#### 4.4.2.2 Speed-brake control

Speed-brake control is used by deflecting a split flap on one side of the wing, as was explained before. The analogy of speed-brake control to SensorCraft is made by using a control surface in the front wing deflecting one direction and another in the aft wing deflecting in opposite direction (but only in left or right side of aircraft). It is like a split flap but its upper and lower flaps are positioned in different wings (front and aft wings).

Figure 4.10 represents a conventional split flap, and an equivalent split flap used by mixing the deflections of control surfaces in front and aft wings.

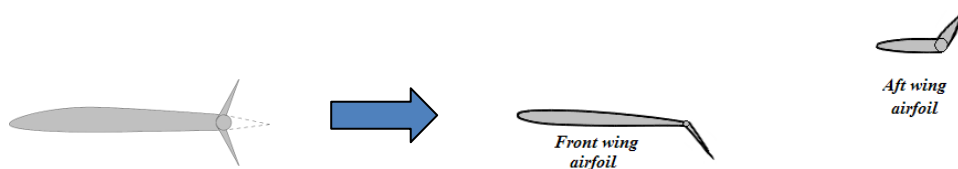


**Figure 4.10 - Analogy between conventional split flaps and SensorCraft split flaps**

From figure 4.10 it seems we can freely choose the direction of the deflection of control surfaces in SensorCraft. For example deflecting down in front wing and up in aft wing, or choosing the respective symmetric deflections in each wing. However, analyzing the yaw moments we can see that it is not true: front wing control surfaces going down and aft wing going up has a higher efficiency in the yawing moment than the symmetric case, as we can prove in figure 4.11.

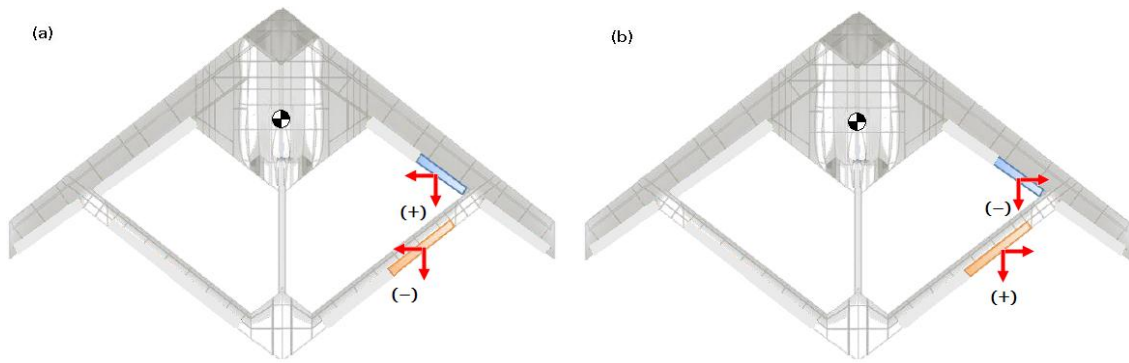


Figure 4.11 -  $F_x$  and  $F_y$  components for (a) front wing down deflection and aft wing up deflection and (b) front wing up deflection and aft wing down deflection

In case (b) the  $F_x$  and  $F_y$  components do not contribute for the same moment, canceling the yawing moments of each other, while in case (a) the forces contribute for the same yawing moment. For that reason the only configurations presented for speed-brake control are referred to case (a).

The speed-brake control configurations analyzed are represented in the next figures and they follow the same format of the previous configurations. The only difference is the red vector in X-axis direction representing the drag force contribution of the control surface,  $F_x$ .

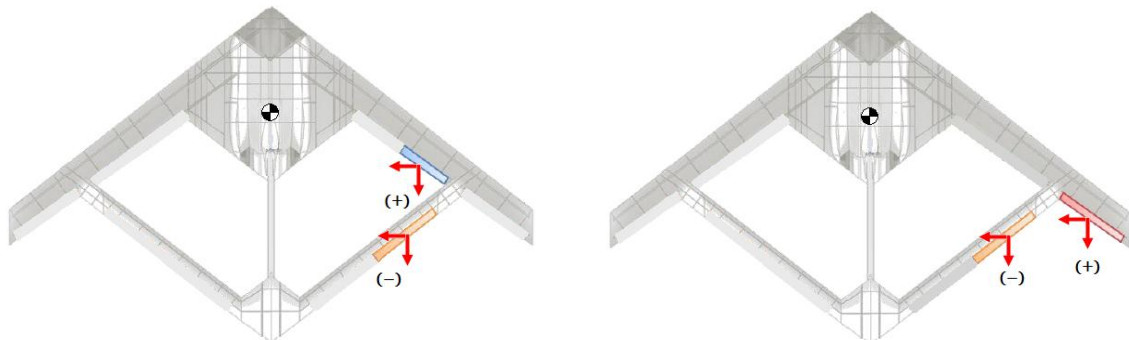


Figure 4.12 - Speed-brake control configuration 1 and 2 (left and right respectively)

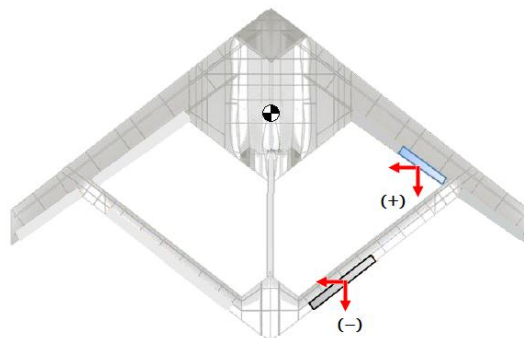


Figure 4.13 - Speed-brake control configuration 3

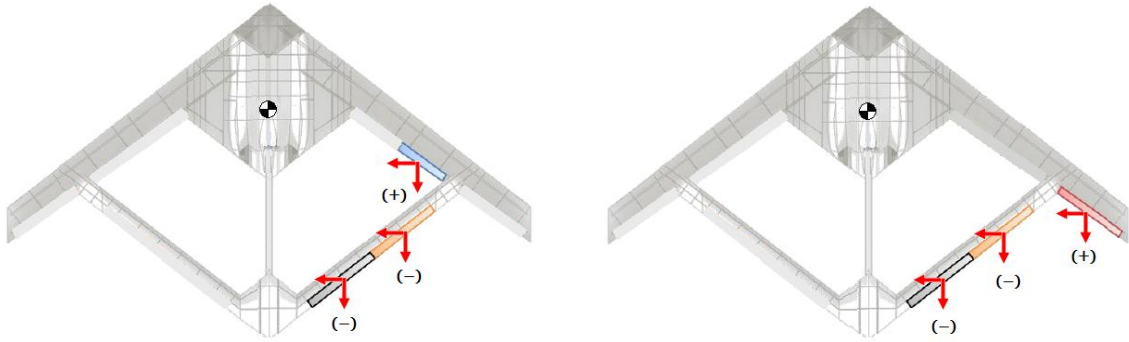


Figure 4.14 - Speed-brake control configuration 4 and 5 (left and right respectively)

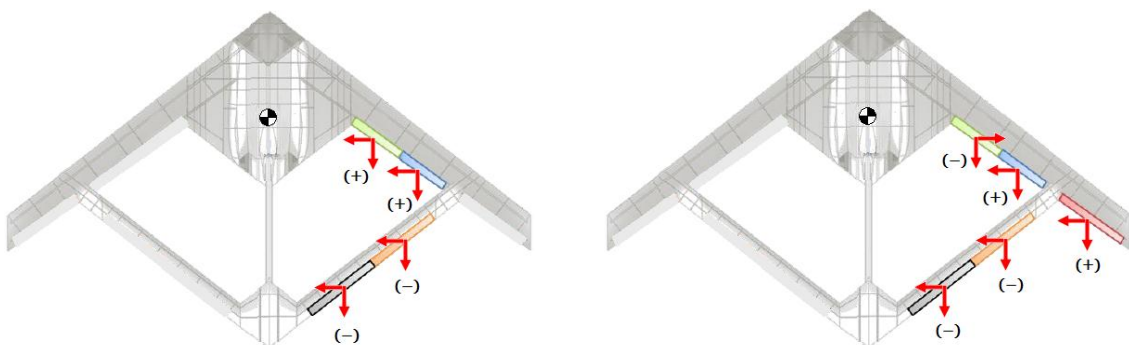


Figure 4.15 - Speed-brake control configuration 6 and 7 (left and right respectively)

The speed-brake control configurations are also represented for a positive yawing moment about the Z-axis. In order to achieve a negative yawing moment the deflections of the control surfaces are the same but in the left wing.

In the next Chapter the configurations mentioned previously will be tested with time-space analysis, and the control system will be designed for each configuration.

## Chapter 5

# Control System Methods

In Chapter 4, the flying properties and qualities of the SensorCraft were established, and different techniques to improve its motion qualities were discussed.

In the present Chapter a control system will be developed based on the existent control surfaces of each control technique configuration.

### 5.1 Equivalent control surface transformation

The use of a large number of control surfaces can lead to several solutions, not all of them feasible. Therefore, the degrees of freedom can be reduced by establishing physic relations between the control surfaces, such as angles and direction of deflections. By combining the existent control surfaces, it allows the transformation into equivalent conventional control surfaces and the system becomes simpler.

#### 5.1.1 Elevator

For example, the longitudinal motion makes use of the right and left inboard elevators (C5) to work as an elevator. Their action in the longitudinal pitching moment is maximized when an equal deflection of both right and left elevators take place and in the same direction. In this way the lateral coefficients ( $C_{Y\delta_s}$ ,  $C_{l\delta_s}$ ,  $C_{n\delta_s}$ ) of, the right and left elevators are minimized or cancelled if they have symmetric values.

In short, for the left and right inboard elevators the following relation is used:

$$\delta_{e_{left}} = \delta_{e_{right}} = \delta_e . \quad (5.1)$$

The effect of this definition in longitudinal forces and moment coefficients is given below:

$$C_X = C_{X\delta_{e_{right}}} \delta_{e_{right}} + C_{X\delta_{e_{left}}} \delta_{e_{left}} = (C_{X\delta_{e_{right}}} + C_{X\delta_{e_{left}}}) \delta_e , \quad (5.1)$$

$$C_Z = C_{Z\delta_{e_{right}}} \delta_{e_{right}} + C_{Z\delta_{e_{left}}} \delta_{e_{left}} = (C_{Z\delta_{e_{right}}} + C_{Z\delta_{e_{left}}}) \delta_e , \quad (5.2)$$

$$C_m = C_{m\delta_{e_{right}}} \delta_{e_{right}} + C_{m\delta_{e_{left}}} \delta_{e_{left}} = (C_{m\delta_{e_{right}}} + C_{m\delta_{e_{left}}}) \delta_e . \quad (5.3)$$

Analyzing both left and right control surfaces stability coefficients (figure 3.3), it can be verified equal contributions for:

$$C_{X\delta e_{right}} = C_{X\delta e_{left}} = C_{X\delta e} , \quad (5.4)$$

$$C_{Z\delta e_{right}} = C_{Z\delta e_{left}} = C_{Z\delta e} , \quad (5.5)$$

$$C_{m\delta e_{right}} = C_{m\delta e_{left}} = C_{m\delta e} , \quad (5.6)$$

resulting in the following forces and moment:

$$C_X = 2 C_{X\delta e} \delta_e , \quad (5.7)$$

$$C_Z = 2 C_{Z\delta e} \delta_e , \quad (5.8)$$

$$C_m = 2 C_{m\delta e} \delta_e . \quad (5.9)$$

Since  $C_{Y\delta s}$ ,  $C_{l\delta s}$ ,  $C_{n\delta s}$  have symmetric values for the left and right elevators, for an equal deflection, their contribution to lateral force and moments becomes null.

Through these linear transformations the left and right inboard elevators (C5) were combined into an equivalent conventional elevator that takes only action in the longitudinal motion. The longitudinal stability coefficients of the equivalent control surface  $\delta_e$  are given by 2 times the stability coefficients of either right or left inboard elevators.

These linear transformations are conducted assuming a interval of  $[-30^\circ, 30^\circ]$  for the deflection of control surfaces, where the control stability coefficients vary linearly.

### 5.1.2 Aileron

In the case of the lateral motion, the ailerons control the rolling moment. This moment is maximized if the left and right outboard ailerons (C3) are deflected symmetrically. Thus, a symmetric deflection not only assure a maximum rolling moment, but also that no exceeding values of deflection of control surface are achieved, since both left and right reach their limit of deflection ( $30^\circ$ ) at the same time.

The relation between the left and right outboard is given by:

$$\delta_{a_{left}} = -\delta_{a_{right}} = \delta_a , \quad (5.10)$$

following the same analysis as the one for the elevators, and considering that for left and right ailerons the lateral stability coefficients have symmetric values and the longitudinal stability coefficients have equal values. Consequently, the longitudinal contributions for forces and moments become null, and the lateral doubles their effects:

$$C_Y = 2 C_{Y\delta a} \delta_a , \quad (5.11)$$

$$C_l = 2 C_{l\delta a} \delta_a , \quad (5.12)$$

$$C_n = 2 C_{n\delta a} \delta_a , \quad (5.13)$$

where:

$$2 C_{Y\delta_a} = C_{Y\delta_a \text{ left}} - C_{Y\delta_a \text{ right}} , \quad (5.14)$$

$$2 C_{l\delta_a} = C_{l\delta_a \text{ left}} - C_{l\delta_a \text{ right}} , \quad (5.15)$$

$$2 C_{n\delta_a} = C_{n\delta_a \text{ left}} - C_{n\delta_a \text{ right}} . \quad (5.16)$$

In conclusion,  $\delta_a$  is the aileron equivalent control surface of the right and left ailerons (C3), corresponding in the real model to the symmetric deflection of both right and left control surfaces.

From this point forward, the following definitions will take place:

- If two opposing control surfaces in right and left wings are working as elevators they will be addressed as  $\delta_e$  . It will be considered that they deflect the same value and in same direction, along with the considerations stated above for the elevators.
- On the other hand, if two opposing control surfaces on the right and left wings work as ailerons they will be addressed as  $\delta_a$  . It will be considered that these control surfaces deflect symmetrically and with the considerations stated above for the ailerons.

### 5.1.3 Rudder

Based on the yaw control methods and configurations presented before (figures 4.11 – 4.20), the simplification of the degrees of freedom for the lateral system will follow the same steps as for the elevators and ailerons. The rudder equivalent control surface will be created by maximizing the yaw moment and minimizing the rolling moment.

Once again assuming linearity of the control stability coefficients in the interval  $[-30^\circ, 30^\circ]$ , for each configuration of mixed-control and speed-brake control, the relations that transform the real control surfaces into an equivalent rudder control surface were established.

#### 5.1.3.1 Mixed-control

For the mixed-control method, the analysis was computed following the next steps for each configuration, where the objective is to determine the relations between the deflections of the control surfaces which maximize the yawing moment and minimize the rolling moment, and with those relations compute an equivalent rudder.

##### Configuration 1

In the mixed-control configuration 1 (figure 4.6), both left and right inboard ailerons (C2) work as ailerons so following the convention described before for the ailerons, their lateral stability coefficients will be doubled and the longitudinal will be null. Inboard ailerons will be defined as  $\delta_{a_1}$  . Since the left and right outboard elevators (C4) work as ailerons, also for the same reason they are defined as  $\delta_{a_2}$  .

The equations representing the influence of  $\delta_{a_1}$  and  $\delta_{a_2}$  in the lateral motion are given by:

$$C_Y = C_{Y\delta_{a_1}} \delta_{a_1} + C_{Y\delta_{a_2}} \delta_{a_2} , \quad (5.17)$$

$$C_l = C_{l\delta_{a_1}} \delta_{a_1} + C_{l\delta_{a_2}} \delta_{a_2} , \quad (5.18)$$

$$C_n = C_{n\delta_{a_1}} \delta_{a_1} + C_{n\delta_{a_2}} \delta_{a_2} . \quad (5.19)$$

As it has been seen already in the configurations analysis, in order to maximize the yawing moment and minimize the rolling moment both control surfaces must deflect in opposite directions, thus minimizing the rolling moment:

$$C_l = 0 \Leftrightarrow \delta_{a_1} = -\frac{C_{l\delta_{a_2}}}{C_{l\delta_{a_1}}} \delta_{a_2} . \quad (5.20)$$

Equation (5.20) defines the relation between  $\delta_{a_1}$  and  $\delta_{a_2}$  for a minimum change in rolling moment defined as zero, which after replacing in the lateral equations will maximize the yawing moment, as we can see in equations (5.21 – 5.23):

$$C_Y = \left( C_{Y\delta_{a_2}} - C_{Y\delta_{a_1}} \frac{C_{l\delta_{a_2}}}{C_{l\delta_{a_1}}} \right) \delta_{a_2} , \quad (5.21)$$

$$C_l = 0 , \quad (5.22)$$

$$C_n = \left( C_{n\delta_{a_2}} - C_{n\delta_{a_1}} \frac{C_{l\delta_{a_2}}}{C_{l\delta_{a_1}}} \right) \delta_{a_2} . \quad (5.23)$$

The resulting expressions, represent the stability coefficients of the equivalent/imaginary rudder, due to the real deflection of the inboard aileron and outboard elevator multiplied by  $\delta_{a_2}$  (here considered the equivalent rudder). The stability coefficients of the equivalent rudder are:

$$C_{Y\delta_r} = C_{Y\delta_{a_2}} - C_{Y\delta_{a_1}} \frac{C_{l\delta_{a_2}}}{C_{l\delta_{a_1}}} , \quad (5.24)$$

$$C_{l\delta_r} = 0 , \quad (5.25)$$

$$C_{n\delta_r} = C_{n\delta_{a_2}} - C_{n\delta_{a_1}} \frac{C_{l\delta_{a_2}}}{C_{l\delta_{a_1}}} . \quad (5.26)$$

The relation in equation (5.20) is defined as a function of the control surface that will be more limited. In the present case,  $\delta_{a_1}$  deflection will be limited by  $\delta_{a_2}$  , therefore  $\delta_{a_1}$  is chosen to be function of  $\delta_{a_2}$  , and used this way in equations (5.17) - (5.19).

For the sake of example, the relation in equation 5.20 after using the stability coefficient values, takes the form of:  $\delta_{a_1} = -0,86 \delta_{a_2}$  . Since the  $\delta_{a_2}$  have a deflection range of  $[-30^\circ, 30^\circ]$ , the  $\delta_{a_1}$  range will be shorter. It is always preferred to write the equations according with the less limitative control surface,  $\delta_{a_2}$  (in this case).

### Configuration 2 and 3

The configurations 2 and 3 (figures 4.6 and 4.7, respectively) will follow the same method applied to configuration 1, since each configuration makes use of two control surfaces, such as the configuration 1.

### Configuration 4

The mixed-control configuration 4 (figure 4.8), has three different control surfaces instead of two as previous configurations. Inboard ailerons (left and right) (C2) are defined as ailerons  $\delta_{a_1}$  (again following the convention stated for the ailerons). Also the outboard and inboard elevators (C4 and C5) are used as ailerons, so they are defined as  $\delta_{a_2}$  and  $\delta_{a_3}$ , respectively.

The equations representing the influence of  $\delta_{a_1}$ ,  $\delta_{a_2}$  and  $\delta_{a_3}$  in lateral motion are given by:

$$C_Y = C_{Y\delta_{a_1}} \delta_{a_1} + C_{Y\delta_{a_2}} \delta_{a_2} + C_{Y\delta_{a_3}} \delta_{a_3}, \quad (5.27)$$

$$C_l = C_{l\delta_{a_1}} \delta_{a_1} + C_{l\delta_{a_2}} \delta_{a_2} + C_{l\delta_{a_3}} \delta_{a_3}, \quad (5.28)$$

$$C_n = C_{n\delta_{a_1}} \delta_{a_1} + C_{n\delta_{a_2}} \delta_{a_2} + C_{n\delta_{a_3}} \delta_{a_3}. \quad (5.29)$$

To minimize the rolling moment, we have:

$$C_l = 0 = C_{l\delta_{a_1}} \delta_{a_1} + C_{l\delta_{a_2}} \delta_{a_2} + C_{l\delta_{a_3}} \delta_{a_3}, \quad (5.30)$$

which has one more degree of freedom than previous configurations. To solve the problem, it was also taken into account the maximization of the yawing moment, by pondering the stability coefficient  $C_{n\delta_s}$  along with  $C_{l\delta_s}$ .

Since the aft wing elevators contribute for the same yawing moment only when deflected in the same direction,  $\delta_{a_2}$  and  $\delta_{a_3}$  were maximized for equal deflections and directions, following the equation (5.31):

$$\delta_{a_2} = \delta_{a_3} = \delta_{a_e}, \quad (5.31)$$

which replaced in the equation (5.30) allows to obtain the next relation between the control surfaces:

$$\delta_{a_e} = -\frac{C_{l\delta_{a_1}}}{C_{l\delta_{a_2}} + C_{l\delta_{a_3}}} \delta_{a_1}. \quad (5.32)$$

After determining the relations between the control surfaces, the deflections can be replaced in the equations (5.27 – 5.29):

$$C_Y = \left( C_{Y\delta_{a_1}} - C_{Y\delta_{a_2}} \frac{C_{l\delta_{a_1}}}{C_{l\delta_{a_2}} + C_{l\delta_{a_3}}} - C_{Y\delta_{a_3}} \frac{C_{l\delta_{a_1}}}{C_{l\delta_{a_2}} + C_{l\delta_{a_3}}} \right) \delta_{a_1}, \quad (5.32)$$

$$C_l = 0, \quad (5.33)$$

$$C_n = \left( C_{n\delta_{a_1}} \delta_{a_1} - C_{n\delta_{a_2}} \frac{C_{l\delta_{a_1}}}{C_{l\delta_{a_2}} + C_{l\delta_{a_3}}} - C_{n\delta_{a_3}} \frac{C_{l\delta_{a_1}}}{C_{l\delta_{a_2}} + C_{l\delta_{a_3}}} \right) \delta_{a_1}. \quad (5.34)$$

Therefore, the equations (5.35 – 5.37) represent the stability coefficients of the equivalent rudder control surface multiplied by  $\delta_{a_1}$ , and they are represented as:

$$C_{Y\delta r} = C_{Y\delta a_1} - C_{Y\delta a_2} \frac{C_{l\delta a_1}}{C_{l\delta a_2} + C_{l\delta a_3}} - C_{Y\delta a_3} \frac{C_{l\delta a_1}}{C_{l\delta a_2} + C_{l\delta a_3}}, \quad (5.35)$$

$$C_{l\delta r} = 0, \quad (5.36)$$

$$C_{n\delta r} = C_{n\delta a_1} \delta_{a_1} - C_{n\delta a_2} \frac{C_{l\delta a_1}}{C_{l\delta a_2} + C_{l\delta a_3}} - C_{n\delta a_3} \frac{C_{l\delta a_1}}{C_{l\delta a_2} + C_{l\delta a_3}}. \quad (5.37)$$

### Configuration 5

The configuration 5 (figure 4.8) makes use of three control surfaces, as the configuration 4. Consequently the methods to achieve the equivalent rudder of configuration 5 are the same as the ones applied in configuration 4.

### Configuration 6

The mixed-control configuration 6 (figure 4.9) uses four distinct control surfaces. In the front wing, the flaps (C1) and inboard ailerons (C2) are used as ailerons, defined as  $\delta_{a_1}$  and  $\delta_{a_2}$  respectively. The control surfaces C4 and C5 in the aft wing will also act as ailerons, represented as  $\delta_{a_3}$  and  $\delta_{a_4}$  respectively.

The equations representing the influence of these four control surfaces in lateral motion are described as:

$$C_Y = C_{Y\delta a_1} \delta_{a_1} + C_{Y\delta a_2} \delta_{a_2} + C_{Y\delta a_3} \delta_{a_3} + C_{Y\delta a_4} \delta_{a_4}, \quad (5.38)$$

$$C_l = C_{l\delta a_1} \delta_{a_1} + C_{l\delta a_2} \delta_{a_2} + C_{l\delta a_3} \delta_{a_3} + C_{l\delta a_4} \delta_{a_4}, \quad (5.39)$$

$$C_n = C_{n\delta a_1} \delta_{a_1} + C_{n\delta a_2} \delta_{a_2} + C_{n\delta a_3} \delta_{a_3} + C_{n\delta a_4} \delta_{a_4}. \quad (5.40)$$

Again, we want to minimize the rolling moment:

$$C_l = 0 = C_{l\delta a_1} \delta_{a_1} + C_{l\delta a_2} \delta_{a_2} + C_{l\delta a_3} \delta_{a_3} + C_{l\delta a_4} \delta_{a_4}. \quad (5.41)$$

To determine the relations between the control surfaces it is insufficient to use only the above equation. Therefore, based on the contributions of the stability coefficients  $C_{n\delta s}$  and  $C_{l\delta s}$  of the four control surfaces and figure 4.9 (which represent the contribution of forces) it is possible to maximize the yawing moment.

Like in configuration 4, both outboard and inboard elevators (C4 and C5) must be deflected in the same direction to produce an equal direction yawing moment, maximizing it:

$$\delta_{a_3} = \delta_{a_4} = \delta_{a_e}. \quad (5.42)$$

From the control surfaces in the front wing, the inboard ailerons (C2) are chosen to maximize the yaw and minimize the roll by deflecting in the opposite direction of the elevators. The inboard ailerons are chosen primarily because their deflection affect more the yawing moment than the flaps (C1). Since they cannot fully reduce the rolling moment to zero, they are going to be actuated in the same proportion as elevators, leading to their maximum deflection:

$$\delta_{a_2} = -\delta_{a_e} . \quad (5.43)$$

Using the previous relations between the control surfaces in equation (5.41), the last relation for the last control surface  $\delta_{a_1}$  can be found:

$$\delta_{a_1} = -\frac{C_{l\delta a_3} + C_{l\delta a_4} - C_{l\delta a_2}}{C_{l\delta a_1}} \delta_{a_e} , \quad (5.44)$$

which, when replaced in the equations of the lateral force and moments, simplify to the deflection of one control surface  $\delta_{a_e}$  :

$$C_Y = \left[ -C_{Y\delta a_1} \left( \frac{C_{l\delta a_3} + C_{l\delta a_4} - C_{l\delta a_2}}{C_{l\delta a_1}} \right) - C_{Y\delta a_2} + C_{Y\delta a_3} + C_{Y\delta a_4} \right] \delta_{a_e} , \quad (5.45)$$

$$C_l = 0 , \quad (5.46)$$

$$C_n = \left[ -C_{n\delta a_1} \left( \frac{C_{l\delta a_3} + C_{l\delta a_4} - C_{l\delta a_2}}{C_{l\delta a_1}} \right) - C_{n\delta a_2} + C_{n\delta a_3} + C_{n\delta a_4} \right] \delta_{a_e} . \quad (5.47)$$

Like in the previous configurations, the equations (5.45 – 5.47) represent the stability coefficients  $C_{Y\delta r}$ ,  $C_{l\delta r}$  and  $C_{n\delta r}$  of the equivalent rudder of configuration 6, multiplied by the deflection of control surface  $\delta_{a_e}$  .

### Configuration 7

The mixed-control configuration 7 (figure 4.9) makes use of all available control surfaces. Each pair of control surfaces is activated as ailerons, so five distinct ailerons are being used. In the front wing, the flaps (C1), inboard and outboard ailerons (C2 and C3) are represented by  $\delta_{a_1}$  ,  $\delta_{a_2}$  and  $\delta_{a_3}$  , respectively. For the aft wing the outboard and inboard elevators (C4 and C5) acting as ailerons are represented by  $\delta_{a_4}$  and  $\delta_{a_5}$  , respectively.

The following equations show the influence of all five control surfaces in the lateral force and moment coefficients:

$$C_Y = C_{Y\delta a_1} \delta_{a_1} + C_{Y\delta a_2} \delta_{a_2} + C_{Y\delta a_3} \delta_{a_3} + C_{Y\delta a_4} \delta_{a_4} + C_{Y\delta a_5} \delta_{a_5} , \quad (5.48)$$

$$C_l = C_{l\delta a_1} \delta_{a_1} + C_{l\delta a_2} \delta_{a_2} + C_{l\delta a_3} \delta_{a_3} + C_{l\delta a_4} \delta_{a_4} + C_{l\delta a_5} \delta_{a_5} , \quad (5.49)$$

$$C_n = C_{n\delta a_1} \delta_{a_1} + C_{n\delta a_2} \delta_{a_2} + C_{n\delta a_3} \delta_{a_3} + C_{n\delta a_4} \delta_{a_4} + C_{n\delta a_5} \delta_{a_5} . \quad (5.50)$$

To minimize the rolling moment, it is applied the same method as for previous configurations:

$$C_l = 0 = C_{l_{\delta a_1}} \delta_{a_1} + C_{l_{\delta a_2}} \delta_{a_2} + C_{l_{\delta a_3}} \delta_{a_3} + C_{l_{\delta a_4}} \delta_{a_4} + C_{l_{\delta a_5}} \delta_{a_5} . \quad (5.51)$$

Once more it stands for a multivariable analysis, which for the equation (5.51) can be solved by maximizing the yawing moment. To achieve that goal, the stability coefficients  $C_{n_{\delta s}}$  and  $C_{l_{\delta s}}$  of all control surfaces must be analyzed, as well as figure 4.9.

The first step is similar to the one taken for the earlier configurations. Given that the elevators C4 and C5 in the aft wing are the ones producing higher yawing moments, they are maximized first, and their deflections must have the same direction, in order that the respective yawing moments do not cancel each other. In this way it is attained the first relation for the elevators:

$$\delta_{a_4} = \delta_{a_5} = \delta_{a_e} . \quad (5.52)$$

All the remaining control surfaces in the front wing produce a yawing moment in the same direction as the elevators when deflected in the opposite direction of elevators, while at same time it cancels the rolling moment. However the contribution of the front wing for the rolling moment is far greater than from the aft wing (almost 3 times higher than aft wing). Thus, it was chosen to maximize first the control surface in the front wing which has greater impact on yawing and which at the same time would be less requested for the rolling motion (like the outboard ailerons). The control surface chosen was the inboard aileron (C2):

$$\delta_{a_2} = -\delta_{a_e} . \quad (5.53)$$

Since the rolling moment from the elevators is practically cancelled by the inboard aileron (C2), the outboard aileron (C3) and flap (C1) can only be actuated in a very short range of deflections to fully cancel the rolling moment. Therefore, the yawing moment produced by them will be limited to the small amount of rolling that they can produce. In this way, to maximize the yaw a rolling moment was introduced in the same direction as the elevators through the use of flaps (C1). The flaps are then maximized to:

$$\delta_{a_1} = \delta_{a_e} . \quad (5.54)$$

The reason behind this unexpected solution, since it will create an opposing yawing moment to the intended moment, is because it will be very small. As it can be confirmed in table 4.7, the  $C_{n_{\delta s}}$  of the flap is insignificant comparing with others, so the impact in the overall yawing moment is expected to be negligible.

On the other hand, the new rolling moment working in the same direction of the elevator moments, allows for a greater use of the outboard ailerons to cancel it. By increasing the actuation of the outboard ailerons the overall yawing moment of aircraft will increase.

Using the previous equations (5.52 – 5.54) in equation (5.51), the final relation is given by the following expression:

$$\delta_{a_3} = -\frac{C_{l\delta a_1} - C_{l\delta a_2} + C_{l\delta a_4} + C_{l\delta a_5}}{C_{l\delta a_3}} \delta_{a_e}. \quad (5.55)$$

Replacing the deflecting relations in the force and moment coefficients, we obtain:

$$C_Y = \left[ C_{Y\delta a_1} - C_{Y\delta a_2} - C_{Y\delta a_3} \left( \frac{C_{l\delta a_1} - C_{l\delta a_2} + C_{l\delta a_4} + C_{l\delta a_5}}{C_{l\delta a_3}} \right) + C_{Y\delta a_4} + C_{Y\delta a_5} \right] \delta_{a_e}, \quad (5.56)$$

$$C_l = 0, \quad (5.57)$$

$$C_n = \left[ C_{n\delta a_1} - C_{n\delta a_2} - C_{n\delta a_3} \left( \frac{C_{l\delta a_1} - C_{l\delta a_2} + C_{l\delta a_4} + C_{l\delta a_5}}{C_{l\delta a_3}} \right) + C_{n\delta a_4} + C_{n\delta a_5} \right] \delta_{a_e}. \quad (5.58)$$

The equations (5.56 – 5.58) represent the stability coefficients  $C_{Y\delta r}$ ,  $C_{l\delta r}$  and  $C_{n\delta r}$  of the equivalent rudder for the configuration 7, multiplied by the control surface  $\delta_{a_e}$ .

### 5.1.3.2 Speed-brake control

The speed-brake control configurations are identical to the mixed-control configurations from the point of view of the control surfaces that are being used to create the yaw. The difference lies in the way to use them, because mixed-control configurations use both left and right control surfaces at the same time (since they are used as ailerons) and speed-brake control only uses either left or right separately depending on the required moment for the motion.

Since the control surfaces used are the same, the proportion between control surface deflections is the same as mixed-control. For example, if outboard elevators (C4) in mixed-control have to deflect 2 times the deflection of the outboard ailerons (C3), the same deflections will be observed in the equivalent speed-brake control configuration using the same control surfaces: left outboard elevator has to deflect 2 times the deflection of the left outboard aileron (and the same goes for the right outboard elevator and aileron if they are used instead of the left ones).

Therefore, the multivariable analysis is accomplished by using the same maximizations and minimizations that are used in the corresponding configurations, in mixed-control. For easier corresponding it was given the same numbering for the equivalent configurations in mixed-control and speed-brake control.

However, the speed-brake control stability coefficients  $C_{n\delta s}$  are only available for a deflection inferior or superior to a certain angle, as it can be seen in table 3.6. So, the addition of the coefficient is not linear, given that the range of deflection of the control surfaces is not the same. Thus a linear approximation will be done, where the equivalent rudder configuration will also have a shorter range of deflection, depending on the limiting control surfaces used. An error analysis will be calculated for the maximum error committed.

### 5.1.4 Equivalent rudder stability coefficients

The stability coefficients of each mixed-control and speed-brake control configurations were calculated using the methods described above, and are resumed in the next table. The deflection range of each configuration, as well as the maximum error of the linear approximations for the speed-brake configurations is presented.

Note that the stability derivatives were maximized for a zero rolling moment coefficient, so for all configurations the stability coefficient  $C_{l_{\delta r}}$  is given by:

$$C_{l_{\delta r}} = 0 . \quad (5.59)$$

<b>Mixed-control</b>		
Configuration	Equivalent rudder [1/rad]	Range
1	$C_{Y_{\delta r}} = -0,144$ $C_{n_{\delta r}} = 0,021$	[-30°, 30°]
2	$C_{Y_{\delta r}} = -0,097$ $C_{n_{\delta r}} = 0,019$	[-30°, 30°]
3	$C_{Y_{\delta r}} = -0,093$ $C_{n_{\delta r}} = 0,022$	[-30°, 30°]
4	$C_{Y_{\delta r}} = -0,192$ $C_{n_{\delta r}} = 0,034$	[-30°, 30°]
5	$C_{Y_{\delta r}} = -0,171$ $C_{n_{\delta r}} = 0,040$	[-30°, 30°]
6	$C_{Y_{\delta r}} = -0,246$ $C_{n_{\delta r}} = 0,041$	[-30°, 30°]
7	$C_{Y_{\delta r}} = -0,133$ $C_{n_{\delta r}} = 0,045$	[-30°, 30°]

Table 5.1 - Mixed-control equivalent rudder stability coefficients

<b>Speed-brake control</b>			
Configuration	Equivalent rudder [1/rad]	Range	Error
1	$C_{Y_{\delta r}} = -0,072$ $C_{n_{\delta r}} = 0,055$	[-20°, 20°]	13,5%
2	$C_{Y_{\delta r}} = -0,049$ $C_{n_{\delta r}} = 0,053$	[-20°, 20°]	15,9%
3	$C_{Y_{\delta r}} = -0,046$ $C_{n_{\delta r}} = 0,035$	[-15°, 15°]	12,5%
4	$C_{Y_{\delta r}} = -0,096$ $C_{n_{\delta r}} = 0,073$	[-20°, 20°]	8,8%
5	$C_{Y_{\delta r}} = -0,085$ $C_{n_{\delta r}} = 0,087$	[-20°, 20°]	10,3%
6	$C_{Y_{\delta r}} = -0,123$ $C_{n_{\delta r}} = 0,089$	[-20°, 20°]	13,6%
7	$C_{Y_{\delta r}} = -0,067$ $C_{n_{\delta r}} = 0,115$	[-20°, 20°]	16,7%

Table 5.2 - Speed-brake control equivalent rudder stability coefficients

All the errors are given in relation to upper bound values, consequently all values computed are in a safe zone where the values are expected to be higher and their maximum error never exceeds 16,7%. Therefore, in a real situation it would be expected higher values of the yawing stability coefficient, which would increase the performance and the control over the lateral motion: the stability coefficients for the speed-brake control are conservatives.

For an easier insight and comparison over the yawing stability coefficients  $C_{n\delta_r}$ , they are represented in the next figure for each configuration.

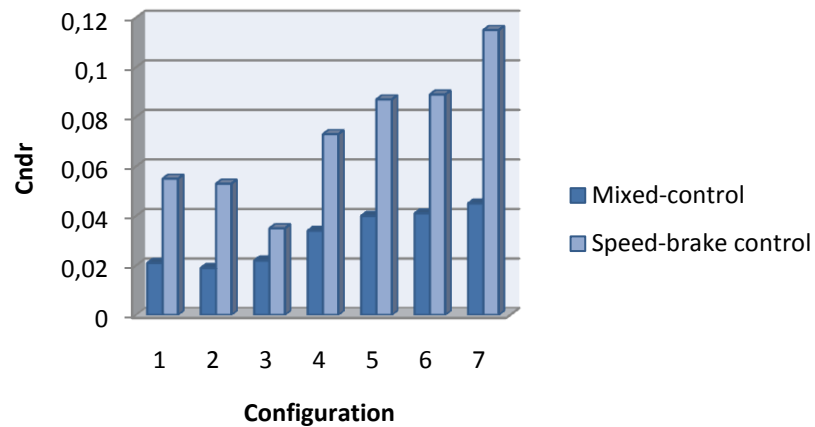


Figure 5.1 - Comparison of the stability coefficient  $C_{n\delta_r}$  for each configuration

From the figure above, it is notable the difference between the efficiency of the mixed-control and the speed-brake control, where the last shows constant contribution of two times higher for almost all configurations.

Some appreciation can be made about the efficiency of the equivalent rudder control surfaces, in which speed-brake control technique configurations clearly present higher results. However, it is still soon to conclude about their action in the dynamic model since the range of deflection is shorter for the speed-brake control configurations.

So, further steps will lead to the analysis of the dynamic response of the aircraft state variables, for a better judgment about the efficiency of the different control methods.

## 5.2 Aircraft open loop system

Before proceeding with the control methods it is necessary to understand how SensorCraft responds to typical control surface deflections. This is called open loop system response.

The open loop system reveals how the state variables of the aircraft change with the input of a control surface.

To demonstrate the open loop response of the system, it was used the *MATLAB*® to define the state space equations of lateral and longitudinal motion. The time-space analysis of the open loop system was tested in the *MATLAB*® multidomain simulation environment *Simulink*®. The longitudinal and lateral representative schemes for the open loop simulation are presented in figure 5.2.

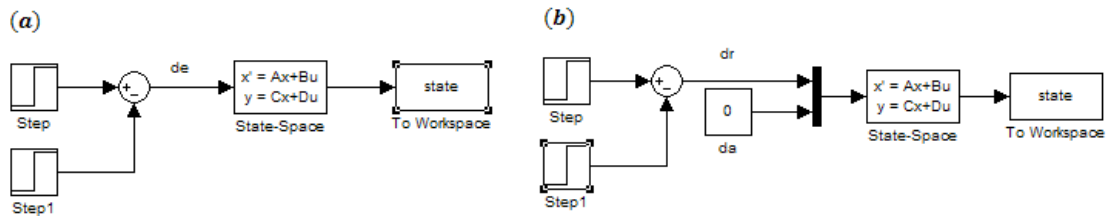


Figure 5.2 - Open loop representative systems for (a) longitudinal and (b) lateral motions

The rectangle signal input of the control surfaces, such as elevator, rudder and aileron, was chosen as a value of 3 degrees as demonstrated in figure 5.3.

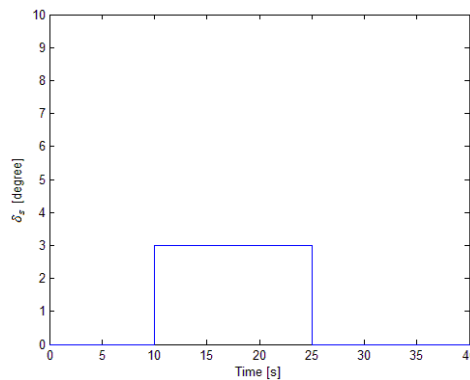


Figure 5.3 - Rectangular signal input of control surfaces

To proceed with the time-space analysis, it was decided to test these inputs for the inboard elevators (C5) in the longitudinal system and for the outboard aileron (C3) and equivalent rudder of speed-brake configuration 1 (C2 and C4) in the lateral system.

The responses of the longitudinal and lateral system are summarized next:

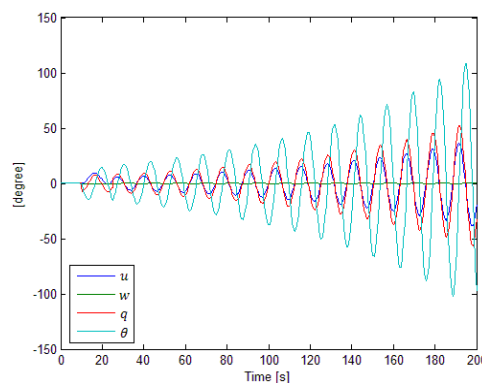


Figure 5.4 - Longitudinal response to a 3 degree rectangular signal in elevators

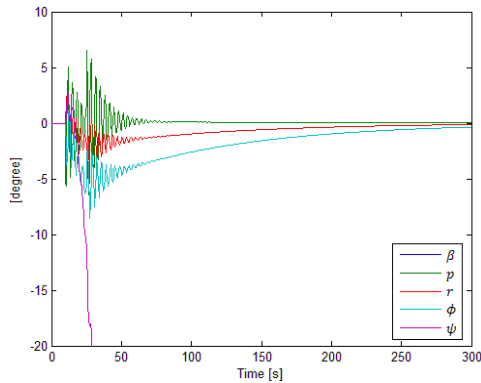


Figure 5.5 - Lateral response to a 3 degree rectangular signal in ailerons

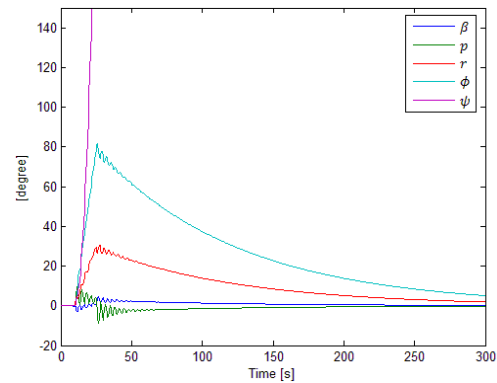


Figure 5.6 - Lateral response to a 3 degree rectangular signal in rudder

Note that the degree unit in the  $y$  axis of the previous graphics denotes that all angle related state variables come in degrees, instead of radians. This is the case of angles (degree) and angular velocity values (degree/s). State variables which are not related with angles are expressed in the SI units, for example the linear velocity comes in m/s. For further state variable graphics this representation will be also used.

The open loop of the longitudinal system from figure 5.4 has an unstable response to the elevators, as it was concluded in the previous Chapter through the analysis of the flying qualities. All the state variables of the longitudinal motion increase their amplitude infinitely, even the vertical velocity  $w$  coloured green although with a lower rate.

From figure 5.5 the open loop of the lateral system has shown to have an average performance to the deflection of ailerons. All the lateral state variables are damped after the perturbation of the ailerons and the system returns to equilibrium. However, since the eigenvalue of the state variable  $\psi$  is located in the origin the convergence is only assured for larger values.

In the case of the response of the lateral open loop to the rudder (figure 5.6), although it is dynamic stable and all state variables are damped, their values are excessively high for a deflection of 3 degrees, when compared with the results of the ailerons deflection. This proves the *level 2* flying quality achieved by the dutch roll mode where the rudder has higher influence, contrasting with the *level 1* quality achieved by the roll mode in which the aileron is the principal control surface.

The state variable  $\psi$  response to the rudder actuation also converges, but to even higher values than figure 5.5.

### 5.3 Control system design

From the analysis of the open loop responses, it is clear that the aircraft needs a control system not only for stabilizing the different motions but also to assure that they can be controlled and inputted into an AFCS (Automatic Flight Control System).

The following AFCS applied to the several test configurations have the objective of comparing the responses of each configuration and their efficiencies to control the aircraft motion.

AFCSs are based in the feedback control, where the system uses the measurement of the output state variables to rectify the control action (input controls). Thus AFCSs guarantee the good behavior of the system and a good relation between the inputs and outputs. The good behavior of the system means that it enhances the flying and handling qualities of the aircraft, which are possible due to the increase of the natural frequency and damping ratio.

The system analysis, as well as the configuration analysis and feedback sizing depend on the methods used. It is possible to distinguish conventional methods and modern methods. In conventional methods it will be approached the stability augmentation through the root locus method, and in modern methods the LQR (Linear Quadratic Regulator) will allow a further study to control the system and attitude variables.

In both methods the determination and sizing of the feedback is what determines the value of the feedback matrix, defined as the gain matrix  $K$ . It is the proper sizing of the gain matrix which will grant the system the improvement of the flying qualities. Using the same state space representation presented in figure 2.9, the typical feedback control system is given for the figure below, where  $K$  is the gain matrix.

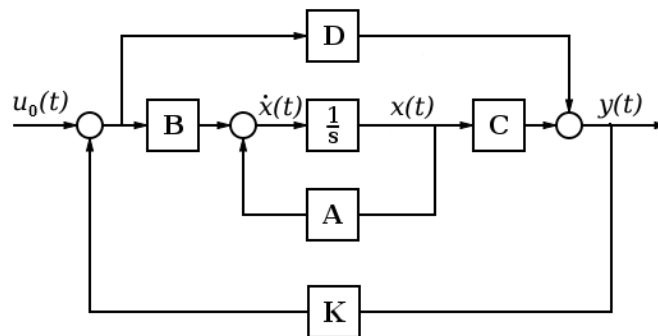


Figure 5.7 - Typical feedback control system

From the state space feedback system in figure 5.7 it is possible to conclude that the relation between the inputs ( $u$ ) and the outputs ( $y$ ) is given for the following expression:

$$u = Ky . \tag{5.60}$$

Replacing the output vector ( $y$ ) for the equation (2.78), we obtain:

$$u = K(Cx + Du) . \tag{5.61}$$

From equations (2.79) and (2.80) the output matrix ( $C$ ) is given by the identity matrix and direct matrix ( $D$ ) by a zero matrix, and equation (5.61) can be simplified:

$$u = Kx . \tag{5.62}$$

The previous equation (5.62) represents the feedback control law, which applied into the system dynamic equations (2.77) and (2.78) translate the dynamic of the feedback control system, as shown in following equations:

$$\dot{x} = (A + BK)x , \quad (5.63)$$

$$y = Cx . \quad (5.64)$$

The term  $A + BK$  in equation (5.63) defines the feedback state coefficient matrix  $A_f$  , which characterizes the parameters of the feedback system, such as damping ratio and natural frequency:

$$A_f = A + BK . \quad (5.65)$$

Thus, using the determinant in equation (4.7) the parameters of the feedback system will be determined by the following equation:

$$|\lambda I - A_f| = 0 . \quad (5.66)$$

Next, conventional and modern methods will be applied in order to stabilize and control the aircraft dynamics.

### 5.3.1 Conventional control method

#### 5.3.1.1 Root Locus

For a conventional approach the root locus method was chosen to design the stability augmentation for the aircraft system. The root locus is a graphical analysis which evaluates how the eigenvalues of a system change with the variation of the gain in the feedback system. The gain is usually resolved for a transfer function, which relates a single output state with a single input variable.

The matrix gain was computed using the *MATLAB*® program for each configuration. For further details the code is presented in Appendix K. And for an equal comparison between configurations, the gain was calculated for an established eigenvalue which grants the stability system augmentation in all configurations.

#### Longitudinal

For the longitudinal motion, the root locus was evaluated for different feedback relations, in which the best solution showed up to be the simultaneous feedback of the rate of pitch ( $q$ ) to the elevators and feedback of the pitch angle ( $\theta$ ) to the elevators. Therefore, the gain matrix was designed for the transfer functions shown below, and the corresponding feedback:

$$\frac{q}{\delta_e} \rightarrow \delta_e = K_q q , \quad (5.67)$$

$$\frac{\theta}{\delta_e} \rightarrow \delta_e = K_\theta \theta . \quad (5.68)$$

where,  $K_q$  and  $K_\theta$  were chosen to have the same gain value.

The sizing of the gain values was accomplished for a chosen point in the root locus graphic which was closer to a line at 45 degrees with the real imaginary axis. The reason to do so is because a point chosen near that line will have a good compromise between the frequency

and damping. Since for root locus an increasing damping can decrease the natural frequency and vice-versa, it represents a commitment between these parameters.

The next figure shows the root locus method applied to the inboard elevators (C5), for the feedback shown in equations (5.67) and (5.68).

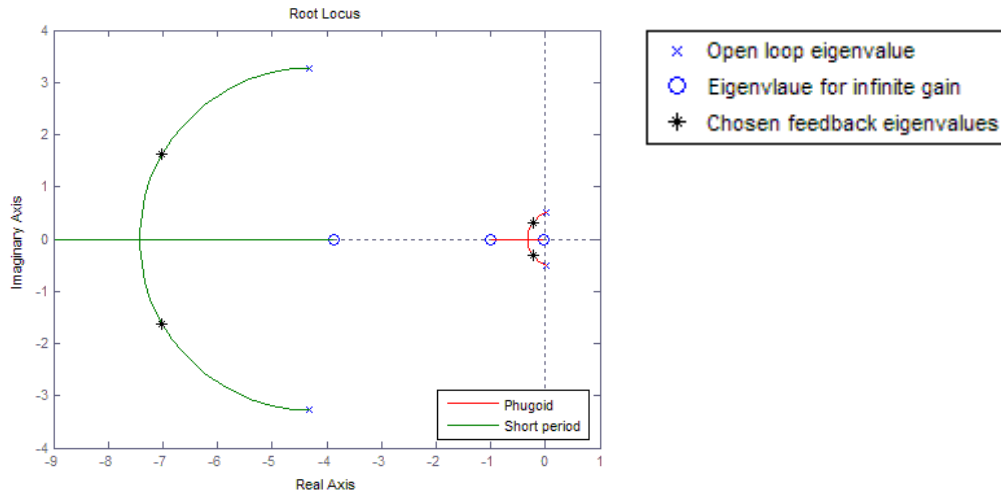


Figure 5.8 - Root locus of longitudinal system and respective legend

From the figure 5.8 the given feedback not only enhanced the phugoid mode but also the short period mode qualities. The selected points marked with a black star represent the points chosen for the feedback system eigenvalues, which resulted in a gain of  $K_\theta = K_q = -0.35$ .

The properties of the longitudinal feedback system are easily determined by the equation (5.66) and are resumed in the next table, as well as the flying qualities:

<i>Mode</i>	<i>Eigenvalue</i>	$\omega_n$ [rad/s]	$\xi$	<i>Level</i>
<i>Short Period</i>	$-6,99 \pm 1,67 i$	7,19	0,97	1
<i>Phugoid</i>	$-0,22 \pm 0,32 i$	0,39	0,56	1

Table 5.3 - Longitudinal feedback system properties

Comparing table 5.3 with table 4.4 it can be seen that the feedback system increased the short period frequency and damping ratio, and a notable increase of the phugoid damping ratio which grant the phugoid mode level 1 flying quality.

### Lateral

For the lateral motion, the best feedback solution to increase the properties of the dutch roll, was the feedback of the rate of yaw ( $r$ ) to the equivalent rudder  $\delta_r$ . The transfer function and the corresponding feedback which determine the gain matrix of the lateral system are represented next:

$$\frac{r}{\delta_r} \rightarrow \delta_r = K_r r . \quad (5.69)$$

The sizing of the gain value  $K_r$ , was chosen in such a way that would increase the properties of the dutch roll predominantly. In figure 5.9 and considering the legend in figure 5.8, it is represented the typical root locus for the given feedback in equation (5.69) where it was used the equivalent rudder of the speed-brake control configuration 1 (C2 and C4).

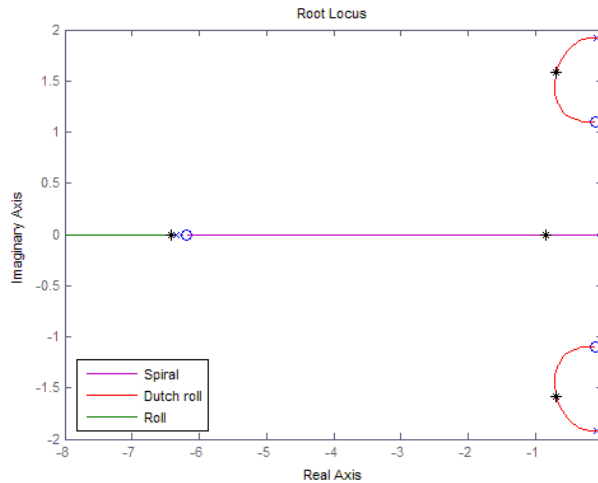


**Figure 5.9 - Root locus of lateral system**

In the previous figure, the sizing of the gain was firstly selected for the solution which better stabilizes the dutch roll. The dutch roll eigenvalue was selected to be located as far left possible, but without reducing the natural frequency greatly. Spiral and roll modes due to the good behavior of the feedback system chosen, also increase their flying quality parameters, but as shown in figure 5.9, the great impact was over the spiral mode which eigenvalue was widely moved to the left unlike the roll mode which nearly did not moved.

The sized gain for this feedback was  $K_r = 0,946$ , and the properties of the lateral feedback system can be found by solving the determinant in equation (5.66). The resulting properties of the lateral modes are resumed in table 5.4.

<b>Mode</b>	<b>Eigenvalue</b>	<b><math>\omega_n</math> [rad/s]</b>	<b><math>\xi</math></b>	<b><math>\xi\omega_n</math></b>	<b>T [s]</b>	<b>Level</b>
<i>Spiral</i>	-0,83	0,83	1	-	-	1
<i>Dutch roll</i>	$-0,68 \pm 1,59 i$	1,73	0,39	0,67	-	1
<i>Roll</i>	-6,42	6,42	1	-	0,16	1

**Table 5.4 - Lateral feedback system properties**

Comparing the results of the lateral feedback system with the results of the lateral open loop system (table 4.5), the feedback of the rate of yaw to the equivalent rudder highly increased the damping of the dutch roll and the frequency of the spiral mode. The roll mode eigenvalue practically did not change its position, since the rudder has not much influence in the roll motion. Therefore, the overall flying qualities of the lateral system were greatly increased for the intended lateral modes, resulting in a level 1 lateral flying quality.

### 5.3.1.2 Simulink® analysis

The time-space analysis of the close loop system (feedback system) was simulated in the *Simulink®* environment. The longitudinal and lateral feedback systems were then built in *Simulink®*, as shown in figure 5.10.

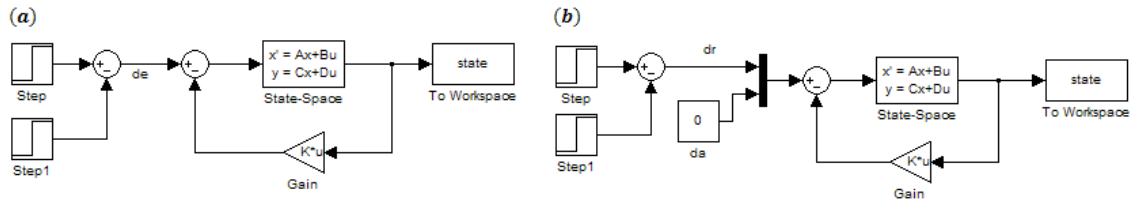


Figure 5.10 - Close loop systems for (a) longitudinal and (b) lateral motions

The rectangle signal input in the control surfaces was chosen as before in figure 5.3. For the time-space analysis, it was chosen the same control surfaces as the ones used in the open loop analysis, thus the inboard elevators (C5) are used in the longitudinal system, the outboard aileron (C3) and the equivalent rudder of speed-brake configuration 1 (C2 and C4) are used in the lateral system.

The longitudinal and lateral responses of the feedback systems, where the gains are given by the previous root locus calculations, are presented in the following figures.

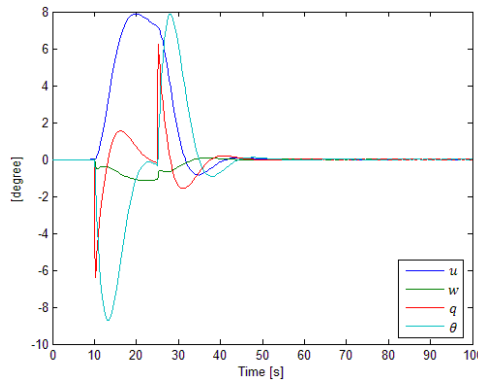


Figure 5.11 - Longitudinal response of feedback system to a 3 degree rectangular signal in elevators

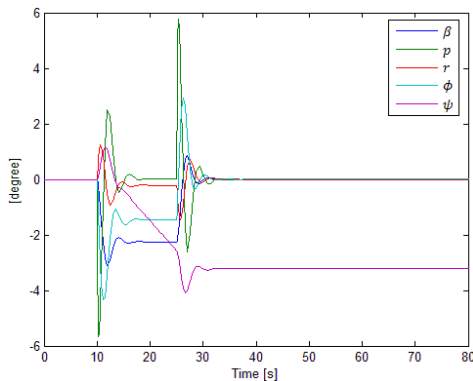


Figure 5.12 - Lateral response of the feedback system to a 3 degree rectangular signal in ailerons

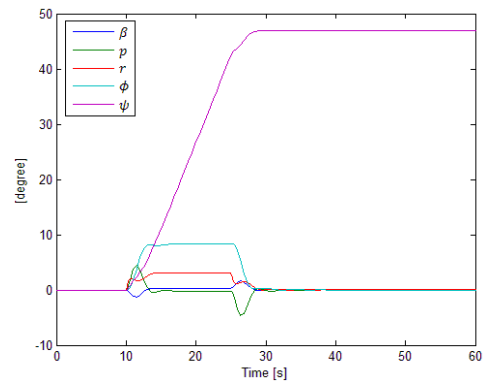


Figure 5.13 - Lateral response of the feedback system to a 3 degree rectangular signal in rudder

Comparing the results obtained for the feedback system with the ones corresponding to the open loop (figures 5.4 – 5.6) the great improvements are shown to be for the longitudinal motion and for the lateral due to rudder deflection. It is an expected result, since from feedback result (tables 5.3) the longitudinal motion improved both modes, specially the unstable phugoid, and the lateral motion improved the dutch roll and spiral mode.

Thus for the longitudinal motion (figure 5.11) all the state variables are reduced to zero after the control surface return to original position, although a very small and negligible oscillation continues in time.

The lateral motion due to the deflection of the ailerons (figure 5.12) presents a faster convergence into the new equilibrium point after the control surface return to the original position than the open loop system. Another improvement is that the undesirable oscillation of the open loop system was greatly attenuated, and the state variable  $\psi$  is now seen to converge much faster. Although the lateral feedback did not aim to improve the roll mode, the good behavior of the chosen feedback system, also moves to the left the values of the spiral and dutch roll eigenvalues, increasing their flying parameters.

Finally, the lateral motion due to the rudder deflection shown in figure 5.13 reveals a very fast convergence of the state variables, right after the perturbation in the control surface ceased. A remarkable difference between the open loop and the feedback system is found in the excessively high values attained for the same control deflection in open loop, which are now highly damped and controlled. Even the state variable  $\psi$  has a fast convergence, proving the efficiency of the applied feedback in the dutch roll.

Resuming, all systems present stable responses and a fast convergence of the state variables. Also another important note is the great change of the heading angle  $\psi$  due to the rudder deflection of  $3^\circ$ , comparing with the change of  $\psi$  due to the aileron deflection.

### *5.3.1.3 Configuration results*

Based on the achieved results for the feedback system, the different configurations will be compared. The comparison will be based on the gain values which represent the required effort of the control surface to control a certain motion. Thus, the higher the gain value the higher will be the deflection to control the disturbance.

#### Longitudinal

For the longitudinal motion the control surfaces tested are the inboard elevators deflecting in the same direction (configuration 1) and the inboard and outboard elevators deflecting in the same direction (configuration 2). In this way, it is planned to conclude about the efficiency of the inboard elevators in the pitch control.

To grant a fair comparison between configurations, it was chosen a gain value which allows the control and stabilization of one configuration, obtaining the correspondent position of the eigenvalues for the given feedback. The comparing configurations will be approximated to the given eigenvalue and calculated their respective gains. Therefore, the gains will be compared for an equal eigenvalues objective.

The results of the root locus for the longitudinal configurations are presented in table 5.5.

<b>Configuration</b>	<b>Phugoid</b>	<b>Short period</b>	<b>Gain</b>
1	$-0,22 \pm 0,32 i$	$-6,99 \pm 1,67 i$	-0,35
2	$-0,21 \pm 0,33 i$	$-6,85 \pm 1,93 i$	-0,2

Table 5.5 - Gains and eigenvalues of the longitudinal configurations

### Lateral

Attending to the same method used for the longitudinal motion, we used an equal value of eigenvalues which stabilize and control the lateral motion. The gains were computed for the mixed-control and speed-brake configurations presented in Chapter 4, and the equivalent rudder stability coefficients are given in tables 5.1 and 5.2 and equation (5.59).

The gain results of the root locus for the lateral configurations are presented in table 5.6, as well as eigenvalues of each configuration.

(Note: To make the notation simpler, mixed-control will be referred as *MC* and speed-brake control as *SBC*, so mixed-control configuration 1 is defined as *MC – 1* as well as speed-brake control).

<b>Configuration</b>	<b>Spiral</b>	<b>Dutch roll</b>	<b>Roll</b>	<b>Gain</b>
<i>MC – 1</i>	-0,90	$-0,65 \pm 1,52i$	-6,38	2,45
<i>MC – 2</i>	-0,88	$-0,66 \pm 1,54i$	-6,39	2,72
<i>MC – 3</i>	-0,87	$-0,67 \pm 1,55i$	-6,40	2,36
<i>MC – 4</i>	-0,90	$-0,66 \pm 1,53i$	-6,39	1,53
<i>MC – 5</i>	-0,86	$-0,67 \pm 1,55i$	-6,39	1,29
<i>MC – 6</i>	-0,88	$-0,66 \pm 1,53i$	-6,38	1,25
<i>MC – 7</i>	-0,86	$-0,68 \pm 1,56i$	-6,40	1,16
<i>SBC – 1</i>	-0,83	$-0,68 \pm 1,59i$	-6,42	0,95
<i>SBC – 2</i>	-0,83	$-0,69 \pm 1,59i$	-6,42	0,99
<i>SBC – 3</i>	-0,83	$-0,68 \pm 1,59i$	-6,42	1,49
<i>SBC – 4</i>	-0,83	$-0,68 \pm 1,59i$	-6,41	0,72
<i>SBC – 5</i>	-0,83	$-0,69 \pm 1,59i$	-6,42	0,60
<i>SBC – 6</i>	-0,84	$-0,68 \pm 1,59i$	-6,42	0,59
<i>SBC – 7</i>	-0,82	$-0,69 \pm 1,60i$	-6,42	0,45

Table 5.6 - Gains and eigenvalues of the lateral configurations

### 5.3.2 Modern control method

The modern control solution chosen consists in the potential of an optimal feedback controller to all state variables and control inputs. It is called Linear Quadratic Regulator (LQR).

From the root locus control method both lateral and longitudinal systems were stabilized and controlled. Considering the longitudinal motion controllable by the root locus results, and as pointed in the beginning of this work, it will focus over the lateral motion since the main problem is the inexistence of the rudder in SensorCraft. Thus the LQR method will be applied only for lateral system.

Two other reasons lead to the investigation of the LQR for the lateral system. The first reason lies in the LQR property of an all state and input variables optimal feedback, which will allow the feedback for both yawing and rolling motions. The second reason and the most important, is that using the LQR method will open a possibility to determine the gain matrix of a flight path control system, which will work as an evaluation method between different configurations.

#### 5.3.2.1 Linear Quadratic Regulator – LQR

##### Introduction

As it was said before, LQR is a modern method which leads to the optimal controller by an all state and input variables feedback. The sizing of feedback gain matrix is determined minimizing the cost function,  $J$ , defined in equation (5.70):

$$J = \int_{t_1}^{t_2} \mathcal{L}(x, u, t) dt, \quad (5.70)$$

where,  $\mathcal{L}$  is the Lagrangian which summarizes the dynamic of the system (state, control and time variables).

The minimizing along with the dynamic equations (2.77) and (2.78) leads to the solution  $u^0$  and to the optimal linear solution of the gain matrix,

$$u^0 = -Kx. \quad (5.71)$$

In the LQR the problem is reduced to:

$$J = \frac{1}{2} \int_{t_1}^{t_2} (x'Qx + u'Ru) dt. \quad (5.72)$$

To minimize the integral the square matrix  $Q$  (related to the state coefficient matrix) and square matrix  $R$  (related to the driving matrix) are used in order to ponder between the different states and inputs to obtain the desirable objective.

The LQR method was computed using *MATLAB*® programmed forms, and it is demonstrated in the *MATLAB*® code source in Appendix K.

Method

To implement the LQR in a flight path control system, the heading state variable ( $\psi$ ) was inputted in the system via command so it can be controlled. Therefore the input command of the system is now the heading instead of control deflections. Thus the gain will operate over the error ( $e$ ), which represents the difference between the commanded variable and the output variable, as it is shown in equation (5.73):

$$e = \psi^{com} - \psi . \tag{5.73}$$

It was also chosen to control via command the state variable bank angle ( $\phi$ ) in order to have an attitude control system over the aircraft.

Thus, the feedback of  $\psi$  and  $\phi$  state variables represents a control command system in an outer loop, and the feedback of the remaining state variables represents a stability augmentation system in an inner loop. This model will be presented further in figure 5.14.

Although the gain matrix computed in LQR stabilized the system, the response of the state variables  $\psi$  and  $\phi$  had no negligible static errors. For that reason the system would not converge to the input commanded values. Thus it was decided to introduce two new integrative states of  $\psi$  and  $\phi$  to cancel the static error.

The new integrative states are given for:

$$\dot{x}_6 = \phi , \tag{5.74}$$

$$\dot{x}_7 = \psi , \tag{5.78}$$

which are introduced in the dynamic state equation as represented below.

$$\begin{bmatrix} \dot{\beta} \\ \dot{p} \\ \dot{r} \\ \dot{\phi} \\ \dot{\psi} \\ \dot{x}_6 \\ \dot{x}_7 \end{bmatrix} = \begin{bmatrix} \dots & \dots & \dots & \dots & \dots & \dots & \dots \\ \dots & \dots & \dots & \dots & \dots & \dots & \dots \\ \dots & \dots & \dots & \dots & \dots & \dots & \dots \\ \dots & \dots & \dots & \dots & \dots & \dots & \dots \\ \dots & \dots & \dots & \dots & \dots & \dots & \dots \\ 0 & 0 & 0 & 1 & 0 & 0 & 0 \\ 0 & 0 & 0 & 0 & 1 & 0 & 0 \end{bmatrix} \begin{bmatrix} \beta \\ p \\ r \\ \phi \\ \psi \\ x_6 \\ x_7 \end{bmatrix} + \begin{bmatrix} \dots \\ \dots \\ \dots \\ \dots \\ \dots \\ 0 & 0 \\ 0 & 0 \end{bmatrix} \dots \begin{bmatrix} \delta_{s1} \\ \delta_{s2} \\ \vdots \end{bmatrix} \tag{5.79}$$

Where  $A$  and  $B$  are defined in equation 2.80.

Using the LQR method in the *MATLAB*® (Appendix H), the gain matrix was determined for the new system represented in equation (5.79). The poles of the new system are given by equation (5.66) and are represented below.

<b>Mode</b>	<b>Eigenvalue</b>	<b><math>\omega_n</math> [rad/s]</b>	<b><math>\xi</math></b>	<b><math>\xi\omega_n</math></b>	<b><math>T</math> [s]</b>	<b>Level</b>
<i>Spiral</i>	-1,38	1,38	1	-	-	1
<i>Dutch roll</i>	$-4,33 \pm 3,65i$	5,66	0,76	4,3	-	1
<i>Roll</i>	-7,48	7,48	1	-	0,13	1

**Table 5.7 - Lateral LQR feedback system properties**

### 5.3.2.2 Simulink® analysis

The time-space analysis of flight path control system was simulated in the *Simulink*® environment. The command feedback and close loop stability augmentation system were then built in *Simulink*® as shown in figure 5.14.

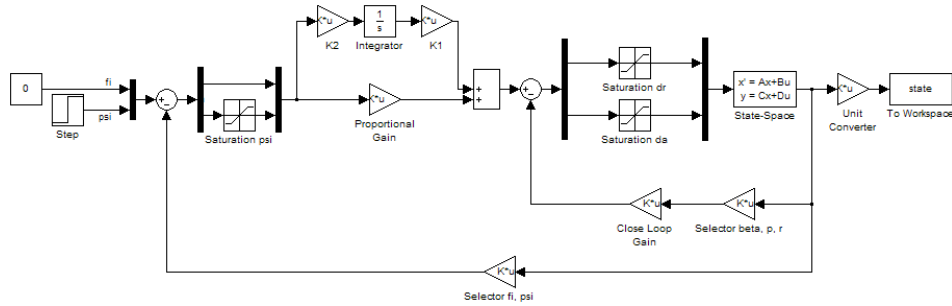


Figure 5.14 - Flight path control system of  $\psi$  and  $\phi$  using the LQR feedback gain matrix

The real system has always limitations either in attitude angles like the bank angle due the proximity to the ground for example, or in the deflection of the control surfaces. For that reason saturation blocks were computed in the *Simulink*® which limit the values of  $\delta_a$  and  $\delta_r$ .

Two different situations of limiting bank angles were tested, one including more accurate control with the bank angle restricted to  $10^\circ$  and another where the bank angle was restricted to  $30^\circ$ :

- Saturation Case 1 –  $\phi \leq 10^\circ$
- Saturation Case 2 –  $\phi \leq 30^\circ$

The system will be tested to an extreme change in the heading angle  $\psi$  of  $90^\circ$  and for a command in the bank angle to level the wings after the perturbation. Therefore, the inputs of the flight path control system are:

$$\psi^{com} = 90^\circ, \quad (5.80)$$

$$\phi^{com} = 0^\circ. \quad (5.81)$$

The  $\psi^{com}$  input is activated at the marked time of 10 s after the simulation started.

The typical response of the state variables to the above command inputs in the time-space analysis are presented in figures 5.15 and 5.16. First figure represents the response of the LQR feedback for the Saturation Case 1 and second figure for the Case 2. The results presented next were achieved using the outboard ailerons as the aileron control surface and the configuration 1 of the speed-brake control as the equivalent rudder.

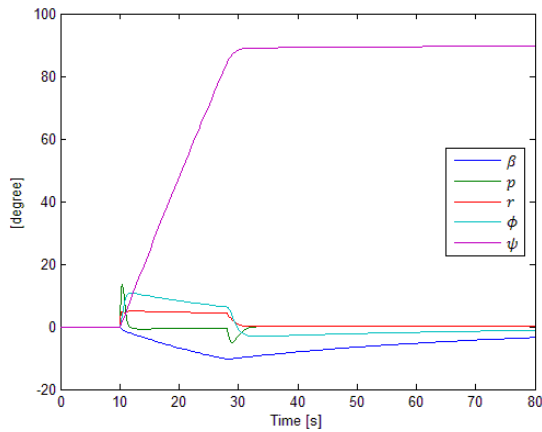


Figure 5.15 - Response of LQR feedback system – Saturation Case 1

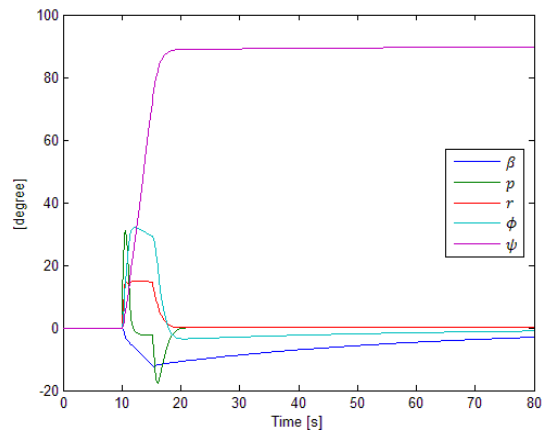


Figure 5.16 - Response of LQR feedback system – Saturation Case 2

Examining figures 5.15 and 5.16 all state variables converge to the extreme request of heading angle change. The heading state variable rapidly converges and stabilizes to the requested input of 90° as desirable. The sideslip state variable after the system reaches the new condition has a slower convergence to zero, but since the sideslip was never a priority to the model requirements and it is between acceptable values it is not a concern.

Comparing the saturation cases it is easily seen that major differences can be observed between the bank angle ( $\phi$ ) and yawing rate ( $r$ ) values of both cases. For the Case 1 where the control is more precise, the bank angle and yawing rate can only reach small limiting values. In Case 2 the values achieved for the same variables are higher since the saturation values are not as much limitative as in Case 1. This directly affects the time of the system to converge to the requested heading angle, because the rate of turn depends either on the bank angle or the yawing rate. The higher the bank angle or yawing rate, the faster the turn will be. So as seen in previous figures, the Case 2 (where the limitations are not so restricted) converges to the 90° much sooner than Case 1.

In conclusion the system is stable and quickly follows the requested inputs with precision. Also, the yawing speed will be as faster as the physical and environment limitations in the bank angle will allow it.

### 5.3.2.3 Configuration results

The objective is now to use the previous LQR feedback system to investigate the different control configurations. The comparison between the several configurations will be done based on the heading angle state variable  $\psi$ , through the analysis of the time to accomplished the requested input.

Using this analysis it will be possible to account for the different range of deflections of control surfaces by means of the computed saturation blocks. The results will be much more reliable to conclude about the efficiency of the equivalent rudders.

For a fair comparison between configurations, the matrices Q and R of the LQR method are the same for all configurations. This will assure that the cost function is minimized for the same contributions of state and input variables.

All configurations were analyzed for the same command inputs given in equations (5.80) and (5.81). The comparison results are presented below for both saturation cases.

*Saturation Case 1*

Mixed-control configurations

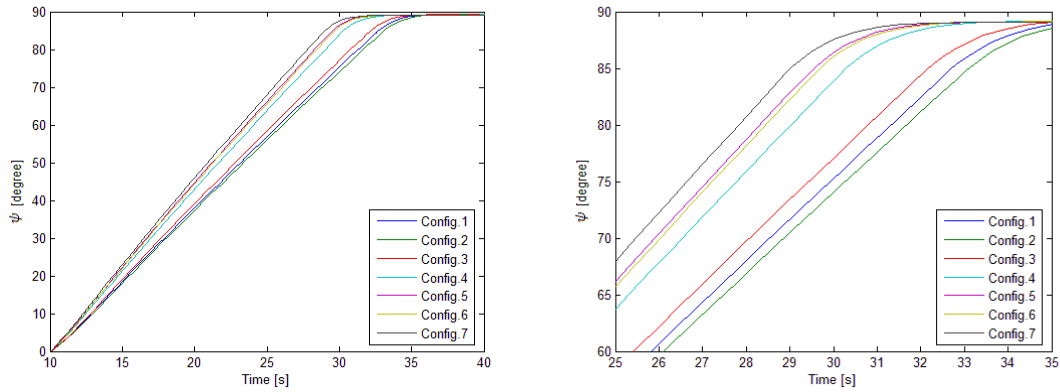


Figure 5.17 -  $\psi$  response for mixed-control configurations (left) and respective zoom (right)

Speed-brake control configurations

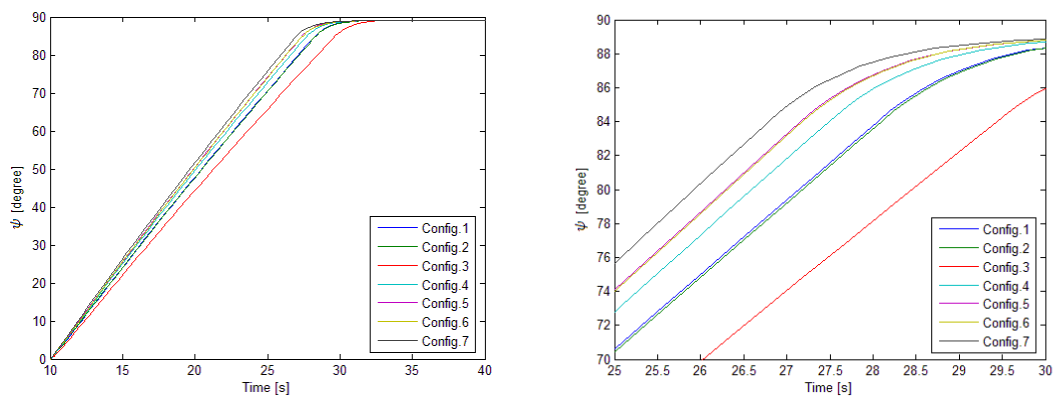


Figure 5.18 -  $\psi$  response for speed-brake control configurations (left) and respective zoom (right)

Mixed-control and speed-brake control comparison:

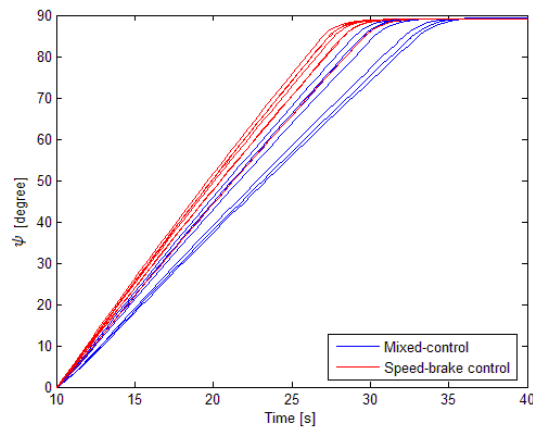


Figure 5.19 -  $\psi$  response comparison between mixed-control and speed-brake control

Saturation Case 2

Mixed-control configuration

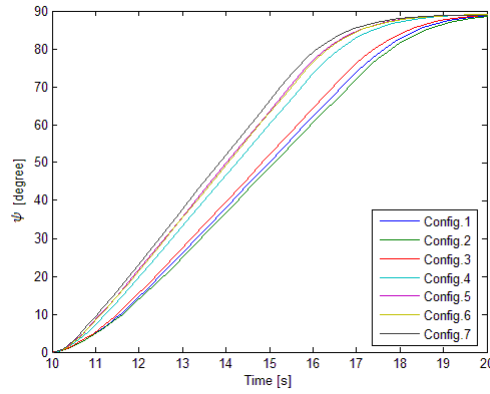


Figure 5.20 -  $\psi$  response for mixed-control configurations

Speed-brake control configuration

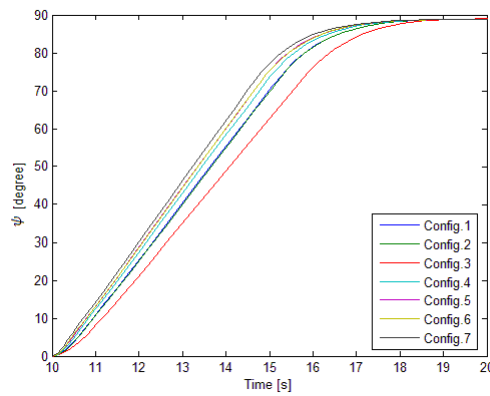


Figure 5.21 -  $\psi$  response for speed-brake control configurations

Mixed-control and speed-brake control comparison

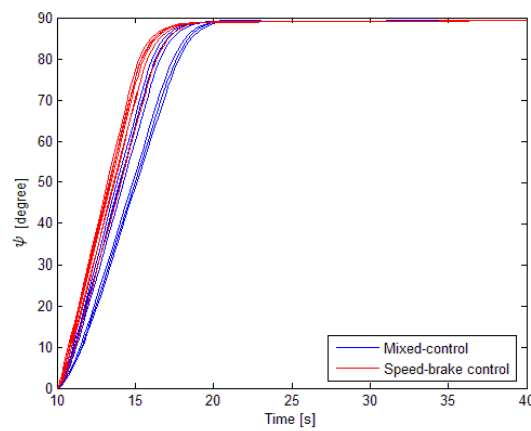
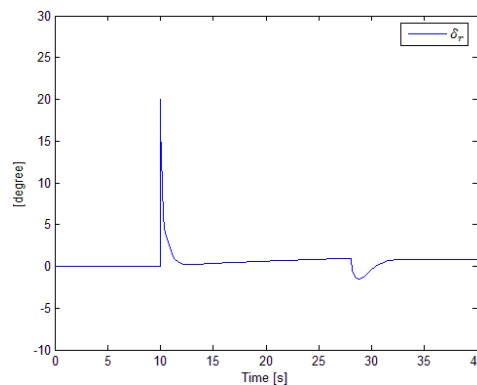


Figure 5.22 -  $\psi$  response comparison between mixed-control and speed-brake control

For the precise control of aircraft motion, the results of mixed-control configurations (figure 5.17) are the ones expected and reflect the influence of the stability coefficients. The mixed-control configurations 5 and 6 in figure 5.17 are superimposed. The speed-brake control configurations (figure 5.18) also present a clear contribution of the stability coefficients over the aircraft ability of a faster turn, where the higher the yawing moment stability coefficient the faster the system becomes. Speed-brake control configurations 1 and 2, as well as configurations 5 and 6 are superimposed.

For the less limited fly condition, Saturation Case 2, the same graphical arrangement is observed for both mixed-control and speed-brake control (figure 5.20 and 5.21), as it was already observed in the Saturation Case 1 configurations. However the convergence times are much faster for the Case 2, since it allows higher bank angle and yawing rate values.

The surprising analysis was the comparison between mixed-control and speed-brake control for either Case 1 or Case 2 limitations (figure 5.19 and 5.22 respectively). Although the speed-brake control configurations were limited in the deflection of control surfaces, almost all (except configuration 3) these configurations presented better results than all mixed-control configurations. After some investigation, it was concluded that this happened not only due to the values of the stability coefficients, but also because the speed-brake control surfaces were not highly requested to their limits as shown in the next figure.



**Figure 5.23 - Equivalent rudder use during the requested heading angle change**

As confirmed in figure 5.23 the maximum values are requested for a very small time period, which allows to conclude that the control surface deflection constraints are not limiting the response in such a way that affects the system performance.

Based on what was presented before and from figures 5.19 and 5.22, the speed-brake control is concluded to have a faster convergence to the requested command inputs.

From figures 5.19 and 5.22 another notable feature, is that for the Saturation Case 1 the configurations mixed-control and speed-brake control are found to be more far apart from each other than in Case 2. Again, this deals about the limitations to the bank angle. Increasing the limit of the acceptable bank angle, this angle will have more influence than the yawing moment. Although it can be concluded that for high bank angles, the turning velocity has a highly contribution from the bank angle (rolling) and not so much reliant on the rudder efficiency, on the other hand the rudder importance for the turning ability and yawing control will be greater for the aircraft accurate control, where bank angle has a more restricted range of variation.

## Chapter 6

# Results Analysis

### 6.1 Configurations results analysis

For the aircraft longitudinal motion, the modes were successfully controlled and stabilized using a close loop feedback of the pitch angle and pitch rate. The evaluated configurations were the inboard elevators (configuration 1) and the inboard and outboard elevators together (configuration 2). From the matrix gain results (table 5.3) the use of the configuration 2 instead of configuration 1 only represents a reduction of 43% from the gain value of configuration 1.

As stated before, the gain value represents the amount of effort requested to a control surface to control a certain motion. Thus, a higher value of the gain represents a higher effort to be requested to the control surface, as confirmed in equation (5.62).

Therefore, since the gain did not change much with the addition of the outboard elevators (C4) (43%), the configuration 2 will not represent a great improvement for the longitudinal performance of the aircraft. This is explained by analyzing the distance of the outboard elevators from the cg of the aircraft, which is smaller than the inboard elevators, as confirmed in figure 2.2, giving the outboard elevators a smaller effect in the pitching moment.

In conclusion the longitudinal motion shows a stabilized and controlled response to the feedback of the configuration 1. Thus, the use of the inboard elevators has a good efficiency to control the longitudinal motion, but can be combined with the outboard elevators if a certain flight condition demands a more precise control.

The conventional and modern control methods, used in the lateral motion analysis were quite conclusive, regarding the control strategies investigated. Through the analysis of the flight path control system, it was possible to compare the performance of mixed-control and speed-brake control strategies, for the real limitations of the control surface deflections. The results for a severe request in the heading angle of  $90^\circ$  were clear enough, verifying an always faster change in the heading for all the speed-brake control configurations (except configuration 3) than all other mixed-control configurations.

Moreover, in agreement with the flight path control system results are the results obtained from the close loop system (root locus feedback). Examining the close loop gain values of all configurations, the speed-brake control configurations (except configuration 3) reveal smaller

values than the mixed-control configurations. This means less effort for the speed-brake control configurations to achieve a same objective, thus proving their efficiency in comparison with the mixed-control configurations.

Therefore, from the analysis of both flight path control system and close loop gains, it was reached the conclusion that speed-brake control strategies have higher efficiency to control and stabilize the yawing moment than the mixed-control strategies. This analysis is easily seen in figure 5.19 representing the convergence speed of the heading angle, and in the next graphic which will emphasize the results obtained for gain values each of configuration.

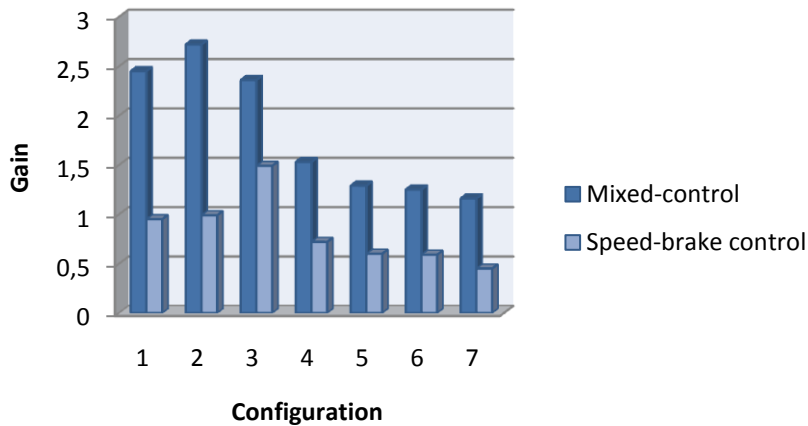


Figure 6.1 - Comparison of the close loop gains for each configuration

Comparing the results for Saturation Case 1 and Case 2 (figures 5.19 and 5.22, respectively), it can be seen that between different configurations, the improvement in the time of convergence from one configuration to another is greater in Case 1 (since configurations are further away from each other). This was explained before by constraints applied on the bank angle, if the constraint limits are not tight, the rate of turn will be much more affected by the aircraft bank angle than for the yawing efficiency of the rudder. Consequently, it will be more difficult to perform the evaluation of the yaw efficiency between the several configurations. Therefore, the analysis must be conducted for the more restricted case, Saturation Case 1, where the rudder efficiency has more impact.

Due to the previous reasons, the analysis will proceed only for the speed-brake control configurations and Saturation Case 1.

For the first three configurations, which make use of two control surfaces, the configuration 3 is the one with the worst results, and so it is excluded.

Between configuration 1 and 2 the results achieved are almost coincident as confirmed in figure 5.18 and in table 5.6. Since configuration 2 makes use of the outboard ailerons (C3) and those control surface are essential to the roll motion, this configuration loses its performance comparing with configuration 1 which do not use any primary control surface belonging to other motion.

Comparing configuration 4 with 5 and configuration 6 with 7, it is verified that the replacement of the inboard ailerons (C2) for the outboard ailerons (C3) and the additional use of the outboard ailerons (C3) respectively, only introduces small changes either in the  $C_{n_{\delta r}}$ , or in the close loop gain or in the convergence times of  $\psi$ . The loss in the autonomy of the rolling motion of the aircraft does not justify their use. Thus, configurations 5 and 7 are excluded.

In resume, the configurations have been reduced to 1, 4 and 6. Between the configurations 4 and 6 there is an improvement in using the configuration 6 for the same impact in the pitching moment. This is not only because the amount of drag force produced by numerous control surfaces, but also because in configuration 4 the inboard ailerons (C2) cannot cancel the rolling moment induced by both elevators, thus the elevators are restricted to smaller deflection angles. In configuration 6, the addition of the flaps cancels the rolling moment produced by elevators, enabling the elevators maximum contribution for the yawing moment. Moreover, the flaps are used at 23% of the actual deflection in other surfaces (equation (5.44)), which enables its use for different requests.

In conclusion, the resulting speed-brake strategies which best stabilize and control the yaw motion are configurations 1 and 6. The difference between these two configurations lies on the desirable autonomy for the longitudinal motion, knowing that configuration 1 does not use the inboard elevators (C5) like configuration 6 does, allowing for a higher control over longitudinal motion. Comparing the root locus gains and the stability coefficients  $C_{n_{\delta r}}$  the configuration 6 presents a general improvement of 38%. Therefore, it was considered both speed-brake control configurations 1 and 6 as the best for control the aircraft yaw, and their use will depend over the real situation where the aircraft is being submitted.

## 6.2 Qualitative validation with the SensorCraft heuristic model

Since we do not have access to experimental results; and in order to validate the conclusions obtained in this work, a qualitative comparison was done with the flight tests results from a heuristic model, that was being developed simultaneously in another thesis [20].

The materials chosen for the heuristic model were: the foam (roofmate) as main material, to grant that the frame and airfoils shape represent the SensorCraft with precision; glass and carbon fibres materials were also used as reinforcements of the main frame. Material density, price, resistance, flexibility, and repairing efforts after crashes were the reasons which lead to this choice of materials [20].

The Joined-Wing heuristic model was scaled by a factor of 1:3 (from the Joined-Wing SensorCraft), to allow visualization at naked eye of its flight characteristics during the tests. The definition of the airframe contour and matching between components has been done using Computer Aided Design (CAD) software like shown in figure 6.1 [20]:

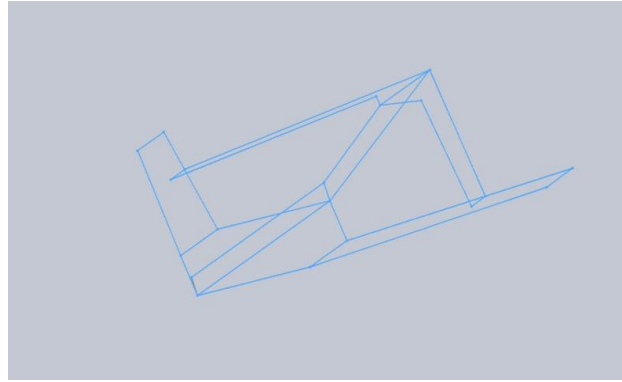


**Figure 6.2 - Heuristic model airframe contour [20]**

The model was built in five separate components for later assembly: one tail boom, two front wings (including fuselage), and two aft wings. The different components were cut with precision using a Computer Numerically Controlled (CNC) machine, and the glass and carbon fibres were applied to each component using a vacuum impregnation process. During the vacuum process, the wings were subjected to a compression twist to accomplish the twist corrections. Finally, after the assembly of all components has been made, the instrumentation was mounted such as servos, receivers, batteries and two Electric Ducted Fans (EDF) [20].

The final assembly of the Joined-Wing heuristics model is shown in the following figure:



**Figure 6.3 - Joined Wing SensorCraft 3 [20]**

The flight tests of the Joined-Wing model were performed via radio controller. Because the radio controller used only 8 channels, it was necessary to use the radio programming and to connect to the same receiver port different devices, in order to command all the control surfaces and EDFs [20].

The important tests to compare in this thesis are the yaw tests. Therefore, the performed yaw flying tests used the different configurations of mixed-control and speed-brake control presented before (Chapter 4). However, some complex configurations were impossible to test, because of the few channels available of the radio controller. The configurations excluded were the 6 and 7 for both control strategies.

The flight tests results were based on observation of the aircraft responses to the control inputs, and on the pilot's feedback. To compare the results it was decided to attribute a scale from 1 to 3 (where 1 is the worst and 3 is the best qualification) to define the stability and velocity of each configuration. The stability parameter defines the behavior of the aircraft, after the rudder equivalent surface has been applied. For example, verifying if the aircraft did not influenced the other motions much besides the desirable yaw motion. The velocity parameter defines the turning velocity of the aircraft, after the rudder equivalent surface has been applied [20].

For all mixed-control and speed-brake configurations, which used the main control surfaces of the roll and pitch motions (outboard ailerons and inboard elevators, respectively) to control the yaw, resulted in a loss of autonomy of the aircraft. The aircraft could not successfully control either roll or pitch with that yaw configuration. For that reason, the stability parameter assigned to all those configurations was 2 and 1.

Therefore, the configurations which better control the yaw motion, are classified accordingly to the defined parameters in next table.

<b>Configuration</b>	<b>MC-1</b>	<b>SBC-1</b>
Velocity	3	3
Stability	2	3

**Table 6.1 - Equivalent rudder classifications**

The obtained flight test results, through the qualitative analysis of the velocity and stability parameters (defined in Chapter 6), are in agreement with the theoretical results. It was been verified that any configuration using the pitch or roll main control surfaces as an equivalent rudder, will result in a loss of either pitch or roll autonomy that not justifies their use.

Of all configurations possible to be tested, the comparison in table 6.1 evidences that even for a slight change of the parameters evaluated, better results were attained for the speed-brake configurations than for mixed-control. In conclusion, the theoretical and the qualitative flight test results show good agreement for the solutions regarding yaw control.



## Chapter 7

# Conclusions and Future Work

Several control strategies for the SensorCraft aircraft were analyzed. The primary challenge was to stabilize and control the yawing lateral motion due to the inexistence of an effective rudder control surface.

Starting with the determination of the aircraft equations of motion, till the determination of the stability coefficients many approaches were made due to the SensorCraft non conventional structure.

After several investigations using feedback systems, computation, analysis of stability coefficients and flight path control systems, the conclusion was reached that mixed-control strategies have inferior results than speed-brake control strategies to control the aircraft yaw. The lateral components of the force created in the dihedral and anhedral wings, have a lower performance to control the yawing moment comparing with the drag force. Even though the mixed-control did not have great results for the SensorCraft, due to the low angles of dihedral and anhedral, it is a solution to keep in mind for aircrafts where the wings have higher angles.

The speed-brake control configurations which better control the aircraft yaw were the configurations 1 and 6. These two configurations stand out because of their significant efficiency to control the lateral motion and at the same time did not decrease the autonomy of the aircraft rolling motion and pitching motion (configuration 1).

Between configurations 1 and 6, an increase of the yawing stability coefficient of 38% for configuration 6 was observed. Nevertheless it involves the use of twice the number of control surfaces. Therefore, the use of each configuration will depend on the flight condition, precision and aircraft real environment situations.

The comparison with a Joined-Wing heuristic model resulted in a qualitatively superior yaw control for the speed-brake configurations instead of the mixed-control configurations. The speed-brake configuration 1 demonstrated higher qualities in controlling the yaw motion. Therefore the flight test results showed a strong agreement with the theoretical results.

The future work can continue using the currently concluded study about the control surfaces effect and efficiency over the different motions. The next aim should be the sensors integration and the design of an appropriate control system for the whole aircraft, allowing for the aircraft to follow any marked object or a determined trajectory, while being commanded from a ground station. The design of a control allocator can be explored to build an optimal controller, which can defines the mixing priorities of the control surfaces in order to achieve the optimal deflections, for each requested aircraft attitude.

The real size SensorCraft is being constructed in this very moment in Instituto Superior Técnico and it is planned to flight in the next two years.

## References

- [1] Trimble, Stephen, *“Over the Horizon”*, Flight International publication, Wright Patterson Air Force Base, Ohio, July 2005.
- [2] Snyder, R., Hur, J., Strong, D., and Beran, P. S., *“Static Aeroelastic Analysis of a High-Altitude Long-Endurance Joined-Wing Aircraft”*, 46th AIAA/ASME/ASCE/AHS Structures, Structural Dynamics, and Materials Conference, Austin, April 2005.
- [3] Taylor, Michael J. H., *Jane's Encyclopedia of Aviation*, London Studio Editions, 1989, pp. 161.
- [4] Wolkovitch, J., *“Joined Wing Aircraft”*, US Patent 3,942,747, March 1979.
- [5] Wolkovitch, J., *“Joined Wing Aircraft”*, US Patent 4,365,773, December 1982.
- [6] Wolkovitch, J., *“The Joined Wing: An Overview”*, Journal of Aircraft, Vol. 23, March 1986, pp. 161-178.
- [7] Loureiro, João P.S., *“Design of a Joined Wing Remotely Piloted Vehicle for Aeroelastically Scaled Flight Tests”*, Master Thesis, Universidade Técnica de Lisboa – Instituto Superior Técnico, September 2008.
- [8] Lucia D.J., *“The SensorCraft Configurations: A Non-Linear AeroServoElastic Challenge for Aviation”*, 46th AIAA/ASME/ASCE/AHS/ASC Structures, Structural Dynamics & Materials Conference, Austin, Texas, April 2005.
- [9] Suleman, A., Richards, J., Costa, Capt. J., *“2009 Progress Report, 5m RPV for Exploring Joined Wing Gust Response”*, 2010.
- [10] Aerospaceweb.org, Reducing Landing Distance, accessed on April 9<sup>th</sup> of 2011, in the web site: <http://www.aerospaceweb.org/question/propulsion/q0181.shtml>.
- [11] James, Michael, RC Airplane Parts and Controls, accessed on April 9<sup>th</sup> of 2011, in the web site: [http://rcvehicles.about.com/od/rcairplanes/ss/RCAirplaneBasic\\_8.htm](http://rcvehicles.about.com/od/rcairplanes/ss/RCAirplaneBasic_8.htm).
- [12] McLean, D., *Automatic Flight Control Systems*, Prentice Hall, 1990.

[13] Author: Inductiveload, Wikimedia Foundation, Source: Own work, accessed on April 10<sup>th</sup> of 2011, in the web site:

[http://commons.wikimedia.org/wiki/File:Typical\\_State\\_Space\\_Model\\_\(CT\).svg](http://commons.wikimedia.org/wiki/File:Typical_State_Space_Model_(CT).svg).

[14] Drela, Mark, Massachusetts Institute of Technology, Department of Aeronautics and Astronautics, accessed in the web site: <http://web.mit.edu/drela/Public/web/avl/>.

[15] Anderson, J. D., *Fundamentals of aerodynamics*, 2<sup>nd</sup> Ed., McGraw-Hill, 1991.

[16] Roskam, Jan, *Airplane Design, Part VI: Preliminary Calculation of Aerodynamic, Thrust and Power Characteristics*, The University of Kansas, 1990.

[17] Drela, Mark, Massachusetts Institute of Technology, Department of Aeronautics and Astronautics, accessed in the web site: <http://web.mit.edu/drela/Public/web/xfoil/>

[18] University of Ljubljana, Lecture 6.1: Concepts of Stable and Unstable Elastic Equilibrium, accessed on April 11<sup>th</sup> of 2011 in the web site:

<http://www.fgg.uni-lj.si/kmk/esdep/master/wg06/l0100.htm>.

[19] Cook, M. V., *Flight Dynamics Principles*, Elsevier, 2<sup>nd</sup> Ed., 2007.

[20] Antunes, Luis, *Design and Manufacturing of a Joined-Wing Experimental Flight Demonstrator*, Master Thesis, Universidade Técnica de Lisboa – Instituto Superior Técnico, June 2011.

[21] Parts of an Airplane and Their Functions, Virtual SKIES, National Aeronautics and Space Administration, accessed on April 9<sup>th</sup> of 2011, in the web site:

<http://quest.arc.nasa.gov/aero/virtual/demo/aeronautics/tutorial/structure.html>.

[22] Bullard, Douglas, Flying Wings, accessed on April 9<sup>th</sup> of 2011 in the web site: [http://www.nurflugel.com/Nurflugel/n\\_o\\_d/weird\\_02.htm](http://www.nurflugel.com/Nurflugel/n_o_d/weird_02.htm).

# Bibliography

- Bell, A., Fromm, F., Lowery, S., Riggs, S., Sleeper, B., Tamayo, M., Todd, J., Usmanov, O., *“Design and Optimization of a Joined-Wing Aircraft”*, AIAA, 2007-2008.
- Bernal, Prof. Luis, Dorman, Paul, *“Study of the Aerodynamics of a Small UAV using AVL Software”*, April 2006.
- Bond, V., *“Flexible Twist for Pitch Control in a High Altitude Long Endurance Aircraft with Non Linear Response”*, Dissertation Prospectus, December 2006.
- Boschetti, Pedro J., Cárdenas, Elsa M., Amerio, Andrea, Arévalo, Ángela, *“Stability and Performance of a Light Unmanned Airplane in Ground Effect”*, AIAA 2010-293, January 2010.
- Boschetti, Pedro J., Cárdenas, Elsa M., Amerio, Andrea, *“Stability of an Unmanned Airplane using a Low-Order Panel Method”*, AIAA 2010-8121, August 2010.
- Bowman, J., *“Stability & Control Analysis of AFRL Radio-Controlled Joined-Wing”*, AFRL/VASA, WPAFB, OH 45433.
- Burns, Roland S., *Advanced Control Engineering*, Butterworth Heinemann, 2001.
- Craft, R., *“Drag Estimates for the Joined-Wing Sensor Craft, Master Thesis”*, Air Force Institute of Technology – Air University, June 2005.
- Dittmar, Josh E., *“Integrated Conceptual Design of Joined-Wing SensorCraft using Response Surface Models”*, Master Thesis, Air Force Institute of Technology – Air University, Nov 2006.
- Jung, D., Tsiotras, P., *“Modeling and Hardware-in-the-Loop Simulation for a Small Unmanned Aerial Vehicle”*, AIAA, Georgia Institute of Technology, Atlanta, GA, 30332-0150.
- Lee, C.-S., Hsiao, F.-B., Jan, S.-S., *“Design and implementation of linear-quadratic Gaussian stability augmentation autopilot for unmanned air vehicle”*, THE AERONAUTICAL JOURNAL, VOLUME 113 N° 1143, pp. 275-290, May 2009.
- Li, W.-q., Ma, J.-j., Zheng Z.-q., Peng X.-f., *“Robust Controller Design to Uncertain Nonlinear Tailless Aircraft”*, The International Federation of Automatic Control, pp. 5980 – 5985, July 2008.

Littleton, Craig A., *“Autonomous Unmanned Aerial Surveillance Vehicle – Autonomous Control and Flight Dynamics”*, Bachelor degree, University of Southern Queensland – Faculty of Engineering and Surveying, October 2005.

Lourenço, João M. A., *“Aerodynamic Analysis of a Joined Wing Aircraft”*, Master Thesis, Universidade Técnica de Lisboa – Instituto Superior Técnico, October 2008.

McClelland, William A., *“Inertia Measurement and Dynamic Stability Analysis of a Radio-controlled Joined-Wing Aircraft”*, Master Thesis, Air Force Institute of Technology – Air University, March 2006.

Melin, Tomas, *“A Vortex Lattice MATLAB Implementation for Linear Aerodynamic Wing Applications”*, Royal Institute of Technology – Department of Aeronautics, December 2000.

Nelson, Robert C., *Flight Stability and Automatic Control*, McGraw-Hill, March 1989.

PEREIRA, Pedro E.R., *“Aeroelastic scaling and optimization of a joined-wing aircraft concept”*, PhD Thesis, Universidade Técnica de Lisboa – Instituto Superior Técnico, May 2008.

Reich, G., Bowman, J., Sanders, B., *“Large-Area Aerodynamic Control for High-Altitude Long-Endurance Sensor Platforms”*, Journal of Aircraft, Vol. 42, N° 1, January – February 2005.

Rogers, David F., *“Flight Determination of Partial-Span-Flap Parasitic Drag with Flap Deflection”*, U. S. Naval Academy, AIAA, vol. 47, n°2, pp. 551-555, 2010.

Roskam, Jan, *Airplane Flight Dynamics and Automatic Flight Controls: Part I and Part II*, Darcorporation, January 2001.

Sivaji, R., Marisarla, S., Narayanan, V., Kaloyanova, V., Ghia, U., Ghia, K., *“Aerodynamic and Structural Analysis of Joined Wings of Hale Aircraft”*, Computational Fluid Dynamics Research Laboratory, University of Cincinnati, Cincinnati, pp. 152 – 164, OH 45221-0072, USA.

Stenfelt, G., Ringertz, U., *“Lateral Stability and Control of a Tailless Aircraft Configuration”*, Journal of Aircraft, Vol. 46, N°. 6, November – December 2009.

Stevens, Brian L., Lewis, Frank L., *Aircraft Control and Simulation*, John Wiley & Sons, Inc., September 2004.

# Appendix

## Appendix A – Angles and ratio definitions

### Swept

The wing sweep angle is defined as the angle between the  $Y$ -axis and the line that joins the root and tip at 25% chord. It is defined positive for back swept wings, and negative for forward swept wings.

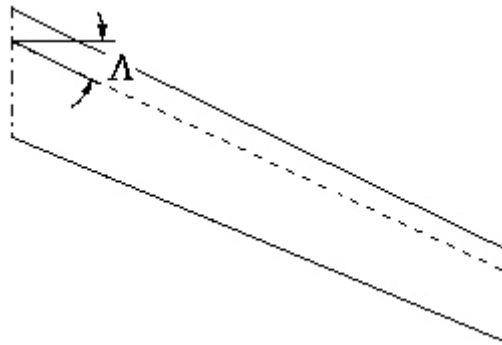


Figure A.1 - Sweep angle definition

### Dihedral

Dihedral angle is the upward angle from horizontal of the forward and aft wings. For negative dihedral angles it is called anhedral angle.



Figure A.2 - Dihedral angle definition [21]

## Twist

Twist angle is the angle in  $XZ$ -plane between the root chord line and the tip chord line. It is defined positive twist for a wing twisting downwards along the span towards the tip, and negative for the inverse situation.

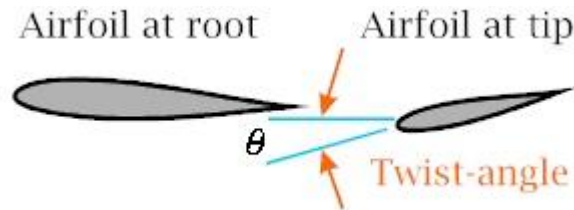


Figure A.3 - Twist angle definition [22]

## Taper ratio

Taper ratio is the ratio of the tip chord over the root chord, given by the following expression:

$$\lambda = \frac{c_{tip}}{c_{root}}. \quad (A.1)$$

## Appendix B – SensorCraft characteristics and geometric parameters

The principal characteristics and geometric parameters used for the SensorCraft analysis are described in table B.1.

<b>Parameters</b>	<b>Value</b>	<b>Unit</b>
$m$	93	$Kg$
$I_{xx}$	61,5	$Kg.m^2$
$I_{yy}$	43,7	$Kg.m^2$
$I_{zz}$	100,8	$Kg.m^2$
$I_{xy}$	0	$Kg.m^2$
$S$	1,965	$m^2$
$b$	5	$m$
$\bar{c}$	0.41	$m$
$\Lambda_f$	37	<i>degrees</i>
$\Lambda_a$	-37	<i>degrees</i>
$\Gamma_f$	6	<i>degrees</i>
$\Gamma_a$	-8	<i>degrees</i>
$\theta_f$	9,6	<i>degrees</i>
$\theta_a$	-3,4	<i>degrees</i>
$\lambda_f$	0,71	–
$\lambda_a$	1	–

Table B.1 - SensorCraft characteristics and geometry parameters

From table B.1,  $m$  is the aircraft mass,  $I_{xx}$ ,  $I_{yy}$  and  $I_{zz}$  represent the aircraft moment of inertia and  $I_{xy}$  the product of inertia,  $S$  is the reference area of both forward and aft wings,  $b$  is the aircraft wingspan and  $\bar{c}$  is the reference chord defined as the forward wing mean chord.

The parameters  $\Lambda_f$  and  $\Lambda_a$  denote the sweep angle of forward and aft wing respectively,  $\Gamma_f$  and  $\Gamma_a$  represent the forward and aft wing dihedral angles respectively. The parameters  $\theta_f$  and  $\theta_a$  represent the forward and aft wing twist angles respectively,  $\lambda_f$  and  $\lambda_a$  are the wing taper ratio of forward and aft wing respectively.

The position of the center of gravity is defined in the axis system presented in figure 1.1:

<i>Properties</i>	<i>Value</i>	<i>Unit</i>
$cg_x$	1,195	$m$
$cg_y$	0	$m$
$cg_z$	0,1704	$m$

Table B.2 - cg position

where  $cg_x$  is the distance of the  $cg$  from the  $YZ$ -plane,  $cg_y$  is the distance of  $cg$  the from the  $XZ$ -plane and  $cg_z$  is the distance of the  $cg$  from the  $XY$ -plane.

## Appendix C – Longitudinal equations transformation

Consider the equations written below:

$$\dot{u} = X_u u + X_w w - (g \cos \gamma_0) \theta + X_{\delta_s} \delta_s, \quad (C.1)$$

$$\dot{w} = Z_u u + Z_w w + (Z_q + U_0) q - (g \sin \gamma_0) \theta + Z_{\delta_s} \delta_s, \quad (C.2)$$

$$\dot{q} = M_u u + M_w w + M_{\dot{w}} \dot{w} + M_q q + M_{\delta_s} \delta_s, \quad (C.3)$$

$$\dot{\theta} = q, \quad (C.4)$$

The transformation applied is to substitute the  $\dot{w}$  equation (C.2) into the  $\dot{q}$  equation (C.3), thus becoming:

$$\dot{q} = M_u u + M_w w + M_{\dot{w}} [Z_u u + Z_w w + (Z_q + U_0) q - (g \sin \Theta_0) \theta + Z_{\delta_s} \delta_s] + M_q q + M_{\delta_s} \delta_s, \quad (C.5)$$

and resulting in:

$$\begin{aligned} \dot{q} = & (M_u + M_{\dot{w}} Z_u) u + (M_w + M_{\dot{w}} Z_w) w + (M_q + M_{\dot{w}} (Z_q + U_0)) q - (g M_{\dot{w}} \sin \Theta_0) \theta \\ & + (M_{\delta_s} + M_{\dot{w}} Z_{\delta_s}) \delta_s. \end{aligned} \quad (C.6)$$

To simplify the notation, the tilde notation is used:

$$\tilde{M}_u = (M_u + M_{\dot{w}} Z_u), \quad (C.7)$$

$$\tilde{M}_w = (M_w + M_{\dot{w}} Z_w), \quad (C.8)$$

$$\tilde{M}_q = [M_q + M_{\dot{w}} (Z_q + U_0)], \quad (C.9)$$

$$\tilde{M}_\theta = -(g M_{\dot{w}} \sin \Theta_0), \quad (C.10)$$

$$\tilde{M}_{\delta_s} = (M_{\delta_s} + M_{\dot{w}} Z_{\delta_s}). \quad (C.11)$$

## Appendix D – Sideslip velocity into sideslip angle

The transformation of sideslip velocity into sideslip angle only affects the equations (2.67 – 2.69). They are represented by:

$$\dot{v} = Y_v v + (Y_p + W_0)p + (Y_r - U_0)r + (g \cos \Theta_0) \phi + Y_{\delta_s} \delta_s, \quad (\text{D.1})$$

$$\dot{p} = L_v v + L_p p + L_r r + L_{\delta_s} \delta_s, \quad (\text{D.2})$$

$$\dot{r} = N_v v + N_p p + N_r r + N_{\delta_s} \delta_s. \quad (\text{D.3})$$

The relation between the sideslip velocity,  $v$ , and the sideslip angle,  $\beta$ , is given by:

$$v = U_0 \sin \beta. \quad (\text{D.4})$$

For small angles, the next approximation can be considered:

$$v = U_0 \beta \quad \Rightarrow \quad \dot{v} = U_0 \dot{\beta}. \quad (\text{D.5})$$

Substituting these relations into the equations of lateral motion, we have:

$$U_0 \dot{\beta} = Y_v U_0 \beta + (Y_p + W_0)p + (Y_r - U_0)r + (g \cos \Theta_0) \phi + Y_{\delta_s} \delta_s, \quad (\text{D.6})$$

$$\dot{p} = L_v U_0 \beta + L_p p + L_r r + L_{\delta_s} \delta_s, \quad (\text{D.7})$$

$$\dot{r} = N_v U_0 \beta + N_p p + N_r r + N_{\delta_s} \delta_s. \quad (\text{D.8})$$

Simplifying, it is possible to obtain:

$$\dot{\beta} = Y_v \beta + \left( \frac{Y_p}{U_0} + \frac{W_0}{U_0} \right) p + \left( \frac{Y_r}{U_0} - \frac{U_0}{U_0} \right) r + \left( \frac{g}{U_0} \cos \Theta_0 \right) \phi + \frac{Y_{\delta_s}}{U_0} \delta_s, \quad (\text{D.9})$$

$$\dot{p} = L_v U_0 \beta + L_p p + L_r r + L_{\delta_s} \delta_s, \quad (\text{D.10})$$

$$\dot{r} = N_v U_0 \beta + N_p p + N_r r + N_{\delta_s} \delta_s, \quad (\text{D.11})$$

and using the follow relations:

$$Y_v = Y_\beta, \quad (\text{D.12})$$

$$L_\beta = L_v U_0, \quad (\text{D.13})$$

$$N_\beta = N_v U_0, \quad (\text{D.14})$$

we get:

$$\frac{W_0}{U_0} = \frac{V_T \cos \beta_0 \sin \alpha_0}{V_T \cos \beta_0 \cos \alpha_0} = \frac{\sin \alpha_0}{\cos \alpha_0} = \tan \alpha_0. \quad (\text{D.15})$$

For small angles,

$$\tan \alpha_0 \cong \alpha_0, \quad (\text{D.16})$$

the expressions take the form:

$$\dot{\beta} = Y_{\beta} \beta + \left(\frac{Y_p}{U_0} + \alpha_0\right) p + \left(\frac{Y_r}{U_0} - 1\right) r + \left(\frac{g}{U_0} \cos \Theta_0\right) \phi + \frac{Y_{\delta_s}}{U_0} \delta_s, \quad (\text{D.17})$$

$$\dot{p} = L_{\beta} \beta + L_p p + L_r r + L_{\delta_s} \delta_s, \quad (\text{D.18})$$

$$\dot{r} = N_{\beta} \beta + N_p p + N_r r + N_{\delta_s} \delta_s. \quad (\text{D.19})$$

## Appendix E - Some AVL data insight calculation

For more precise results, some aerodynamic parameters were calculated for the aircraft airfoils. These parameters were:

### ➤ Lift curve slope of the airfoil $dC_l/d\alpha$

The lift curve slope of each airfoil was calculated using a good estimate for  $C_{l_{\alpha}}$  from 2D potential flow theory (accordingly with AVL documentation):

$$C_{l_{\alpha}} = 2\pi C_{l_{cf}}, \quad (\text{E.1})$$

where,

$$C_{l_{cf}} = 1 + 0.77 \frac{t}{c}, \quad (\text{E.2})$$

and,  $\frac{t}{c}$  is the ratio between the maximum thickness value and the chord of the airfoil.

### ➤ 3 points of the Drag-Polar curve: $C_l$ vs $C_d$

The Drag-Polar curve was determined using the program *JavaFoil* to find the relation  $C_l$  vs  $C_d$  of each airfoil. From the Drag-Polar curve three points are selected to be used in AVL code through a parabolic interpolation. These three points are selected as figure E.1 shows coloured in purple.

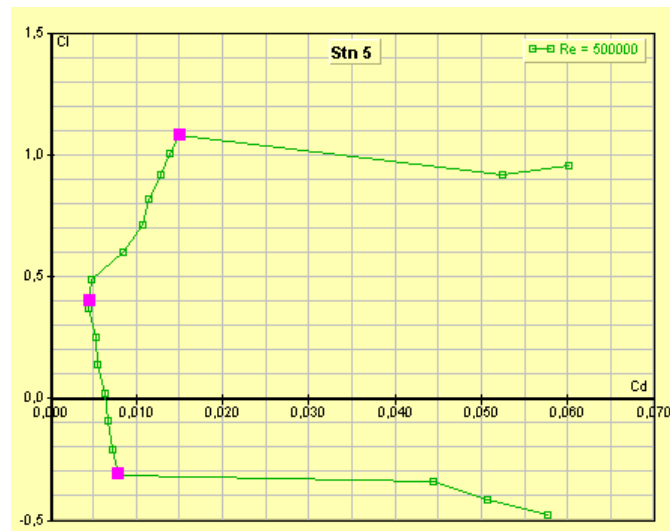


Figure E.1 - Drag-Polar points selection from *JavaFoil* program

## Appendix F – Stability coefficients of SensorCraft

The stability coefficients determined with *AVL* program are presented in figure F.1.

alpha		beta	
-----		-----	
CLa = 11.055526	CLb = -0.000004		
CYa = 0.000028	CYb = -0.510408		
Cl a = 0.000004	Cl b = -0.305695		
Cma = -1.658976	Cmb = 0.000002		
Cna = -0.000021	Cnb = 0.013697		
axial vel. u	sideslip vel. v	normal vel. w	
-----	-----	-----	
CXu = -0.066819	CXv = 0.000009	CXw = 1.010724	
CYu = 0.000005	CYv = -0.510408	CYw = 0.000028	
CZu = -1.861883	CZv = 0.000005	CZw = -11.148037	
Clu = 0.000001	Clv = -0.305990	Clw = 0.000007	
Cmu = 0.406555	Cmv = 0.000002	Cmw = -1.645416	
Cnu = -0.000003	Cnv = 0.002691	Cnw = -0.000020	
roll rate p	pitch rate q	yaw rate r	
-----	-----	-----	
CXp = 0.000025	CXq = -0.317727	CXr = -0.000006	
CYp = 0.193098	CYq = 0.000021	CYr = 0.208067	
CZp = 0.000009	CZq = -26.183298	CZr = -0.000002	
Clp = -0.987337	Clq = -0.000004	Clr = 0.205652	
Cmp = -0.000010	Cmq = -78.802109	Cmd = -0.000001	
Cnp = -0.160249	Cnq = -0.000016	Cnr = -0.033343	
RFlaps d1	LFlaps d2	RAilerInboar d3	LAilerInboar d4
-----	-----	-----	-----
CXd1 = -0.000200	CXd2 = -0.000200	CXd3 = 0.000011	CXd4 = 0.000011
CYd1 = -0.001039	CYd2 = 0.001039	CYd3 = -0.000709	CYd4 = 0.000709
CZd1 = -0.007447	CZd2 = -0.007447	CZd3 = -0.004634	CZd4 = -0.004634
Cl d1 = -0.001299	Cl d2 = 0.001299	Cl d3 = -0.001299	Cl d4 = 0.001299
Cmd1 = 0.006666	Cmd2 = 0.006666	Cmd3 = -0.001709	Cmd4 = -0.001709
Cnd1 = 0.000022	Cnd2 = -0.000022	Cnd3 = 0.000031	Cnd4 = -0.000031
RAilerOutboa d5	LAilerOutboa d6	RElevInboard d7	RElevOutboar d8
-----	-----	-----	-----
CXd5 = 0.000145	CXd6 = 0.000145	CXd7 = 0.000066	CXd8 = -0.000031
CYd5 = -0.000350	CYd6 = 0.000350	CYd7 = 0.000558	CYd8 = 0.000663
CZd5 = -0.005355	CZd6 = -0.005355	CZd7 = -0.005761	CZd8 = -0.005643
Cl d5 = -0.001983	Cl d6 = 0.001983	Cl d7 = -0.000483	Cl d8 = -0.001117
Cmd5 = -0.007931	Cmd6 = -0.007931	Cmd7 = -0.019248	Cmd8 = -0.012766
Cnd5 = -0.000025	Cnd6 = 0.000025	Cnd7 = -0.000165	Cnd8 = -0.000124
LElevOutboar d9	LElevInboard d10		
-----	-----		
CXd9 = -0.000031	CXd10 = 0.000066		
CYd9 = -0.000663	CYd10 = -0.000558		
CZd9 = -0.005643	CZd10 = -0.005761		
Cl d9 = 0.001117	Cl d10 = 0.000483		
Cmd9 = -0.012766	Cmd10 = -0.019248		
Cnd9 = 0.000124	Cnd10 = 0.000165		

Figure F.1 - *AVL* stability coefficients results

## Appendix G – Results of *MATLAB*® dynamic stability

```
>> [freq_lon, damp_lon, poles_lon] = damp(A_lon)

freq_lon =

    0.49762405946807
    0.49762405946807
    5.41358087730200
    5.41358087730200

damp_lon =

   -0.02263857731114
   -0.02263857731114
    0.78321640094906
    0.78321640094906

poles_lon =

    0.01126550074215 + 0.49749652567079i
    0.01126550074215 - 0.49749652567079i
   -4.24000533096713 + 3.36588958649273i
   -4.24000533096713 - 3.36588958649273i
```

Figure G.1 – Longitudinal natural frequency, damping ratio and eigenvalues

```
>> [freq_lat, damp_lat, poles_lat] = damp(A_lat)

freq_lat =

           0
    0.00994316196819
    1.92586929919289
    1.92586929919289
    6.34455237611642

damp_lat =

   -1.00000000000000
    1.00000000000000
    0.04695663478028
    0.04695663478028
    1.00000000000000

poles_lat =

           0
   -0.00994316196819
   -0.09043234131676 + 1.92374492831500i
   -0.09043234131676 - 1.92374492831500i
   -6.34455237611642
```

Figure G.2 – Lateral natural frequency, damping ratio and eigenvalues

## Appendix H – Stability coefficient $C_{m\dot{\alpha}}$ estimation

Using reference [16] the following formula was applied:

$$C_{m\dot{\alpha}} = -2C_{L\alpha_h} \eta_h \bar{V}_h (\bar{x}_{ac_h} - \bar{x}_{cg}) \frac{d\epsilon}{d\alpha}, \quad (\text{H.1})$$

where:

- $C_{L\alpha_h}$  is the horizontal tail lift curve slope
- $\eta_h$  is dynamic pressure ratio between the horizontal tail and the free stream dynamic pressures:  $\eta_h = \frac{\bar{q}_h}{\bar{q}}$
- $\bar{V}_h$  is the horizontal tail volume coefficient
- $\bar{x}_{ac_h}$  and  $\bar{x}_{cg}$  are geometric distances in the aircraft between wing and horizontal tail, and between wing and center of gravity respectively
- $\frac{d\epsilon}{d\alpha}$  is the downwash gradient at the horizontal tail

These properties were obtained using other estimating formulas and graphics resources following the indications in reference [16].

The values achieved in each property are shown in the table H.1.

Properties	$C_{L\alpha_h}$ [1/rad]	$\eta_h$	$\bar{V}_h$	$(\bar{x}_{ac_h} - \bar{x}_{cg})$	$d\epsilon/d\alpha$
Value	4,01	0,96	0,63	2,05	0,24

Table H.1 - Estimated values

## Appendix I – Longitudinal and Lateral Modes

The representative pictures of each longitudinal and lateral mode are shown below.

### Short period mode

The development of a stable short period mode is presented below in figure I.1.

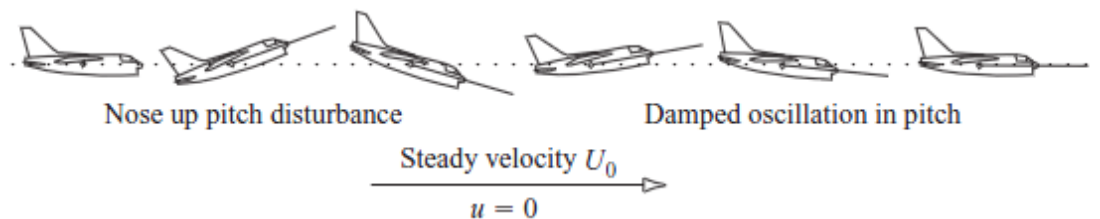


Figure I.1 - Stable short period mode [19]

*Phugoid mode*

The figure I.2 represents a stable oscillation of the phugoid mode.



Figure I.2 - Stable phugoid mode [19]

*Spiral mode*

The spiral mode development for a sideslip disturbance is presented in following figure:

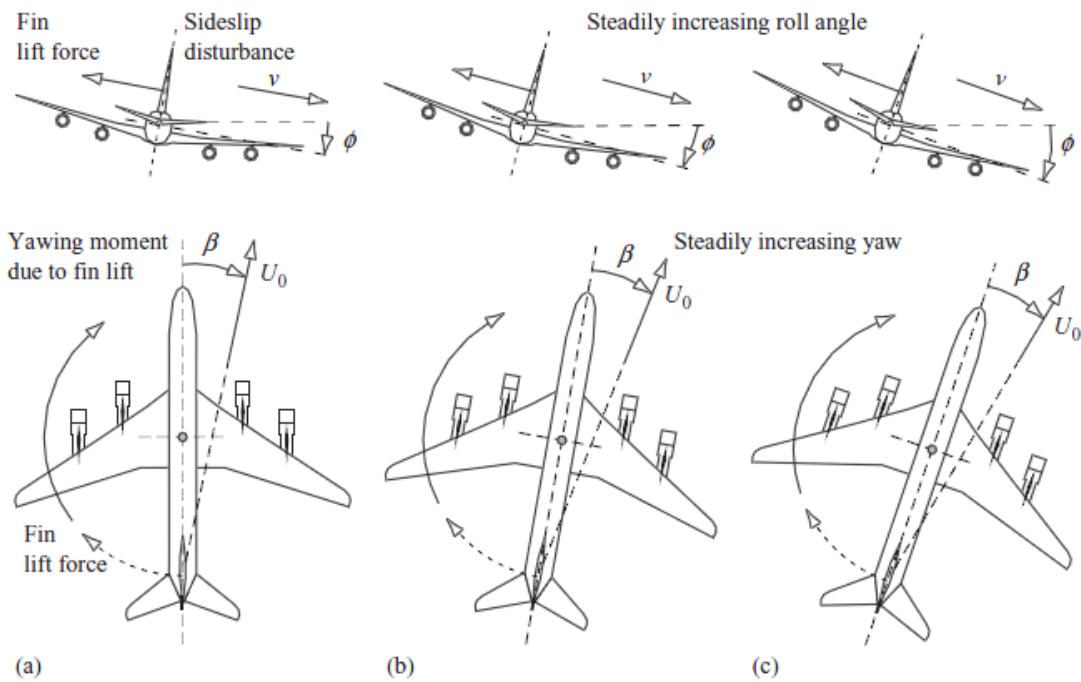


Figure I.3 - Spiral mode [19]

*Dutch roll mode*

Representative process of the dutch roll mode and its explanation is given in the figure I.4.

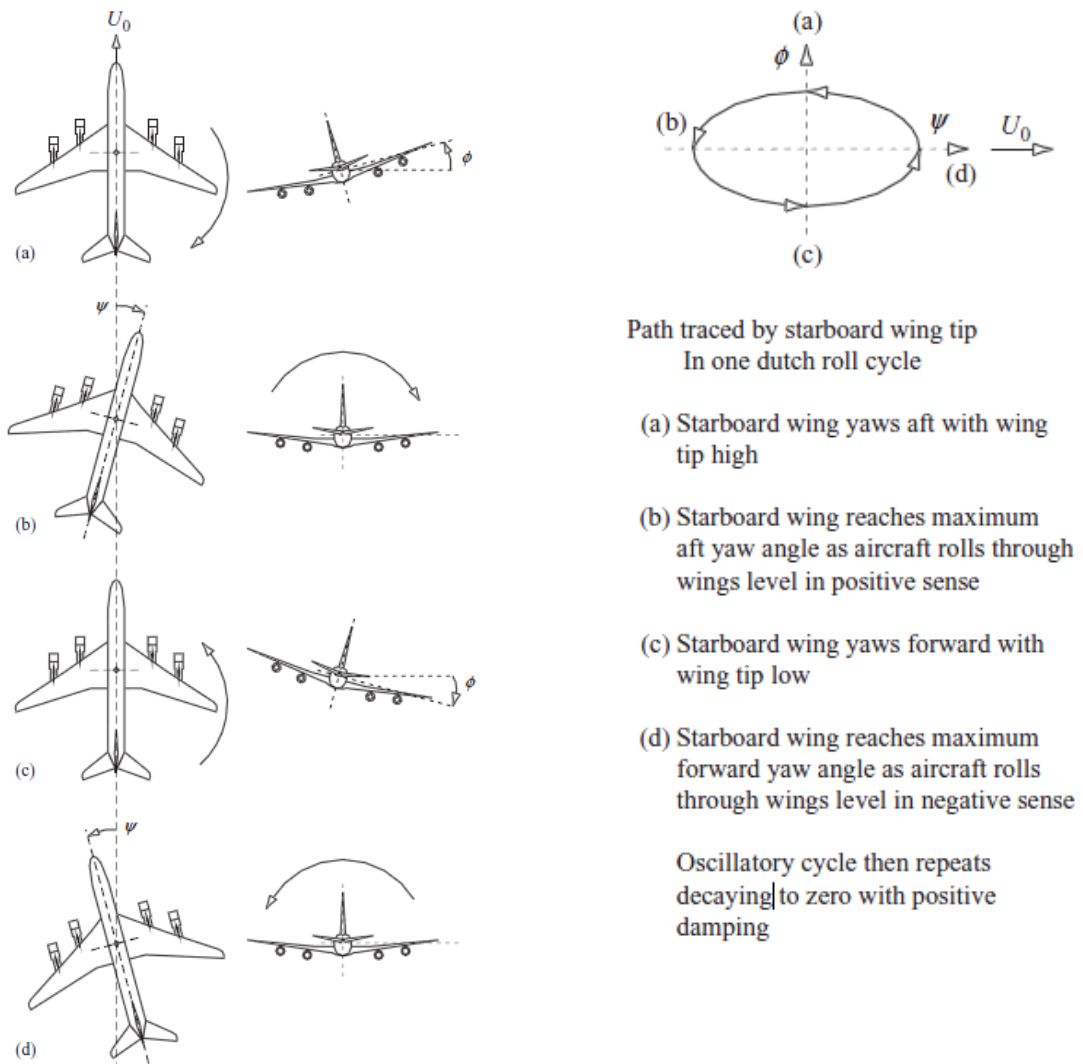


Figure I.4 - Dutch roll mode explanation [19]

*Roll mode*

The figure I.5 represents the explanation of the roll mode and the appearance of its restoring rolling moment.

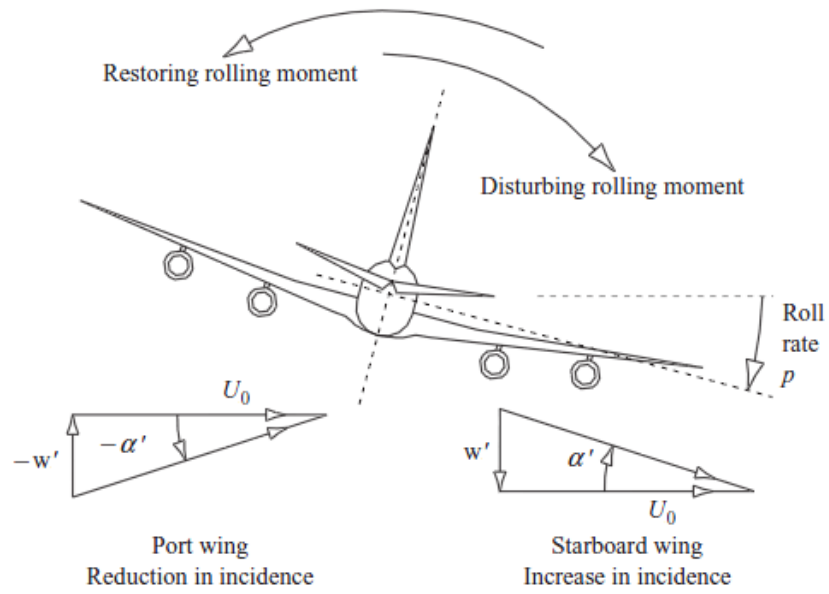


Figure I.5 - Roll mode [19]

## Appendix J – Flying qualities

### J.1 Aircraft Classification

The aircraft is considered to belong to one of the four classes shown in table J.1 according with reference [12].

<b>Class</b>	<b>Aircraft characteristics</b>
<i>I</i>	<i>Small, light aircraft (max. weight = 5.000 Kg)</i>
<i>II</i>	<i>Aircraft of medium weight (weight between 5000 and 30.000 Kg)</i>
<i>III</i>	<i>Large, heavy aircraft with moderate maneuverability (30.000 + Kg)</i>
<i>IV</i>	<i>Aircraft with high maneuverability</i>

Table J.1 - Aircraft classification

The mission of an aircraft is characterized in three phases of flight as shown in table J.2 according with the reference [12].

<b>Phase</b>	<b>Description</b>
<i>A</i>	<i>Non – terminal phase of flight such as those involving rapid maneuvering and precise control of the flight path</i>
<i>B</i>	<i>Non – terminal phase of flight accomplished by gradual maneuvers which do not require precise tracking or control of the flight path</i>
<i>C</i>	<i>Terminal flight phase, accomplished by gradual maneuvers, but requiring accurate flight path control</i>

Table J.2 - Aircraft flight phases

The capability of an aircraft to complete the mission for which was designated will be characterized in three distinct levels. Each level is a limiting condition for the flight quality evaluation parameters.

The levels are described in table J.3 according with reference [12].

<b>Level</b>	<b>Definition</b>
<i>1</i>	<i>The flying qualities are completely adequate for the particular flight phase</i>
<i>2</i>	<i>The flying qualities are adequate for the particular phase, but there is either some loss in the effectiveness of mission, or an increase of workload upon the pilot to achieve the mission, or both</i>
<i>3</i>	<i>The flying qualities are such that the aircraft can be controlled, but either the effectiveness of the mission is gravely affected or the workload imposed upon the pilot to accomplish the mission is so great that it can approaches the limit of his capacity</i>

Table J.3 - Aircraft quality flight levels

## J.2 Longitudinal flying qualities

### *Short period response*

The longitudinal short period mode flying quality levels are defined by limit conditions for the short period damping ratio  $\xi_{sp}$ . The values of the damping ratio specifications are presented in table J.4.

<b>Flight phase category</b>	<b>Level 1</b>		<b>Level 2</b>		<b>Level 3</b>	
	<i>Min.</i>	<i>Max.</i>	<i>Min.</i>	<i>Max.</i>	<i>Min.</i>	<i>Max.</i>
<i>A</i>	0,35	1,3	0,25	2	0,1	-
<i>B</i>	0,3	2	0,2	2	0,1	-
<i>C</i>	0,35	1,3	0,35	2	0,25	-

**Table J.4 - Short period mode damping ratio specification**

### *Phugoid response*

The phugoid mode flying quality levels are characterized by imposing limits in the phugoid damping ratio  $\xi_{ph}$  as well as in the *period*  $P$ , for the undamped oscillatory mode. These specifications are presented in table J.5.

<b>Level</b>	<b><math>\xi_{ph}</math></b>
1	$\geq 0,04$
2	$\geq 0,0$
3	<i>Period of at least 55 s</i>

**Table J.5 - Phugoid mode flying qualities**

If the real part of the eigenvalue is positive,  $> 0$ , the resultant undamped oscillatory mode is analyzed using a minimum required value for the phugoid *period* and it is defined as:

$$P = \frac{2\pi}{\omega_n}. \quad (\text{J.1})$$

Besides the requisites in the damping ratio for both short period and phugoid, good flying qualities are only achieved if the aircraft has a good separation of the longitudinal modes frequency. Therefore, short period frequency and phugoid frequency must be widely separated in order to accomplish good longitudinal qualities as shown below:

$$\frac{\omega_{ph}}{\omega_{sp}} < 0,1. \quad (\text{J.2})$$

## J.3 Lateral flying qualities

### *Spiral*

The spiral mode flying quality levels are defined using the time for the bank angle to double after a disturbance for unstable eigenvalues (positive value). Therefore if the spiral eigenvalue is negative the spiral mode is automatically assumed to be *level 1* quality.

The time to double  $T_2$  of spiral is determined using the eigenvalue as shown in equation (J.3). The table J.6 shows the specifications for the spiral mode quality levels.

$$T_2 = \frac{\ln(2)}{\sigma}. \quad (J.3)$$

<b>Flight phase category</b>	<b><math>T_2</math></b>		
	<b>Level 1</b>	<b>Level 2</b>	<b>Level 3</b>
<i>A and C</i>	$\geq 12$ s	$\geq 8$ s	$\geq 5$ s
<i>B</i>	$\geq 20$ s	$\geq 8$ s	$\geq 5$ s

Table J.6 - Spiral mode levels specification

### Dutch roll

The dutch roll parameters which will define the flying quality levels are the damping ratio,  $\xi_D$ , and the dutch roll frequency,  $\omega_D$ . The specifications for dutch roll parameters are shown in table J.7 representing the minimum values allowed for each level.

<b>Flight phase category</b>	<b>Class</b>	<b>Level 1</b>			<b>Level 2</b>			<b>Level 3</b>		
		$\xi_D$	$\xi_D \omega_D$	$\omega_D$	$\xi_D$	$\xi_D \omega_D$	$\omega_D$	$\xi_D$	$\xi_D \omega_D$	$\omega_D$
<i>A</i>	<i>I, IV</i>	0,19	0,35	1	0,02	0,05	0,5	0	-	0,4
<i>A</i>	<i>II, III</i>	0,19	0,35	0,5	0,02	0,05	0,5	0	-	0,4
<i>B</i>	<i>All</i>	0,08	0,15	0,5	0,02	0,05	0,5	0	-	0,4
<i>C</i>	<i>I, IV</i>	0,08	0,15	1	0,02	0,05	0,5	0	-	0,4
<i>C</i>	<i>II, III</i>	0,08	0,1	0,5	0,02	0,05	0,5	0	-	0,4

Table J.7 - Dutch roll mode levels specification

### Roll

The specification that characterizes the roll mode flying quality levels is given by the time constant  $T_R$ , and it is required to be less than the specific maximum values shown in table J.8. The time constant of the roll mode is defined as equation (J.4).

$$T_R = \frac{1}{|\sigma|}. \quad (J.4)$$

<b>Flight phase category</b>	<b>Class</b>	<b><math>T_R</math></b>		
		<b>Level 1</b>	<b>Level 2</b>	<b>Level 3</b>
<i>A</i>	<i>I, IV</i>	1,0 s	1,4 s	10 s
<i>A</i>	<i>II, III</i>	1,4 s	3,0 s	10 s
<i>B</i>	<i>All</i>	1,4 s	3,0 s	10 s
<i>C</i>	<i>I, IV</i>	1,0 s	1,4 s	10 s
<i>C</i>	<i>II, III</i>	1,4 s	3,0 s	10 s

Table J.8 - Roll mode time constant specification

## Appendix K – *MATLAB*® code

```

%-----%
% Stability and Control %
%-----%
% Constants %
deg = pi/180; % Convert to [rad] units %
rad = 180/pi; % Unit convert in order to pass [1/degrees] to [1/rad] %
aa0 = 4.5; % angle in degrees %
gg0 = 0; % reference gama angle %
tt0 = gg0+aa0; % reference angle gama plus reference angle of attack equals reference teta angle %
u0 = 25.9*cos(aa0*deg); % [m/s] %
v0 = 0; % [m/s] %
w0 = u0*sin(aa0*deg); % [m/s] %
g = 9.814; % [m/s^2] %
ro = 1.225; % demsity of the atmosphere [Kg/m^3] %
lxx = 61.5; % [Kg.m^2] %
lyy = 43.7; % [Kg.m^2] %
lzz = 100.8; % [Kg.m^2] %
lxz = 0; % [Kg.m^2] %
h = 100; % [m] %
lp = lxx/lzz;
lr = lxx/lzz;
S = 1.965; % Wing Surface [m^2] %
b = 5; % Wing Span [m] %
c = 0.41; % Wing Chord [m] %
m = 93; % Mass [Kg] %
cg_x = 1.195; % Gravity center xx %
cg_y = 0; % Gravity center yy %
cg_z = 0.1704; % Gravity center zz %
%-----%
% Longitudinal Motion %
%-----%
% Non-Dimensional Stability Derivatives %
CXu = -0.066819;
CXw = 1.010724;
CXaa = CXw/u0;
CXq = -0.317727;
CZu = -1.861883;
CZw = -11.148037;
CZwp = 0;
CZq = -26.183298;
CZaap = 0;
Cmu = 0.406555;
Cmaa = -1.658976;
Cmq = -78.802109;
Cmwp = 0;
Cmaap = -2.4;
% mutiplied by 'rad' constant in order to get the conventional units [1/rad] %
CXde = 2*(0.000066)*rad; % Inboard Elevator %
CZde = 2*(-0.005761)*rad;
Cmde = 2*(-0.019248)*rad;
% CXde = 2*(0.000066-0.000031)*rad; % Inboard Elevator + Outboard Elevator %

```

```

% CZde = 2*(-0.005761-0.005643)*rad;
% Cmde = 2*(-0.019248-0.012766)*rad;
% CXde = 2*(-0.000031)*rad; % Outboard Elevator %
% CZde = 2*(-0.005643)*rad;
% Cmde = 2*(-0.012766)*rad;
% CXde = 2*(-0.000200)*rad; % Flaps %
% CZde = 2*(-0.007447)*rad;
% Cmde = 2*(0.006666)*rad;
% Dimensional Stability Derivatives calculations %
Xu = CXu*ro*S*u0/(2*m);
Xw = CXaa*ro*S*u0/(2*m);
Xq = CXq*ro*S*u0*c/(4*m);
Zu = CZu*ro*S*u0/(2*m);
Zw = CZw*ro*S*u0/(2*m);
Zwp = CZaap*ro*S*u0*c/(4*m); % despresável %
Zq = CZq*ro*S*u0*c/(4*m);
Mu = Cmu*ro*S*u0*c/(2*Iyy);
Mw = Cmaa*ro*S*u0*c/(2*Iyy);
Mq = Cmqa*ro*S*u0*(c^2)/(4*Iyy);
Mwp = Cmaap*ro*S*(c^2)/(4*Iyy);
% Elevator %
Xde = -CXde*ro*S*(u0^2)/(2*m);
Zde = -CZde*ro*S*(u0^2)/(2*m);
Mde = Cmde*ro*S*(u0^2)*c/(2*Iyy);
%-----%
% Longitudinal Stability %
%-----%
% State coefficient matrix %
A_lon = [ Xu Xw 0 -g*cos(tt0*deg) ; Zu Zw u0+Zq -g*sin(tt0*deg) ;
          Mu+Mwp*Zu Mw+Mwp*Zw Mq+Mwp*u0 -Mwp*g*sin(tt0*deg) ; 0 0 1 0 ];
% Driving matrix %
B_lon = [ Xde; Zde; Mde+Mwp*Zde ; 0];
C_lon = [ 1 0 0 0 ; 0 1 0 0 ; 0 0 1 0 ; 0 0 0 1];
D_lon = [ 0 ; 0 ; 0 ; 0];
[ freq_lon, damp_lon, poles_lon ] = damp(A_lon); % Frequency, damping and poles position of A_lon %
% -- Root Locus -- %
[num1,den1] = ss2tf(A_lon,B_lon,[0 0 1 1],[0],1); % realimentação da velocidade vs de %
bode(num1,den1);
rlocus(-num1,den1);
rlocfind(num1,den1)
% K_lon = [ 0 0 -0.2 -0.2]; %to inboard + outboard elevators
K_lon = [ 0 0 -0.35 -0.35]; %to inboard elevators only
A_lonK = A_lon-B_lon*K_lon;
[ freq_lonK, damp_lonK, poles_lonK ] = damp(A_lonK);

%-----%
% Lateral Motion %
%-----%
% Non-Dimensional Stability Derivatives %
CYbb = -0.510408;
Clbb = -0.305695;
Cnbb = 0.013697;
CYp = 0.193098;
Clp = -0.987337;
Cnp = -0.160249;

```

```

CYr = 0.208067;
Clr = 0.205652;
Cnr = -0.033343;
% Mixed-control rudder equivalent surfaces %
% CYda1 = -0.144; % Configuration 1 %
% Clda1 = 0;
% Cnda1 = 0.021;
% CYda1 = -0.097; % Configuration 2 %
% Clda1 = 0;
% Cnda1 = 0.019;
% CYda1 = -0.093; % Configuration 3 %
% Clda1 = 0;
% Cnda1 = 0.022;
% CYda1 = -0.192; % Configuration 4 %
% Clda1 = 0;
% Cnda1 = 0.034;
% CYda1 = -0.171; % Configuration 5 %
% Clda1 = 0;
% Cnda1 = 0.04;
% CYda1 = -0.246; % Configuration 6 %
% Clda1 = 0;
% Cnda1 = 0.041;
% CYda1 = -0.133; % Configuration 7 %
% Clda1 = 0;
% Cnda1 = 0.045;
% Speed-brake control rudder equivalent surfaces %
CYda1 = -0.072; % Configuration 1 % max 20
Clda1 = 0;
Cnda1 = 0.055;
% CYda1 = -0.049; % Configuration 2 % max 20
% Clda1 = 0;
% Cnda1 = 0.053;
% CYda1 = -0.046; % Configuration 3 % max 15
% Clda1 = 0;
% Cnda1 = 0.035;
% CYda1 = -0.096; % Configuration 4 % max 20
% Clda1 = 0;
% Cnda1 = 0.0725;
% CYda1 = -0.085; % Configuration 5 % max 20
% Clda1 = 0;
% Cnda1 = 0.087;
% CYda1 = -0.123; % Configuration 6 % max 20
% Clda1 = 0;
% Cnda1 = 0.089;
% CYda1 = -0.067; % Configuration 7 % max 20
% Clda1 = 0;
% Cnda1 = 0.115;
% Dimensional Stability Derivatives %
% Lateral - Aircraft %
Ybb = CYbb*ro*S*u0/(2*m);
Lbb = Clbb*ro*S*(u0^2)*b/(2*Ixx);
Nbb = Cnbb*ro*S*(u0^2)*b/(2*Izz);
Yp = CYp*ro*S*u0*b/(4*m);
Lp = Clp*ro*S*u0*(b^2)/(4*Ixx);
Np = Cnp*ro*S*u0*(b^2)/(4*Izz);

```

```

Yr = CYr*ro*S*u0*b/(4*m);
Lr = Clr*ro*S*u0*(b^2)/(4*Ixx);
Nr = Cnr*ro*S*u0*(b^2)/(4*Izz);
% Control Surface 1 %
Yda1 = CYda1*ro*S*(u0^2)/(2*m);
Lda1 = Clda1*ro*S*(u0^2)*b/(2*Ixx);
Nda1 = Cnda1*ro*S*(u0^2)*b/(2*Izz);
% Control Surface 2 %
Yda2 = CYda2*ro*S*(u0^2)/(2*m);
Lda2 = Clda2*ro*S*(u0^2)*b/(2*Ixx);
Nda2 = Cnda2*ro*S*(u0^2)*b/(2*Izz);
%-----%
% Lateral Stability %
%-----%
% State coefficient matrix %
A_lat = [ Ybb Yp/u0+aa0*deg Yr/u0-1 g*cos(tt0*deg)/u0 0 0 ; Lbb+Ip*Nbb Lp+Ip*Np Lr+Ip*Nr 0 0 ;
          Nbb+Ir*Lbb Np+Ir*Lp Nr+Ir*Lr 0 0 ; 0 1 tan(tt0*deg) 0 0 ; 0 0 1/cos(tt0*deg) 0 0 ];
% Driving matrix %
B_lat = [ Yda1/u0 Yda2/u0 ; Lda1+Ip*Nda1 Lda2+Ip*Nda2 ; Nda1+Ir*Lda1 Nda2+Ir*Lda2 ; 0 0 ; 0 0 ];
C = [ 1 0 0 0 0 ; 0 1 0 0 0 ; 0 0 1 0 0 ; 0 0 0 1 0 ; 0 0 0 0 1 ];
D = [ 0 0 ; 0 0 ; 0 0 ; 0 0 ];
% --Root Locus-- %
[num1,den1] = ss2tf(A_lat,B_lat1,[0 0 1 0 0],[0 0 0 0 0],1); % realimentação da razão de guinada vs da1
bode(num1,den1);
rlocus(num1,den1);
rlocfind(num,den)
A_latr = A_lat-B_lat*K;
[freq_latr, damp_latr, poles_latr] = damp(A_latr);
% -----%
% --- LQR with integrative state of 'fi' and 'psi' --- %
A_lati2 = [ Ybb Yp/u0+aa0*deg Yr/u0-1 g*cos(tt0*deg)/u0 0 0 0 ; Lbb+Ip*Nbb Lp+Ip*Np Lr+Ip*Nr 0 0 0 0 ;
            Nbb+Ir*Lbb Np+Ir*Lp Nr+Ir*Lr 0 0 0 0 ; 0 1 tan(tt0*deg) 0 0 0 0 ; 0 0 1/cos(tt0*deg) 0 0 0 0 ;
            0 0 0 1 0 0 0 ; 0 0 0 0 1 0 0 ];
% Driving matrix %
B_lati2 = [ Yda1/u0 Yda2/u0 ; Lda1+Ip*Nda1 Lda2+Ip*Nda2 ; Nda1+Ir*Lda1 Nda2+Ir*Lda2 ; 0 0 ; 0 0 ; 0 0 ; 0 0 ];
Qi2 = diag([1000 1 30 10 40 3 5]);
Ri2 = diag([10 10]);
Ki2 = lqr(A_lati2,B_lati2,Qi2,Ri2);
damp(A_lati2-B_lati2*Ki2);

```

## Appendix L – SensorCraft airfoil coordinates data

The airfoil coordinate data of each numbered section defined in figure 3.1, provided by USAF partners, are presented below:

<u>Section 1</u>		<u>Section 2</u>		<u>Section 3</u>		<u>Section 4</u>	
1.000000	0.000000	1.000000	0.000000	1.000000	0.000000	1.000000	0.000000
0.962600	0.014700	0.962600	0.014700	0.961500	0.005000	0.961600	0.006700
0.924700	0.028300	0.924700	0.028300	0.922900	0.009400	0.923100	0.012600
0.886500	0.040800	0.886500	0.040800	0.884200	0.013100	0.884400	0.017700
0.848000	0.052200	0.848000	0.052200	0.845500	0.016400	0.845700	0.022000
0.809100	0.062400	0.809100	0.062400	0.806800	0.019300	0.806900	0.025700
0.769900	0.071500	0.769900	0.071500	0.768100	0.022000	0.768100	0.028900
0.730500	0.079400	0.730500	0.079400	0.729300	0.024400	0.729200	0.031800
0.690800	0.086000	0.690800	0.086000	0.690500	0.026700	0.690300	0.034600
0.651000	0.091300	0.651000	0.091300	0.651700	0.028800	0.651400	0.037100
0.611000	0.095300	0.611000	0.095300	0.612900	0.030800	0.612500	0.039400
0.570800	0.098000	0.570800	0.098000	0.574100	0.032700	0.573600	0.041300
0.530600	0.099200	0.530600	0.099200	0.535300	0.034400	0.534600	0.043000
0.490400	0.099400	0.490400	0.099400	0.496500	0.035900	0.495700	0.044400
0.450200	0.099700	0.450200	0.099700	0.457700	0.037200	0.456700	0.045400
0.410000	0.099900	0.410000	0.099900	0.418900	0.038200	0.417800	0.046200
0.369800	0.100200	0.369800	0.100200	0.380000	0.038900	0.378800	0.046600
0.329600	0.100400	0.329600	0.100400	0.341200	0.039300	0.339800	0.046600
0.289400	0.100600	0.289400	0.100600	0.302400	0.039300	0.300800	0.046200
0.249200	0.100100	0.249200	0.100100	0.263500	0.038800	0.261900	0.045200
0.209000	0.098600	0.209000	0.098600	0.224700	0.037800	0.222900	0.043700
0.168900	0.095400	0.168900	0.095400	0.185900	0.036200	0.184000	0.041400
0.129300	0.088900	0.129300	0.088900	0.147100	0.033900	0.145200	0.038400
0.091100	0.076400	0.091100	0.076400	0.108400	0.030700	0.106400	0.034400
0.056400	0.056300	0.056400	0.056300	0.069800	0.026100	0.067800	0.029000
0.025800	0.030200	0.025800	0.030200	0.031700	0.018800	0.029700	0.021100
0.012200	0.016500	0.012200	0.016500	0.014100	0.013000	0.012000	0.015000
0.005200	0.008800	0.005200	0.008800	0.005300	0.008100	0.003800	0.009200
0.000000	0.000000	0.000000	0.000000	0.000000	0.000000	0.000000	0.000000
0.002600	-0.009800	0.002600	-0.009800	0.006200	-0.007500	0.005000	-0.008300
0.009500	-0.017500	0.009500	-0.017500	0.015200	-0.011900	0.014100	-0.012500
0.025600	-0.027700	0.025600	-0.027700	0.032800	-0.018100	0.032200	-0.017000
0.062000	-0.043600	0.062000	-0.043600	0.070500	-0.028100	0.070400	-0.023600
0.100200	-0.055100	0.100200	-0.055100	0.108500	-0.036400	0.109000	-0.027500
0.139100	-0.063800	0.139100	-0.063800	0.146800	-0.043100	0.147700	-0.028800
0.178600	-0.068600	0.178600	-0.068600	0.185500	-0.048100	0.186500	-0.028400
0.218400	-0.069700	0.218400	-0.069700	0.224200	-0.051700	0.225300	-0.027400
0.258200	-0.070000	0.258200	-0.070000	0.263100	-0.054100	0.264100	-0.026300
0.298100	-0.070200	0.298100	-0.070200	0.302000	-0.055600	0.302900	-0.025200
0.337900	-0.070500	0.337900	-0.070500	0.341000	-0.056000	0.341600	-0.023900
0.377800	-0.070700	0.377800	-0.070700	0.379900	-0.055600	0.380400	-0.022500
0.417600	-0.071000	0.417600	-0.071000	0.418800	-0.054400	0.419200	-0.020900
0.457400	-0.071300	0.457400	-0.071300	0.457700	-0.052300	0.457900	-0.019100
0.497300	-0.071500	0.497300	-0.071500	0.496600	-0.049600	0.496600	-0.017000
0.537100	-0.071800	0.537100	-0.071800	0.535400	-0.046200	0.535400	-0.014800
0.577000	-0.072000	0.577000	-0.072000	0.574100	-0.042300	0.574100	-0.012300
0.616800	-0.072300	0.616800	-0.072300	0.612800	-0.038000	0.612800	-0.009700
0.656600	-0.072500	0.656600	-0.072500	0.651400	-0.033300	0.651500	-0.006700
0.696500	-0.072800	0.696500	-0.072800	0.690100	-0.028300	0.690100	-0.003500
0.736300	-0.073000	0.736300	-0.073000	0.728700	-0.023100	0.728800	-0.000100
0.776200	-0.073200	0.776200	-0.073200	0.767200	-0.017900	0.767400	0.002800
0.815900	-0.070800	0.815900	-0.070800	0.805900	-0.012900	0.806200	0.004800
0.855200	-0.064200	0.855200	-0.064200	0.844600	-0.008500	0.845000	0.005500
0.893500	-0.053500	0.893500	-0.053500	0.883300	-0.004700	0.883800	0.005200
0.930600	-0.039000	0.930600	-0.039000	0.922100	-0.001900	0.922500	0.004000
0.966200	-0.021000	0.966200	-0.021000	0.961100	-0.000300	0.961300	0.001900
1.000000	0.000000	1.000000	0.000000	1.000000	0.000000	1.000000	0.000000

<u>Section 5</u>		<u>Section 6</u>		<u>Section 7</u>		<u>Section 8</u>	
1.000000	0.000000	1.000000	0.000000	1.000000	0.000000	1.000000	0.000000
0.961600	0.007200	0.961700	0.007700	0.961700	0.008200	0.961600	0.007700
0.923100	0.013500	0.923200	0.014400	0.923200	0.015300	0.923100	0.014300
0.884500	0.019100	0.884500	0.020500	0.884600	0.021800	0.884400	0.020300
0.845800	0.024000	0.845900	0.026000	0.845900	0.028000	0.845700	0.025900
0.807000	0.028300	0.807100	0.031000	0.807200	0.033600	0.806900	0.031000
0.768200	0.032200	0.768300	0.035400	0.768400	0.038700	0.768000	0.035600
0.729300	0.035600	0.729400	0.039400	0.729500	0.043200	0.729100	0.039800
0.690400	0.038800	0.690400	0.043000	0.690500	0.047200	0.690200	0.043600
0.651500	0.041700	0.651500	0.046300	0.651500	0.050900	0.651200	0.046900
0.612500	0.044200	0.612500	0.049100	0.612500	0.053900	0.612100	0.049800
0.573500	0.046400	0.573500	0.051400	0.573400	0.056500	0.573100	0.052100
0.534500	0.048100	0.534400	0.053300	0.534300	0.058400	0.534000	0.054000
0.495500	0.049500	0.495300	0.054600	0.495200	0.059700	0.494900	0.055500
0.456500	0.050400	0.456300	0.055400	0.456000	0.060400	0.455700	0.056500
0.417500	0.050900	0.417200	0.055700	0.416900	0.060400	0.416600	0.057100
0.378400	0.051000	0.378100	0.055400	0.377700	0.059800	0.377500	0.057200
0.339400	0.050600	0.339000	0.054500	0.338600	0.058500	0.338400	0.056900
0.300400	0.049700	0.299900	0.053200	0.299500	0.056800	0.299300	0.056000
0.261400	0.048300	0.260900	0.051400	0.260400	0.054600	0.260200	0.054700
0.222400	0.046400	0.221900	0.049100	0.221300	0.051800	0.221100	0.052700
0.183400	0.043800	0.182900	0.046200	0.182300	0.048600	0.182000	0.050000
0.144600	0.040500	0.143900	0.042600	0.143300	0.044600	0.143100	0.046400
0.105800	0.036200	0.105100	0.038000	0.104500	0.039800	0.104300	0.041400
0.067200	0.030500	0.066500	0.031900	0.065900	0.033400	0.065700	0.034500
0.029100	0.022000	0.028500	0.022900	0.027900	0.023800	0.028000	0.024300
0.011600	0.015400	0.011200	0.015900	0.010700	0.016300	0.011100	0.016200
0.003600	0.009300	0.003500	0.009400	0.003300	0.009500	0.003800	0.009300
0.000000	0.000000	0.000000	0.000000	0.000000	0.000000	0.000000	0.000000
0.004400	-0.008700	0.003900	-0.009000	0.003400	-0.009400	0.003700	-0.009200
0.013200	-0.013500	0.012200	-0.014500	0.011200	-0.015600	0.011700	-0.015300
0.031100	-0.018500	0.030000	-0.020000	0.028900	-0.021600	0.029300	-0.021400
0.069300	-0.025300	0.068300	-0.027000	0.067200	-0.028800	0.067500	-0.028800
0.108000	-0.029000	0.107000	-0.030600	0.106000	-0.032200	0.106300	-0.032600
0.146800	-0.030200	0.145900	-0.031600	0.145000	-0.033000	0.145200	-0.033900
0.185700	-0.029600	0.184800	-0.030700	0.183900	-0.031800	0.184100	-0.033200
0.224500	-0.028100	0.223700	-0.028800	0.222900	-0.029500	0.223000	-0.031300
0.263300	-0.026300	0.262500	-0.026400	0.261700	-0.026500	0.261900	-0.028800
0.302100	-0.024500	0.301300	-0.023900	0.300600	-0.023200	0.300700	-0.026000
0.340900	-0.022600	0.340100	-0.021200	0.339400	-0.019900	0.339500	-0.023100
0.379700	-0.020600	0.379000	-0.018600	0.378200	-0.016600	0.378400	-0.020200
0.418500	-0.018400	0.417800	-0.015900	0.417100	-0.013400	0.417200	-0.017300
0.457200	-0.016100	0.456600	-0.013100	0.455900	-0.010200	0.456000	-0.014500
0.496000	-0.013700	0.495400	-0.010300	0.494800	-0.007000	0.494900	-0.011700
0.534800	-0.011100	0.534200	-0.007500	0.533600	-0.003900	0.533700	-0.008900
0.573500	-0.008500	0.573000	-0.004600	0.572500	-0.000800	0.572500	-0.006100
0.612300	-0.005700	0.611800	-0.001700	0.611300	0.002300	0.611400	-0.003300
0.651000	-0.002700	0.650600	0.001300	0.650200	0.005300	0.650200	-0.000400
0.689800	0.000500	0.689400	0.004400	0.689000	0.008400	0.689100	0.002600
0.728500	0.003700	0.728200	0.007500	0.727900	0.011300	0.727900	0.005500
0.767200	0.006400	0.767000	0.009900	0.766800	0.013400	0.766800	0.007800
0.806100	0.008000	0.805900	0.011100	0.805800	0.014300	0.805700	0.009100
0.844900	0.008300	0.844800	0.011000	0.844800	0.013700	0.844600	0.009100
0.883700	0.007400	0.883700	0.009600	0.883700	0.011800	0.883500	0.008200
0.922500	0.005600	0.922500	0.007200	0.922600	0.008900	0.922400	0.006300
0.961300	0.002800	0.961300	0.003800	0.961300	0.004700	0.961200	0.003400
1.000000	0.000000	1.000000	0.000000	1.000000	0.000000	1.000000	0.000000

<u>Section 9</u>		<u>Section 10</u>		<u>Section 11</u>	
1.000000	0.000000	1.000000	0.000000	1.000000	0.000000
0.961600	0.007300	0.961600	0.003700	0.961300	0.007300
0.922900	0.013400	0.922900	0.006700	0.923200	0.017100
0.884200	0.018800	0.884200	0.009400	0.885200	0.027200
0.845400	0.023800	0.845400	0.011900	0.846900	0.036700
0.806600	0.028400	0.806600	0.014200	0.808500	0.044900
0.767700	0.032600	0.767700	0.016300	0.770000	0.053300
0.728700	0.036400	0.728700	0.018200	0.731200	0.059900
0.689800	0.039900	0.689800	0.019900	0.692200	0.065600
0.650800	0.043000	0.650800	0.021500	0.653100	0.070000
0.611800	0.045600	0.611800	0.022800	0.613900	0.073600
0.572700	0.047800	0.572700	0.023900	0.574600	0.076300
0.533600	0.049700	0.533600	0.024800	0.535300	0.078000
0.494600	0.051200	0.494600	0.025600	0.495900	0.078400
0.455500	0.052600	0.455500	0.026300	0.456600	0.078500
0.416400	0.053800	0.416400	0.026900	0.417200	0.078000
0.377300	0.054700	0.377300	0.027400	0.377900	0.076700
0.338200	0.055300	0.338200	0.027600	0.338600	0.074600
0.299000	0.055300	0.299000	0.027700	0.299300	0.072100
0.259900	0.054800	0.259900	0.027400	0.260100	0.068400
0.220800	0.053500	0.220800	0.026800	0.221000	0.064000
0.181800	0.051400	0.181800	0.025700	0.182000	0.058600
0.142800	0.048100	0.142800	0.024000	0.143100	0.052300
0.104000	0.043000	0.104000	0.021500	0.104400	0.045100
0.065600	0.035700	0.065600	0.017900	0.066100	0.036200
0.028100	0.024800	0.028100	0.012400	0.028600	0.024100
0.011500	0.016100	0.011500	0.008100	0.011700	0.015700
0.004200	0.009100	0.004200	0.004500	0.003800	0.009200
0.000000	0.000000	0.000000	0.000000	0.000000	0.000000
0.004000	-0.009100	0.004000	-0.004500	0.003500	-0.009300
0.012100	-0.015000	0.012100	-0.007500	0.011500	-0.015500
0.029700	-0.021200	0.029700	-0.010600	0.028900	-0.022600
0.067800	-0.028800	0.067800	-0.014400	0.066900	-0.031600
0.106500	-0.033000	0.106500	-0.016500	0.105500	-0.037900
0.145300	-0.034700	0.145300	-0.017400	0.144400	-0.042800
0.184300	-0.034500	0.184300	-0.017300	0.183300	-0.046800
0.223100	-0.033200	0.223100	-0.016600	0.222300	-0.050100
0.262000	-0.031200	0.262000	-0.015600	0.261300	-0.052900
0.300800	-0.028800	0.300800	-0.014400	0.300400	-0.055100
0.339700	-0.026300	0.339700	-0.013100	0.339500	-0.056800
0.378500	-0.023800	0.378500	-0.011900	0.378600	-0.058100
0.417300	-0.021300	0.417300	-0.010600	0.417800	-0.059000
0.456100	-0.018800	0.456100	-0.009400	0.456900	-0.059500
0.495000	-0.016400	0.495000	-0.008200	0.496000	-0.059500
0.533800	-0.013900	0.533800	-0.007000	0.535200	-0.059000
0.572600	-0.011400	0.572600	-0.005700	0.574300	-0.058100
0.611400	-0.008800	0.611400	-0.004400	0.613400	-0.056500
0.650300	-0.006100	0.650300	-0.003000	0.652400	-0.054200
0.689100	-0.003200	0.689100	-0.001600	0.691500	-0.051100
0.727900	-0.000400	0.727900	-0.000200	0.730300	-0.046600
0.766700	0.002100	0.766700	0.001100	0.769000	-0.040400
0.805600	0.003800	0.805600	0.001900	0.807400	-0.033100
0.844500	0.004600	0.844500	0.002300	0.845800	-0.025300
0.883400	0.004600	0.883400	0.002300	0.884100	-0.017200
0.922300	0.003800	0.922300	0.001900	0.922400	-0.009300
0.961200	0.002100	0.961200	0.001100	0.961000	-0.002700
1.000000	0.000000	1.000000	0.000000	1.000000	0.000000